



저작자표시-비영리-변경금지 2.0 대한민국

이용자는 아래의 조건을 따르는 경우에 한하여 자유롭게

- 이 저작물을 복제, 배포, 전송, 전시, 공연 및 방송할 수 있습니다.

다음과 같은 조건을 따라야 합니다:



저작자표시. 귀하는 원저작자를 표시하여야 합니다.



비영리. 귀하는 이 저작물을 영리 목적으로 이용할 수 없습니다.



변경금지. 귀하는 이 저작물을 개작, 변형 또는 가공할 수 없습니다.

- 귀하는, 이 저작물의 재이용이나 배포의 경우, 이 저작물에 적용된 이용허락조건을 명확하게 나타내어야 합니다.
- 저작권자로부터 별도의 허가를 받으면 이러한 조건들은 적용되지 않습니다.

저작권법에 따른 이용자의 권리는 위의 내용에 의하여 영향을 받지 않습니다.

이것은 [이용허락규약\(Legal Code\)](#)을 이해하기 쉽게 요약한 것입니다.

[Disclaimer](#)

공학박사 학위논문

**Non-inductive current drive
utilizing 3D magnetic flux ropes in
Versatile Experiment Spherical Torus**

**VEST 장치에서의 3D 자기 플럭스 로프를 활용한
비유도적 전류 구동 연구**

2022년 8월

서울대학교 대학원
에너지시스템공학부
박 중 윤

Non-inductive current drive utilizing 3D magnetic flux ropes in Versatile Experiment Spherical Torus

**VEST 장치에서의 3D 자기 플럭스 로프를 활용한
비유도적 전류 구동 연구**

지도 교수 황 용 석

이 논문을 공학박사 학위논문으로 제출함
2022 년 8 월

서울대학교 대학원
에너지시스템공학부
박 종 윤

박종윤의 공학박사 학위논문을 인준함
2022 년 8 월

위 원 장	정 경 재	(인)
부위원장	황 용 석	(인)
위 원	나 용 수	(인)
위 원	윤 건 수	(인)
위 원	유 종 수	(인)

Abstract

Non-inductive current drive utilizing 3D magnetic flux ropes in Versatile Experiment Spherical Torus

Jong Yoon Park

Department of Energy System Engineering

(Fusion & Plasma Engineering)

The Graduate School

Seoul National University

In tokamak configuration, increasing magnetic helicity, the linkage of toroidal and poloidal flux, means increasing toroidal plasma current, thereby increasing the performance of tokamak plasma. To inject magnetic helicity, DC (electrostatic) Local Helicity Injection (LHI) technique using 3D magnetic flux ropes has been developed. The LHI can be used as a means of current drive for tokamak and a non-inductive startup for the spherical torus (ST) that deals with the limited-central-inductive-flux swing.

To use the LHI technique as a startup, the seed plasma in closed-flux-surface (CFS) should be formed by 3D magnetic flux ropes. With this seed plasma, the plasma current can be driven further via LHI and the Taylor relaxation process that convert the localized injected helicity into global helicity and macroscopic plasma current. Finally, a closed flux surface that resembles a tokamak plasma (tokamak-like state) can be formed. The operation using the LHI technique as a startup will fail without forming the seed plasma.

One candidate of the MHD instabilities that can form a seed plasma in CFS is the merging between flux ropes undergoing current-driven kink instability in 3D helical

geometry. However, the operational conditions required for forming seed plasma from the 3D magnetic flux ropes in ST remained unsolved, resulting in the possibility of operational failure. Therefore, understanding the profound physics of changing magnetic topology to a tokamak-like state from magnetic flux ropes in 3D helical geometry is the key to the successful operation of LHI as a startup method. So, the object of this thesis is to find the answer to the number of open questions regarding how to/ what physics related to reaching a Taylor relaxation process from the discharging 3D helical magnetic flux ropes.

To form 3D helical flux ropes in VEST, the LHI system consisting of two arc plasma guns and two pulsed powers is developed and successfully commissioned. According to discharge conditions, the arc plasma guns can discharge flux ropes with a total current of 3 kA within a power of up to 1.5 MW. The typical normalized effective toroidal loop voltage value can range from 1.4 to 2.4 V-m. In this thesis, ion Doppler spectroscopy is used to measure ion temperature, which is used to evaluate merging activity. The main spectral line is CIII (464.7nm), the strongest impurity line in VEST.

Before rope-rope merging takes place, the various MHD states in the 3D magnetic flux ropes discharged by arc plasma guns have been observed and analyzed. Magnetic diagnostics and spectroscopy confirm all these states without any invasive measurement. The axial magnetic field strength is the key to controlling the stability state of flux ropes. When the axial field strength is stronger than poloidal field strength driven by flux ropes, the flux ropes are in a stable state that the neutral pressure highly influences the temperature and density of the plasma. When the axial field strength is decreased, the coherent internal kink mode has appeared. The kink characteristics such as rotating frequency and deformation are calculated, which shows good agreement with experimental results. The coherent rotating model based on both phenomenological kink theory and the monoenergetic assumption is also developed, and its calculation results

also agreed well with experimental measurement. By reducing the axial magnetic field further, the highly unstable external kink mode is appeared, leaving chaotic signals on the magnetic pick-up coil. With this external kink mode, the flux ropes can be merged via magnetic reconnection, resulting in a linear relationship between the discharge power and ion temperature. The axial magnetic field can act as both stabilizing force that the kink stability in flux ropes and repulsing force that suppresses the merging activity. When the distance between the ropes is reduced, the ion temperature is also increased, which is consistent with the calculation results that show an increased reconnection field angle in the 3D reconnection configuration. In this study, it is confirmed that there is a specific upper limit of the magnetic field strength to initiate merging between flux ropes for a given power range. The flux ropes can be merged by kink instability in flux rope within the limit.

As the merging process is undergoing, one more condition should be met to drive toroidal plasma current non-inductively and continuously; proximity. Then the Taylor relaxation phase can be reached with sustained plasma by radial force balance. Only when the vertical magnetic field is adjusted to give high proximity between flux ropes and the seed plasma the multiplication factor has reached ~ 10 (more than the geometrical factor of 4), and the toroidal plasma current is driven up to 15 kA with an injection current of 1.5 kA. The increased CIII/II ratio is observed during the current ramp-up phase, meaning improved confinement. The magnetic reconstruction results using FEM show the formation of CFS in the toroidally averaged sense. As the coupling (proximity) between the toroidal plasma and flux ropes is maintained, the toroidal plasma current is driven non-inductively. At the same time, the edge localized peaked profile of ion temperature is measured at the low-field side, indicating where the strong reconnection activity takes place.

Interestingly, the magnetic signals from kink mode in flux rope also disappeared,

similar to “reduced-MHD mode” which is the newly discovered mode at the other device. At the end of discharge, as radial force is not balanced, the coupling is halted (decreased proximity), decaying the toroidal plasma, indicating the end of the Taylor relaxation phase. The external kink signal from the flux ropes appeared again.

The magnetic flux rope in 3D helical geometry plays an essential role from the merging to the LHI phase. Based on studying the stability mode of 3D flux ropes, the experimental operational regime for a given injection power is suggested. The more increased toroidal plasma driven by the LHI is expected with increased injection power and vacuum field controllability.

Keywords: Spherical Torus, Plasma gun, Pulsed Power, Magnetic Reconnection, Merging, Helicity Injection.

Student Number: 2013-23180

Table of Contents

Abstract.....	i
Table of Contents.....	v
List of Tables.....	vii
List of Figures.....	viii
Chapter 1. Introduction and Motivation	1
1.1. Nuclear Fusion and Tokamaks.....	1
1.2. The need for non-inductive current-drive	3
1.3. Startup and Current drive via DC helicity injection	5
1.4. Merging activity during LHI.....	8
1.5. Goals of Thesis	12
Chapter 2. Theory and Prior Work.....	14
2.1. Arc plasma gun and its physics.....	14
2.2. Kink instability of flux ropes discharged by arc plasma gun.....	17
2.3. Magnetic reconnection and merging of flux ropes	22
2.4. Magnetic Helicity Conservation and Taylor Relaxation.....	29
Chapter 3. Experimental Setup	34
3.1. The VEST Machine	34
3.2. Diagnostics.....	37
3.2.1. Magnetic diagnostics.....	37
3.2.2. Spectroscopies	39
3.2.2.1. Ion Doppler Spectroscopy.....	39
3.2.2.2. Filterscope.....	41
3.2.2.3. Fast Camera	43
3.3. Helicity injection system	45
3.3.1. Arc plasma guns.....	45

3.3.2. Pulsed power systems	50
3.3.3. Plasma gun operation.....	60
Chapter 4. 3D helical flux rope merging.....	64
4.1. Kink instability in flux rope.....	65
4.1.1. MHD-Stable discharge.....	65
4.1.2. Identification of two kink modes [50].....	72
4.1.3. Coupling to kink theory.....	79
4.2. Conditions for merging.....	88
4.2.1. Dependence of merging on the guide field	90
4.2.2. Dependence of merging on the field pitch	97
4.2.3. Impedance changes of flux rope during merging.....	102
4.3. Discussion.....	104
Chapter 5. Demonstration of local helicity injection	105
5.1. Conditions for transition to HI phase.....	105
5.1.1. The effect of proximity.....	105
5.1.2. Operating regime for LHI technique.....	120
5.2. Characteristics of plasma driven by LHI	126
5.2.1. Anomalous ion heating	126
5.2.2. Initial measurement of Te, ne profile	132
5.2.3. The MHD transition.....	135
Chapter 6. Conclusions and Future Work.....	140
6.1. Conclusions.....	140
6.2. Future work.....	140
Bibliography	142
국 문 초 록.....	146

List of Tables

Table 1. The calculated mean-free-path, collision frequency and momentum frequency.	72
---	-----------

List of Figures

Figure 1.1 Cross-section for fusion	2
Figure 1.2 Basic characteristic of tokamak geometry[12]	4
Figure 1.3 The difference between Spherical torus($R/a \sim 1.5$) and (a high-aspect-ratio)Tokamak [12]	4
Figure 1.4 (a) 3D Field following calculation results during LHI in VEST as a current drive, (b) Magnetic reconstruction result using Finite element method for Shot 35964 at 304 ms. The colored contour in (b) show the current density distribution. (c) Fast camera image	6
Figure 1.5 Typical process of LHI as a startup.....	7
Figure 1.6 The non-linear, 3D resistive MHD NIMROD results that describe the LHI process. Taken from figure 6.21 of [13].....	9
Figure 1.7 Taken from figure 6.7 of [13].	10
Figure 1.8 I_p evolution of an LHI-Ohmic coupling shot. Taken from figure 4 of [15]	11
Figure 1.9 Objective of thesis	13
Figure 2.1 Arc plasma gun impedance model. Taken from figure 4.8 of [19]	16
Figure 2.2 The impedance tendency of arc plasma gun in VEST	16
Figure 2.3 Taken from figure 4 of [22]	18
Figure 2.4 Taken from figure 5 of [21]	18
Figure 2.5 Taken from figure 5 of [23]	18
Figure 2.6 Coherent motion. Taken from figure 12 of [25]	21
Figure 2.7 Chaotic, incoherence motion. Taken from figure 5.6 of [27]	21
Figure 2.8 The effect of background plasma. Taken from figure 4.11 of [26]	21
Figure 2.9 Magnetic reconnection layer in 2D.....	24
Figure 2.10 Collisionless reconnection layer, Taken from figure 4 of [33]	24
Figure 2.11 Taken from figure 2 of [34].....	25
Figure 2.12 Taken from figure 5 of [35]	27
Figure 2.13 Taken from figure 3 of [36]	28
Figure 2.14 Magnetic helicity in toroidal system.....	31
Figure 2.15 The experimental picture of helicity flow using 3D helical flux rope	32
Figure 2.16 Taken from figure 1 of [39]	33

Figure 2.17 Taken from figure 5 of [40]	33
Figure 3.1 (a) VEST cross section showing field configuration and size. (b) VEST cross-section Top view (Cutaway at $Z = 0$)	36
Figure 3.2 toroidal cross-section of VEST. The magenta hexagram indicates the location of the arc plasma gun. The black circles indicate the locations of flux rope used in this study at the toroidal location of the magnetic pickup coil array.	38
Figure 3.3 Schematic view of IDS system in VEST [29]	40
Figure 3.4 Filterscope system in VEST.....	42
Figure 3.5 Fast camera image of discharges in this study.	44
Figure 3.6 A schematic diagram of early version of pulsed electron gun.	47
Figure 3.7 (a) Cutaway schematic of the VEST device with local helicity injection system, and (b) toroidal cross-section of VEST. The magenta hexagram indicates the location of the arc plasma gun. The black circles indicate the locations of flux rope used in this study at the toroidal location of the magnetic pickup coil array.	48
Figure 3.8 Schematics of newly designed arc plasma gun. (a) Miniaturized arc chamber, (b) Feedthrough, (c) Outer housing and fully assembled arc plasma gun.	49
Figure 3.9 (a) An experimental circuit diagram of the helicity injection system, and (b) an equivalent circuit during discharge.	53
Figure 3.10 (a) Comparison of simulated and measured injection current (top) and voltage (bottom) and (b) load impedance, arc impedance and injection impedance as a function of the injection length.	54
Figure 3.11 Circuit diagram of pulsed power system for magnetic flux ropes. When the arc plasma guns are negatively biased with respect to the VEST upper plate, the flux ropes are discharged. Shown are the pulse forming network (PFN), Insulated gate bipolar transistors (IGBTs).	56
Figure 3.12 (a) Discharge results of PFNs with sparker circuit for arc discharge. (b) Simulation results of PFN with matching condition.....	57
Figure 3.13 A schematic of Helicity injection power system for VEST	58
Figure 3.14 Photos of Helicity injection power system	59
Figure 3.15 Typical discharge results. (a) Flux rope current for each arc plasma gun. Because there are two guns, the total flux rope current is twice that of the waveform. (b) Voltage for maintaining flux ropes. For LHI, the flux rope current and voltage are known as	

injection current, injection voltage respectively.....	62
Figure 3.16 The radial profile of background plasma parameters is measured using a triple Langmuir probe at $Z = 0$ m of VEST. (a) Electron density, n_e , (b) Electron temperature, T_{eff} . Background plasma is extracted based on the pressure difference between the interior and exterior of the arc plasma gun. Flux rope discharge power is zero for these measurements.	63
Figure 4.1. Three selected discharge result for high field strength scan. (a) line-integrated OV/OII ratio measured by filter scope. (b) total flux rope current. (c) discharge voltage. (d) neutral pressure time evolution.	66
Figure 4.2 The IDS measurement results. (a) the ratio between vacuum field strength of 88 mT to poloidal field strength by flux rope. Note that high ratio value means more stable flux rope state. (b) Acceleration calculated from shift of CIII spectrum(c) Ion temperature of CIII impurity.....	67
Figure 4.3 Example spectra corresponding three selected data in figure 4.2.....	68
Figure 4.4 The spectrogram from inboard magnetic pickup coil and the Rogowski coil in VEST. The coherent signal of shot 35655 means flux ropes undergoes internal kink mode.	70
Figure 4.5 Fast camera image of discharges of figure 4.1. The exposure time of each frame is set 0.4ms. The yellow-dot-enclose-line indicate inner wall of VEST, red dot line shows the outer mid limiter.	71
Figure 4.6 Spectrograms for two controlled discharges. (a) Flux rope current evolution for coherent rotating kink mode. (b) Spectrogram for pickup coil, I02, in coherent rotating kink mode. (c) Spectrogram for Rogowski coil in coherent rotating kink mode. (d) Flux rope current evolution for kink mode transition discharge. (e) Spectrogram for pickup coil, I02, in kink mode transition discharge. (f) Spectrogram for Rogowski coil in kink mode transition discharge. Whereas the Rogowski coil is unable to measure signals from varying locations of the flux rope, the pickup coil is able to obtain such measurements.....	74
Figure 4.7 Propagation of coherent perturbation along with azimuthal (poloidal) and axial directions for two different discharges. (a)–(c) show azimuthal perturbations obtained from inside(I11) and outboard(O11) pickup coil set, and (d)–(f) show those in axial direction.....	76

Figure 4.8 Spectrograms for two controlled discharges and calculated frequency of kink mode. (a) Low-current mode subject to coherent rotating kink mode, (b) High-current mode transitioned to external kink mode from coherent rotating kink mode. The two spectrograms in this figure are the same as those depicted in figs. 8(b) and (e). Because these discharges are controlled by gas injection, different Alfvén Mach numbers, M , are used for the calculation. Kink frequency during transition is precisely calculated for the given M number range. Flux rope current evolutions for each discharge are given in figs. 7 (a) and (b) respectively. ($a = 30$ mm, $L = 5$ m, $B_{axial} = 350$ G).....	83
Figure 4.9 Toroidal cross-sectional view for rotating kink mode. The red dot indicates the center of rotating flux rope, as calculated based on vacuum-field-following-calculation code. Values of <i>fkink</i> and <i>rkink</i> are calculated from Eqs. (4.1) and (4.2), respectively. Through the use of simple electromagnetism, a magnetic signature from rotating flux rope can be calculated, as derived using Eqs. (4.3) and (4.4). 86	86
Figure 4.10 Magnetic signatures for coherent rotating kink mode. Black lines indicate experimental results obtained using inboard magnetic pickup coil array, whereas red lines indicate calculations obtained by using the rotating model, as shown in Fig. 4.9 and based on eq. (4.4).	87
Figure 4.11 Rope-rope merging experiment configuration.	89
Figure 4.12 The injection power scan with reduced axial field strength	91
Figure 4.13 Example spectra corresponding three selected data in figure 4.13	92
Figure 4.14 Three selected discharge result for low field strength scan. (a) line-integrated OV/OII ratio measured by filter scope. (b) total flux rope current. (c) discharge voltage. (d) neutral pressure time evolution.	93
Figure 4.15 The spectrogram from inboard magnetic pickup coil(up) and the Rogowski coil(down) in VEST. The chaotic signal on magnetic pickup coil means flux ropes undergoes external kink mode.	94
Figure 4.16 Fast camera image of discharges of figure 4.13. The exposure time of each frame is set 0.4ms. The yellow-dot-enclose-line indicate inner wall of VEST, red dot line shows the outer mid limiter.	95
Figure 4.17 The effect of guide field on reconnection field strength.....	98
Figure 4.18 The merging dependency on the distance between flux ropes	100

Figure 4.19 The spectrograms of two end points for each flux rope current in figure 4.16.....	101
Figure 4.20 Impedance changes during rope-rope merging and localized B-field amplification. (a) Discharge profile during rope-rope merging, (b) Cross-section and selected Mirnov coils, (c and d) BZ signals at two vertical ends (black and blue in (b)) for two shots in (a) and (e and f) BZ signals at $Z=0[m]$ (green in (b)) for two shots in (a)	103
Figure 5.1 (a) Evolution of MF (b) Time evolution of toroidal plasma current and flux rope current. Black(shot# 33547), Blue(shot# 33545). The current density (kA/m²) distributions for shot# 33547 are fitted (c) at 304.5 ms with the mean magnetic fitting error of 4.4 % and (d) at 305.6 ms with the mean magnetic fitting error of 5.2 %.....	109
Figure 5.2 Fast-camera images for shot# 33547 shown in Fig. 5.4. Exposure time for each shot is 0.4 ms . (a) Pre-Taylor relaxation time, (b) during Taylor relaxation at peak toroidal current, (c) reduced Taylor relaxation by radial force imbalance for tokamak plasma, (d) Taylor relaxation is halted.	110
Figure 5.3 (a) The evolutions of the applied vertical magnetic field, and (b) the mid limiter signal for shot# 33547 (black) and shot# 33545 (blue) respectively.	111
Figure 5.4 The effect of coupling for LHI. With sensitive control of vacuum field, sustained coupling is obtained, resulting in increased pulsed length. The purple line show the failure of LHI, which show the clear difference with other shots.	112
Figure 5.5 The effect of proximity. The white box indicates the calculated distance between the two plasmas.	114
Figure 5.6 Fast camera image at low proximity.	115
Figure 5.7 Magnetic reconstruction results using FEM for shot 35964. The white closed line shows the toroidally averaged CFS. The black line at the middle of figure is ion temperature profile for a given time.....	116
Figure 5.8 The vacuum field following considering FEM-reconstruction results.	118
Figure 5.9 Calculation of the Taylor state for Shot# 35964	119
Figure 5.10 LHI operating map for B = 34 mT	123
Figure 5.11 LHI operating map for B = 17 mT	124
Figure 5.12 LHI discharge results for operation map experiment.	125
Figure 5.13 IDS measurement results of Shot 35963. To check its anomalousness, the counter	

discharge of shot 35967 is shown in red. The graphs in top row show the emissivity. The graphs in middle row show the toroidal velocity while the graphs in low row show the ion temperature profile.....	128
Figure 5.14 Magnetic reconstruction results using FEM for shot 35963. The white closed line shows the toroidally averaged CFS. The black line at the middle of figure is ion temperature profile for a given time.....	129
Figure 5.15 IDS measurement results of Shot 35964. To check its anomalousness, the counter discharge of shot 35967 is shown in red. The graphs in top row show the emissivity. The graphs in middle row show the toroidal velocity while the graphs in low row show the ion temperature profile.....	130
Figure 5.16 The example of trial result of two gaussian fitting for IDS	131
Figure 5.17 Radial and time evolution of <i>ne</i> and <i>Te</i> using Thomson scattering measurement system in VEST.....	133
Figure 5.18 Radial and Time evolution of Soft X-ray signal. The filter #1 that can transmit the signal higher than 10eV, Al 0.1 um, was used. The signal is line integrated. White line in each graph shows the corresponding plasma current evolution. Shot 35967 : Failed LHI shot.....	134
Figure 5.19 Spectrograms of (a) Inboard magnetic pickup coil, I11, (b) Outer magnetic pickup coil, O11, (c) Rogowski coil for shot# 33547. Spectrograms of (d) Inboard magnetic pickup coil, I11, (e) Outer magnetic pickup coil, O11, (f) Rogowski coil for shot# 33545. The white line in Figs. 15(c) and 15(f) represents the toroidal plasma current measured by the Rogowski current.	138
Figure 5.20 Spectrograms approach of sustained current drive with LHI; Shot 35963((a), (b), (c)), Shot 35964((d), (e), (f)), Shot35967((g), (h), (i)).....	139

Chapter 1. Introduction and Motivation

1.1. Nuclear Fusion and Tokamaks

The realization of a clean and unlimited energy source is one of the ultimate goals for humankind. It is essential not only to escape from the threat of limited resource depletion but also to protect nature. Nuclear energy released by the fusion reaction of the nucleus is the closest way to achieve this ultimate goal. There is a good example that nuclear fusion is already an essential part of our lives; the Sun. The source of the sun's energy is nuclear fusion which indirectly gives energy to Earth. Thus, nuclear fusion is already deeply involved in our lives.

The energy can be generated by fusing two small nuclei into a single and more heavier nuclei with higher binding energy (alpha particle). The most compromising and favorable fusion reaction is between deuterium and tritium (D-T reaction)[1]

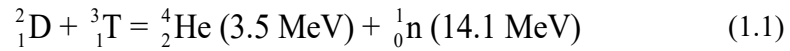


Figure 1.1 shows the cross-section for three different fusion reactions. To maximize D-T reaction, a temperature level around 10 keV is required. At this temperature, the reactants are in the plasma state as they completely are ionized. Here, one important thing is that these hot ionized reactants must be confined for fusion reaction, otherwise they will simply be cooled, and no more fusion reaction can take place. For the sun, the strong gravitational force is the main mechanism for confining the reactant in the plasma state and balancing the hot plasma pressure. Thus, to attain fusion reaction on Earth, thereby generating fusion energy for Earth, the novel and effective confinement method for plasma, hot ionized gas, is needed as the gravitational force like of the Sun is cannot be used on Earth. The concept called the tokamak magnetic confinement is employed as a creative means for the confinement of fusion grade plasmas on Earth. A comprehensive and intensive work of tokamak design, technology, and its physics can be found in [1].

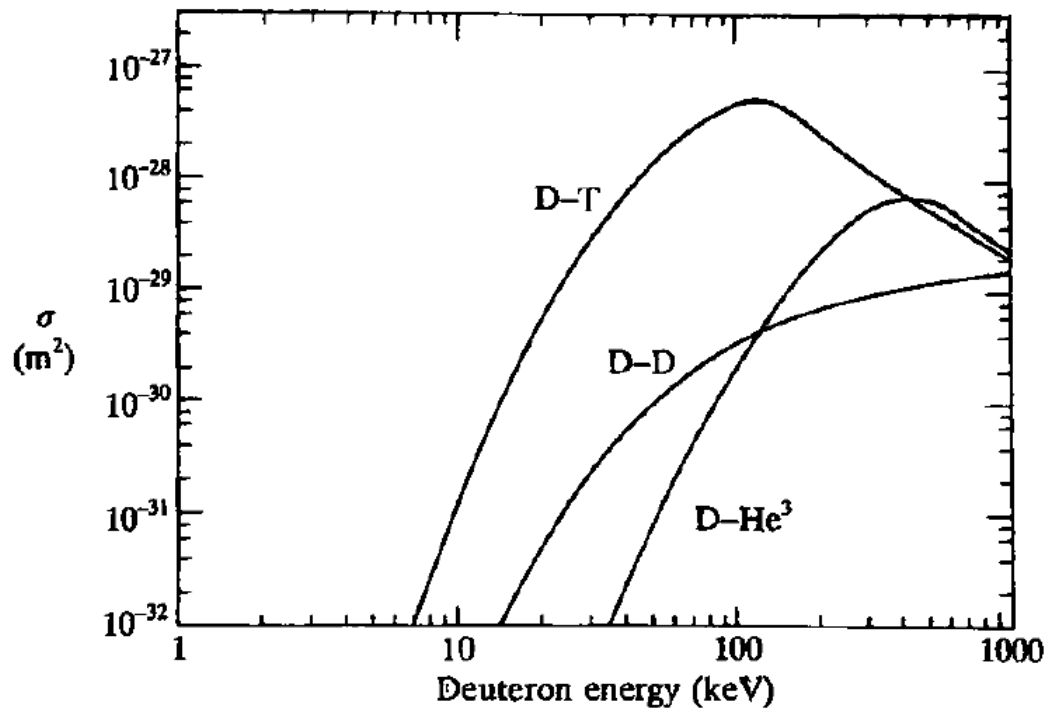


Figure 1.1 Cross-section for fusion

1.2. The need for non-inductive current-drive

The cost required to build the devices is one of the challenging parts for a tokamak. It is well known that the confinement properties for fusion reaction of tokamak can be improved by increasing the plasma radius, which means the increased total cost of building. So, if the performance of the fusion plasma can be maximized while the device size remains as small as possible, it would be a cost-effect way to get a fusion reaction. There is a convenient descriptor of plasma geometry called the aspect ratio $A = \frac{R_0}{a}$, where R_0 is the major radius and a is the minor radius as shown in figure 1.2. The low aspect ratio means that very elongated plasma volume, thereby maximizing the volume while minimizing the size of the device. Typically, the low aspect ratio of $A \leq 1.5$ is called as ‘Spherical Torus (ST)’. The geometry of ST compared to conventional tokamak is shown in figure 1.3.

While the ST has the cost-effeteness compared to the conventional tokamak, it also has a drawback; limited size of the central solenoid. Minimizing the size of the device would result in a reduction in the size of the solenoid coil, normally used for ohmic operation, which limits the capability of inductive flux swing and ohmic heating as compared to the conventional tokamak. It would be very helpful for ST if another current-drive method is developed for long-pulse, high I_p operation of ST.

So far, three major startup methods are widely developed and used for ST[2]; First of all, the merging startup is used. This can be divided into two parts; 1) merging compression[3], 2) Double null merging[4]. Second, RF is also used[5, 6]. Lastly, the DC helicity injection is used, and it can be divided into two parts; 1) Coaxial Helicity Injection (CHI)[2, 7, 8], and 2) Local Helicity Injection (LHI)[9-11]. LHI and CHI have both been demonstrated experimentally, but the focus of this thesis is on LHI startup. The details will be shown in Chapter 1.3.

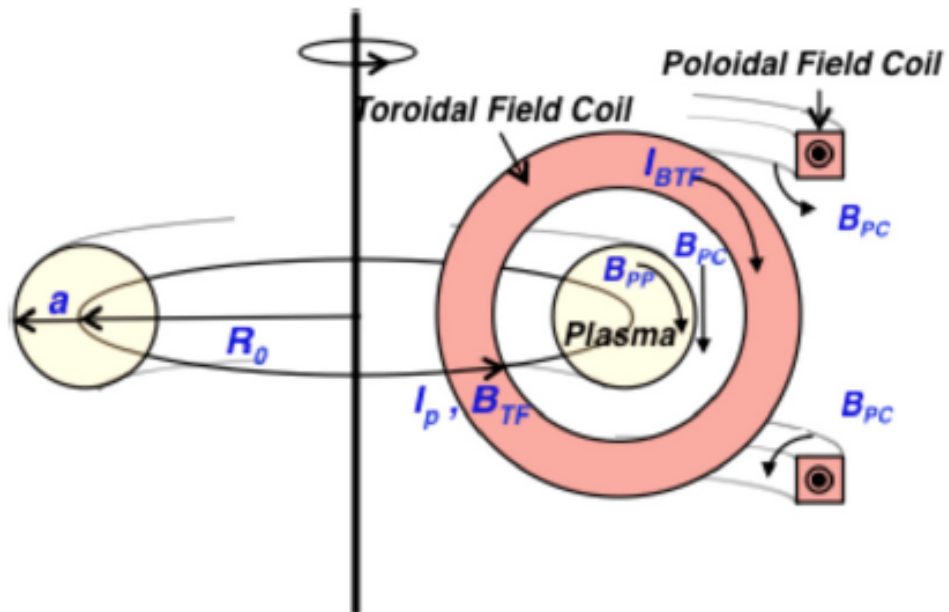


Figure 1.2 Basic characteristic of tokamak geometry[12]

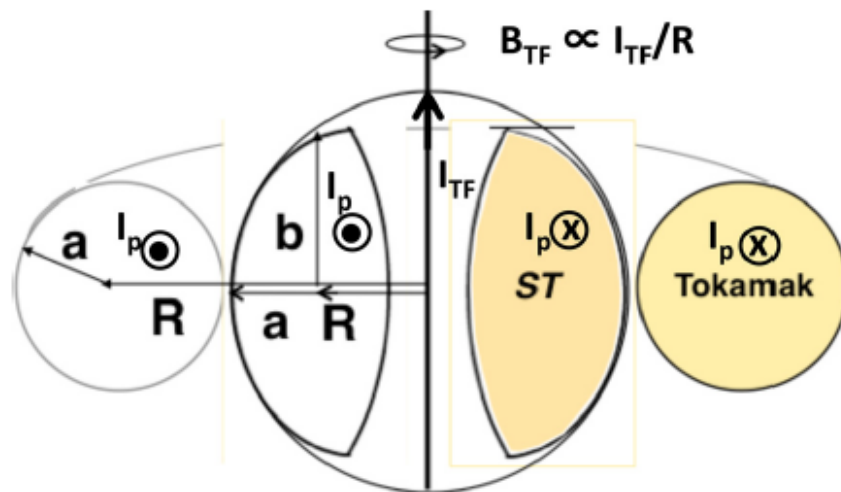


Figure 1.3 The difference between Spherical torus($R/a \sim 1.5$) and (a high-aspect-ratio)Tokamak [12]

1.3. Startup and Current drive via DC helicity injection

Magnetic helicity is a physical quantity that represents the linkage of magnetic flux in a volume. In a tokamak configuration, plasma current is directly proportional to helicity quantity as poloidal flux created by plasma current links the toroidal flux provided by the toroidal field coil. Thus, the helicity of the system will be increased if any method of current drive is applied to the plasma. Here, the DC helicity injection is a technique that adds helicity electrostatically. The detailed theoretical explanation will be described in section 2.4.

As shown in figure 1.4, recent DC helicity injection schemes have utilized magnetic flux ropes in the 3D helicity configuration of ST. The magnetic flux ropes with current follow the open field line that passes the plasma edge while close proximity is maintained. DC LHI technique also can be used not only as a non-inductive current drive but startup for ST as well. However, here, the unnatural process came up. To inject helicity, the plasma to be injected helicity should have coexisted with the plasma that can inject helicity. When LHI operation is used as a startup, there are only 3D magnetic flux ropes that can inject helicity to another plasma; there is no target plasma in Closed Flux Surface (CFS), as shown in figure 1.5 (a). This is a very important part for a successful startup via LHI operation considering that if there is no plasma in CFS, no matter how huge helicity is in 3D flux ropes, the helicity injection process cannot proceed. Thus, when 3D magnetic flux ropes are discharged for LHI operation, the seed plasma to be injected helicity should be formed from the 3D magnetic flux ropes. Afterward, DC helicity can be injected via Taylor relaxation, which is the self-organization of turbulently relaxing plasmas to minimum energy. So far, the conditions to form a seed plasma from the 3D magnetic flux ropes are not clear. The empirical trial tests are required to reach the Taylor relaxation state, resulting in the possibility of operational failure.

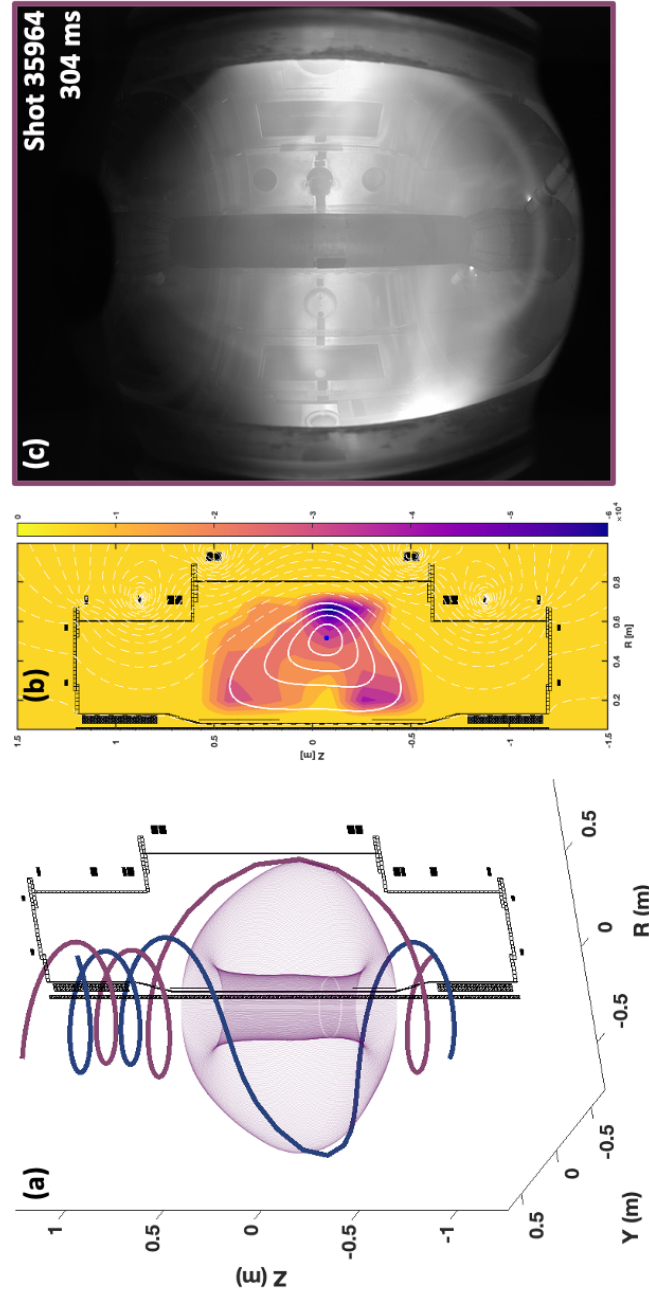


Figure 1.4 (a) 3D Field following calculation results during LHI in VEST as a current drive, (b) Magnetic reconstruction result using Finite element method for Shot 35964 at 304 ms. The colored contour in (b) show the current density distribution. (c) Fast camera image

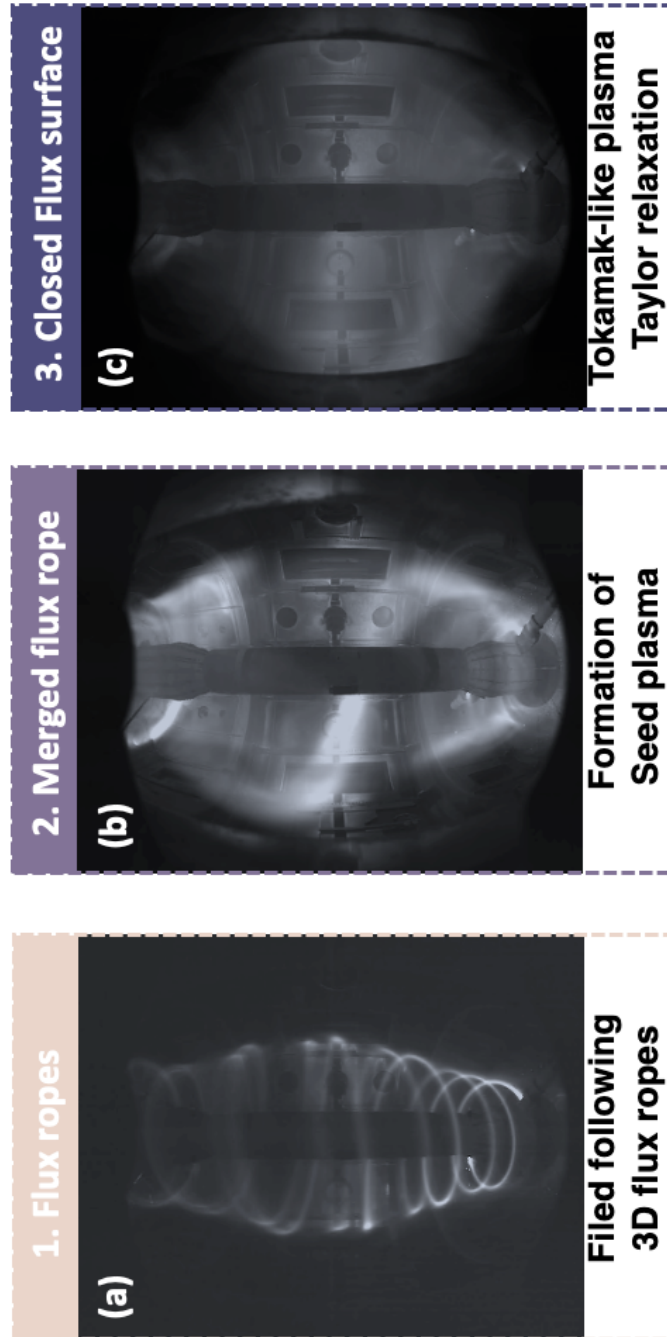


Figure 1.5 Typical process of LHI as a startup

1.4. Merging activity during LHI

Even though the experimental conditions to form a seed plasma are not clear, one possible mechanism that can form a seed plasma from 3D flux ropes is suggested by the non-linear, 3D resistive MHD NIMROD code[13, 14], and it shown at figure 1.6. The simulation results describe the possible mechanism as follows. In the 3D helical geometry, the kink-unstable flux rope undergoes large displacements in the poloidal plane. As shown in figure 1.7, with sufficient current in the flux rope, the interaction between adjacent flux ropes becomes stronger until they collide and merge via magnetic reconnection. After merging, the winding of the magnetic flux rope ring surrounding the central core is released. By accumulating these rings, until a global-scale poloidal magnetic field null is formed near the central core, a tokamak-like-state can be induced. Based on these results, presumably, the merging activity between flux ropes looks essential for LHI as a startup. However, because of its 3D configuration, it is not easy to confirm its MHD state, in other words, whether it is kink stable or not. In addition, without information on its MHD state, it is also not clear whether flux rope can merge or not.

When the LHI technique is used as a current drive, high CIII ion temperature tendency compared to Ohmic operation is measured[15], as shown in figure 1.8. Considering close proximity between the plasma to be injected helicity and magnetic flux ropes as shown in figure 1.7, during the current drive via LHI, it is also reasonable to expect magnetic reconnection activity between them.

Finally, during LHI operation as a startup, two merging activity via magnetic reconnection is expected, one for the formation of seed plasma and the other for DC helicity injection.

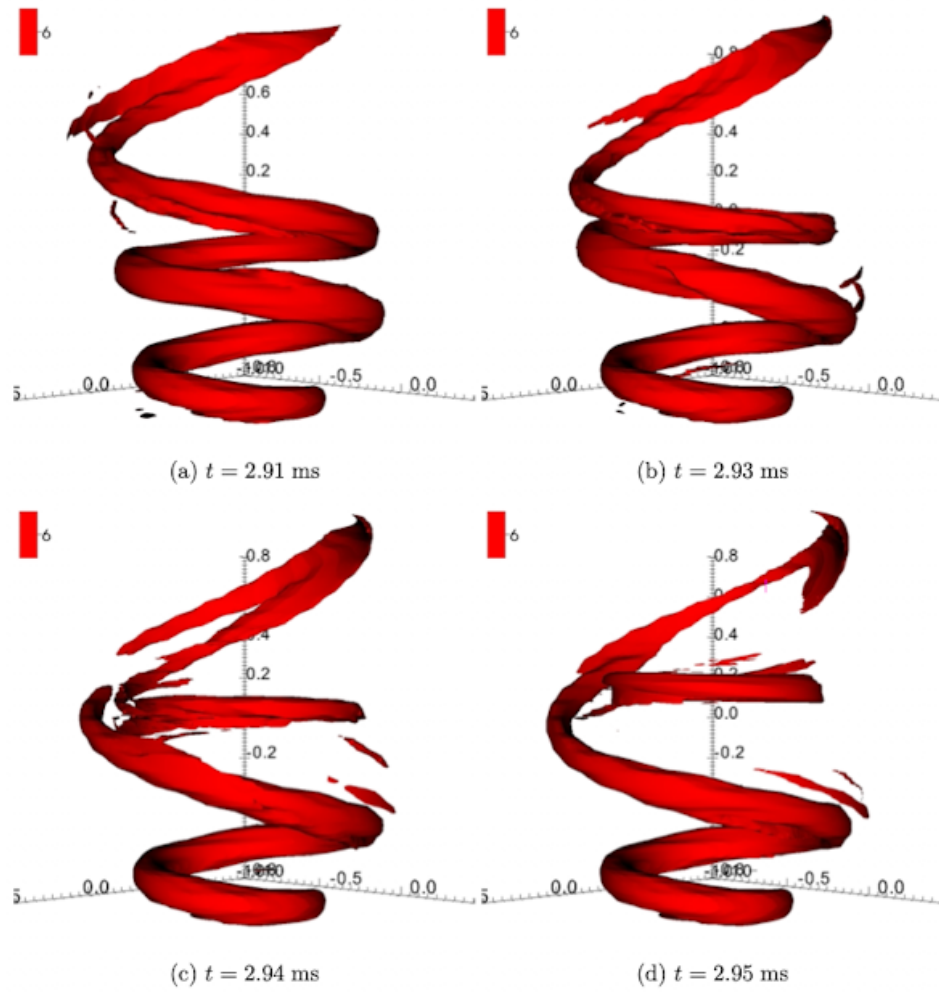


Figure 1.6 The non-linear, 3D resistive MHD NIMROD results that describe the LHI process. Taken from figure 6.21 of [13].

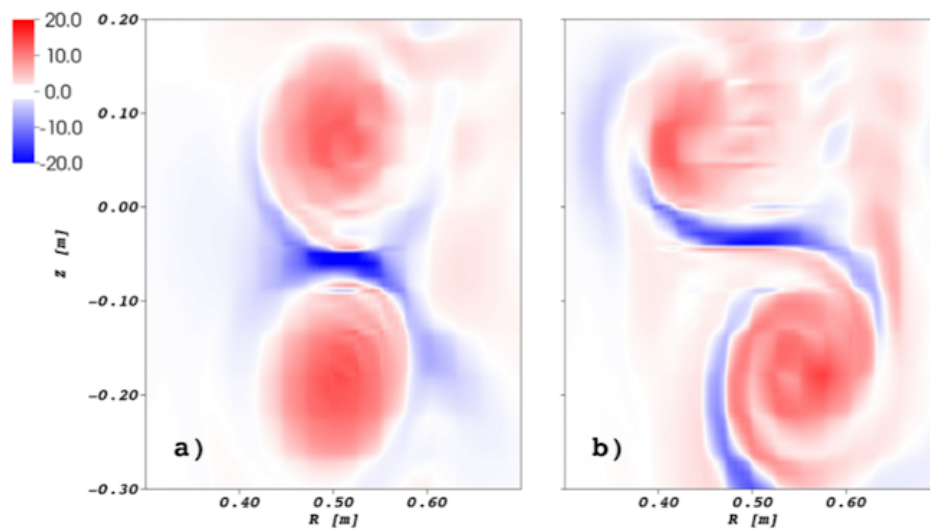


Figure 1.7 Taken from figure 6.7 of [13].

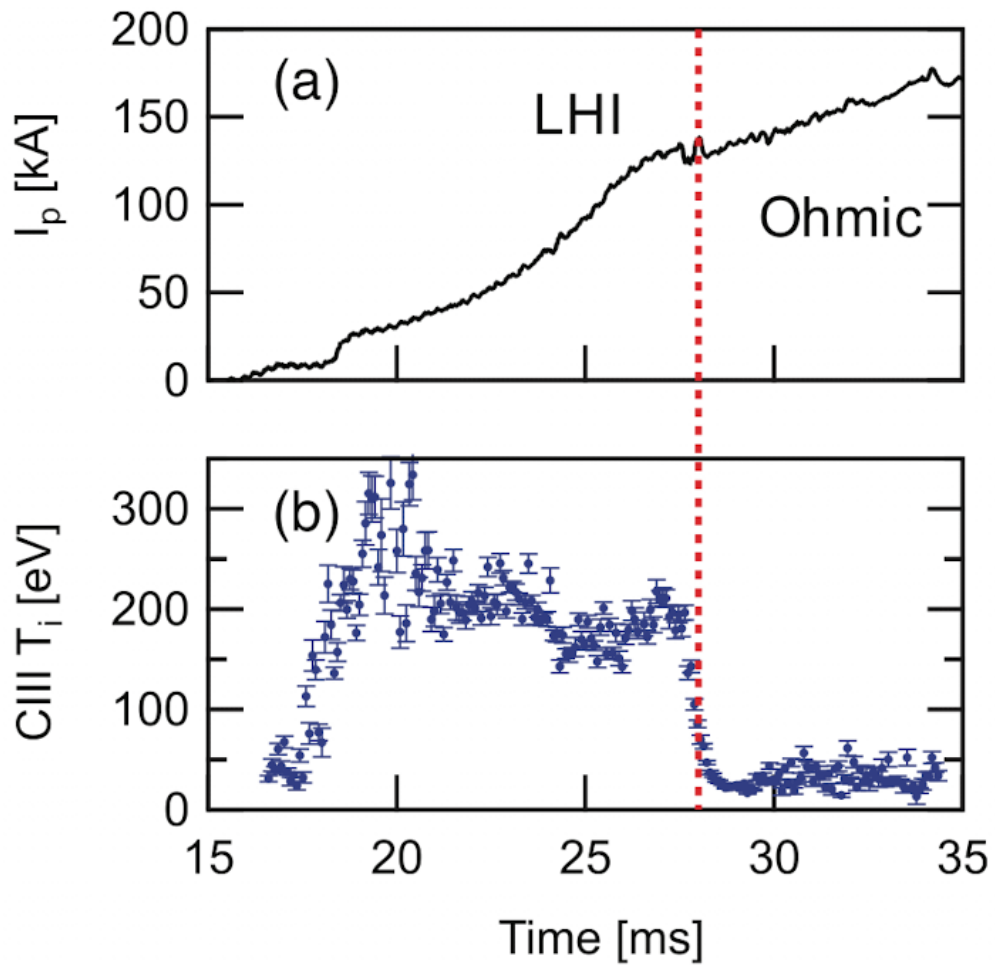


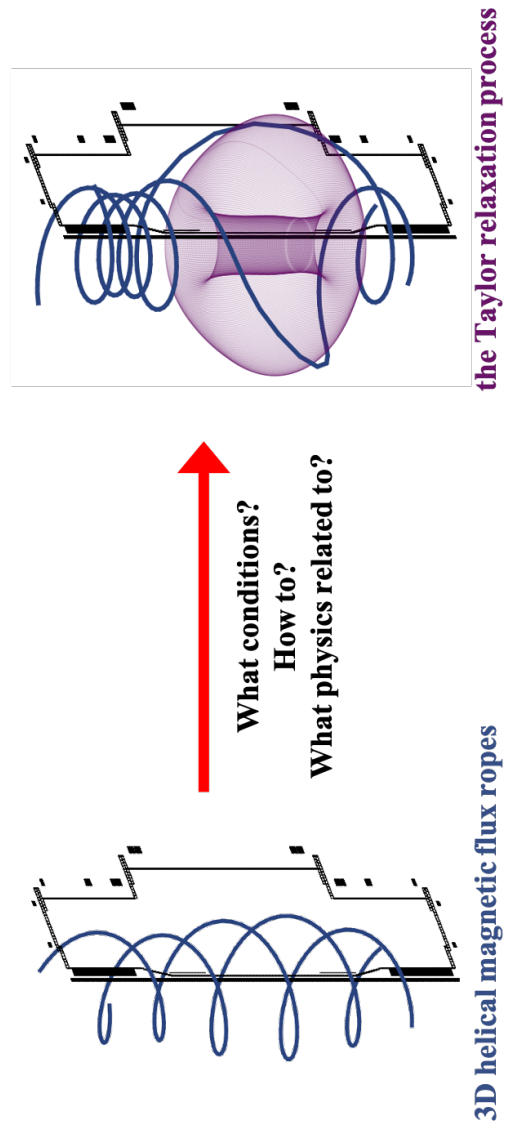
Figure 1.8 I_p evolution of an LHI-Ohmic coupling shot. Taken from figure 4 of [15]

1.5. Goals of Thesis

To achieve the Taylor relaxation phase, thereby driving plasma current via LHI, understanding the profound physics such as the MHD stability of flux ropes in 3D helical geometry, their merging, and its relevant ST operation is required. The object of this thesis is to find the answer regarding how to/what physics related to reaching a Taylor relaxation process from the discharging 3D helical magnetic flux ropes.

The following scientific and technical goals will be accomplished in this thesis.

1. Development of the LHI system and its commission in VEST
2. Determination of MHD stability of 3D magnetic flux ropes
3. Finding the conditions for rope-rope merging that can form seed plasma for LHI operation
4. Finding the conditions to reach Taylor relaxation phase
5. Characterization of tokamak-like plasma driven by LHI operation
6. Characterization of MHD during LHI operation



Main objective :

To provide **physically meaningful-experimental conditions** for LHI as a startup then startup!
Kink? Merging? and tokamak physics?

Figure 1.9 Objective of thesis

Chapter 2. Theory and Prior Work

2.1. Arc plasma gun and its physics

Discharging flux ropes with high plasma current is an important part of a successful LHI operation. The CDX and CDX-U at Princeton Plasma Physics Laboratory, the early device that demonstrated DC helicity injection technique, used a negatively biased hot emitting cathode, LaB6[9]. The injection(extracted) current, I_{inj} , up to 500A was achieved with cathode heater current of up to 400A. Note that the toroidal plasma current of 10 kA was driven using an injection current of 500 A. As the cathode is exposed in the chamber, the impurities from the cathode were indispensable, thereby giving limits to operation with injection power.

The breakthrough for high injection power was made by using an arc plasma gun that can discharge a current of kA[16, 17]. The arc plasma gun was suggested to control the current profile during the experiment on MST. The PEGASUS team has developed and utilized various versions of injectors that can handle high voltage/current in a large area. However, the high voltage operation has caused many problems on arc plasma gun such as cathode spot and flashover, and ultimately damaged parts of the plasma gun. In order to solve these problems, the plasma gun technology has been developed for years. Finally, a physics-based plasma gun design capable of high voltage operation has been proposed, and the high voltage operation for LHI has been successfully performed at the PEGASUS[10, 18]. Not only a physics-based plasma gun design but an impedance model for arc plasma were also developed and suggested by Hinson[[18, 19]]. In this beam impedance model, the charge carrier density, n_{beam} , is derived under conditions such as a monoenergetic beam and a uniform current profile. Consequently, the beam density is scaled to $n_{beam} \sim \frac{I_{flux\ rope}}{e v_d A_{inj}}$, where $I_{flux\ rope}$ is the flux rope current, $v_d =$

$\sqrt{\frac{2 e V_{flux\ rope}}{m_e}}$ is the drift velocity, e is the electron charge, m_e is the electron mass, and $V_{flux\ rope}$ is the voltage applied to the flux rope to maintain the discharge. The monoenergetic beam assumption used here is reasonable because the beam-plasma interaction can result in two velocity groups: bulk plasma of low energy and beam plasma of high energy[20]. Figure 2.1 show the V - I relation, so Z (impedance). The clear two regimes of operation are confirmed. The same analysis results for arc plasma gun in VEST are shown in figure 2.2.

The detailed operation description of arc plasma gun is in Section 3.3. By using a pulsed power system, the arc plasma gun can discharge flux rope that is the current-carrying plasma column in the magnetic field. Note that the magnetic field is applied externally.

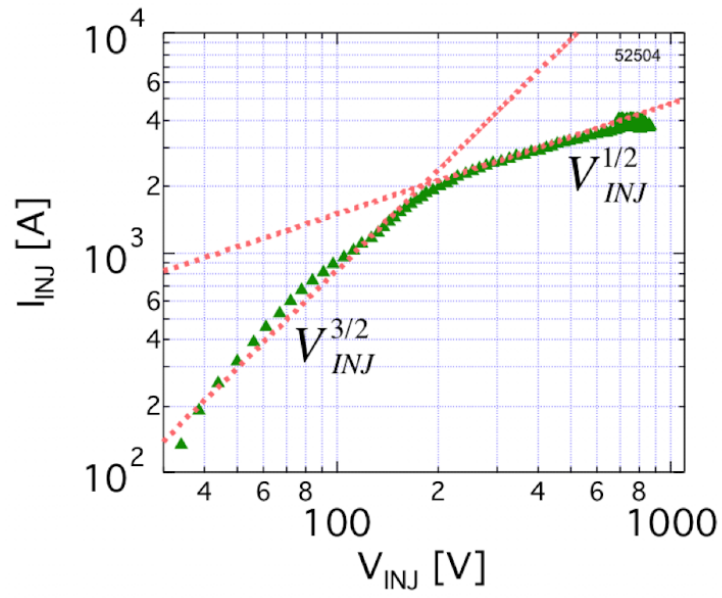


Figure 2.1 Arc plasma gun impedance model. Taken from figure 4.8 of [19]

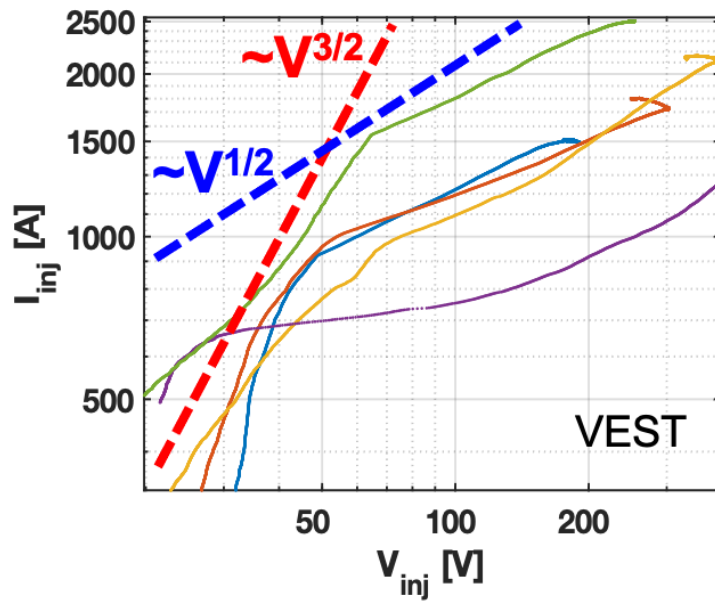


Figure 2.2 The impedance tendency of arc plasma gun in VEST

2.2. Kink instability of flux ropes discharged by arc plasma gun

As the current in flux rope can be increased from zero to kA by arc plasma gun, the appearance of magnetohydrodynamics instabilities is expected. One of the MHD instability that can be easily observed is current-driven kink instability. The appearance of kink instability and its structure are varied according to system geometry and the boundary condition[21, 22].

The ideal current threshold for kink instability in a line-tied condition at both ends is well known.

$$I_{KS} = \frac{(2\pi)^2 a^2 B_{axial}}{\mu_0 L} \quad (2.1)$$

This threshold current is called Kruskal-Shafranov limit. Above this threshold, the $J \times B$ forces can overcome the tension in the field lines, thereby kinking and rotating.

The current-driven rotating-kink instability and its mode have been theoretically investigated[22], showing that its rotating frequency and mode structure are determined by the boundary conditions and the geometrical (system) configuration. Ryutov et al.[22] proposed a phenomenological model for the rotating kink mode in a flux rope; the model is a unified method for describing effects such as boundary conditions, finite plasma resistivity, and plasma axial flow. Here, the axial flow is one of the distinct features that different from other models. Here, the axial flow indicates the flow of gas dynamics, not the current. When arc plasma gun is used to discharge flux rope, it has neutral gas flow from the gun inherently. So, applying the phenomenological model to flux rope discharged by arc plasma gun for analysis is more promising. Figure 2.3 show the kink mode structure suggested by phenomenological model. There are two different boundary condition; 1) both end (top), 2) one-end line-tied(bottom). It can also be seen that the structure is changed by the axial flow (broken lines in figure).

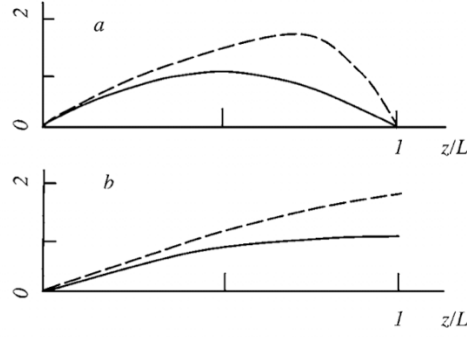


Figure 2.3 Taken from figure 4 of [22]

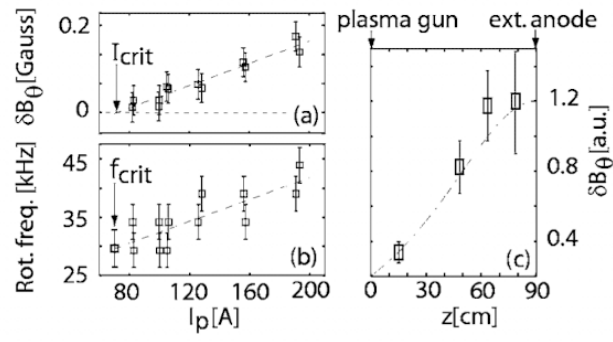


Figure 2.4 Taken from figure 5 of [21]

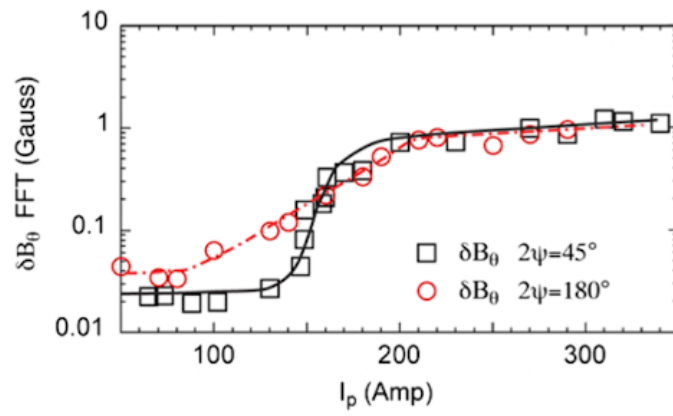


Figure 2.5 Taken from figure 5 of [23]

Experimentally, it is confirmed that the phenomenological model is agreed well with experimental measurement results. Figure 2.4 shows the detailed comparing results[21]. Note that this model is only effective up to lower than threshold limit, as beyond the threshold, the non-linear behavior of flux rope is appeared. Figure 2.5 describes that the boundary condition can be controlled by adjusting the angle of end plate[23]. In addition, there is clear transition from one-end free line-tied condition to both end line-tied condition.

Another important characteristic of kink plasma in flux rope discharged by arc plasma gun is rotating behavior. As the plasma current in the flux rope increases from zero, an azimuthal magnetic field component is generated in the flux rope, and an Alfvén wave is launched in the flux rope[13, 14]. The oscillations from the Alfvén mode intensify over time with increasing flux rope current; then, the $m=1$ global kink mode occurs in the flux ropes, which is consistent with a plasma column rotating as a rigid body with a certain frequency[22]. Because kink instability can be thought of as one part of the spectrum of surface Alfvén waves[24], the transition from the Alfvén wave to kink mode is not entirely unexpected. This rotating behavior in ropes has also been reported to be indicative of a helical equilibrium state or an internal kink[25], as shown in figure 2.6. In the laboratory frame, flux ropes in this kink mode show no movements (internal kink). The flux rope in the coherent rotating mode is accompanied by the axial current density perturbations with the same frequency of rotating[25]. As the current in flux rope are further increased, the chaotic, incoherence motion is appeared, as shown in figure 2.7.

Last important feature that affects kink instability in flux rope discharged by arc plasma gun is the existence of background plasma. As the arc plasma is kept in plasma gun, there is pressure gradient between inside of the gun and outside. The pressure gradient makes arc plasma out from the gun without any bias voltage. This plasma is referred to as background plasma in this thesis. The background plasma gives effect of

increased radius of the flux rope, a , and/or can act as an ideal wall condition. These two effects can be understood as stabilizing effects for kink instability (increased threshold current)[26].

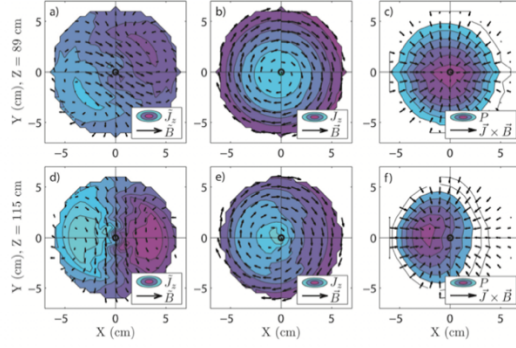


Figure 2.6 Coherent motion. Taken from figure 12 of [25]

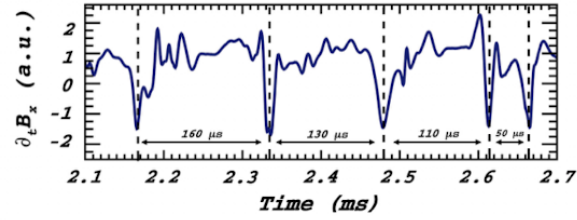


Figure 2.7 Chaotic, incoherence motion. Taken from figure 5.6 of [27]

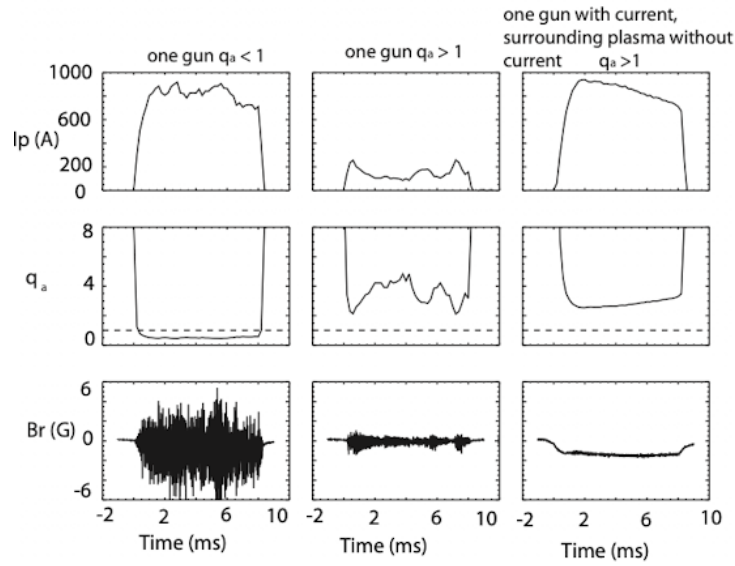


Figure 2.8 The effect of background plasma. Taken from figure 4.11 of [26]

2.3. Magnetic reconnection and merging of flux ropes

Magnetic reconnection is a topological change of magnetic field lines in the presence of plasma[28]. This process is an essential part of nature such as the evolution of solar flares, coronal mass ejection, and interaction of solar winds with the magnetosphere of Earth. In the laboratory, this process can be seen in fusion plasmas as a consequence of tokamak sawtooth crashes and IRE[29]. Moreover, this process can convert magnetic energy to plasma kinetic energy[30]. The detailed physics of magnetic reconnection differs according to the field of plasma research. Figure 2.9 show the simple 2D reconnection layer developed by Sweet and Parker[31]. When the two-field line with opposite directions meet, the sum of the magnetic field becomes zero, and the all-compressive stress is supported by the plasma. The plasma reacts to the stress, flowing two reconnected field lines out. Note that this Sweet-Parker model is used for highly collisional plasma as the compressive stress is supported by the plasma.

For the understanding of collisionless magnetic reconnection physics, significant progress has been done[32]. When it comes to collisionless magnetic reconnection, the two-fluid effects become important. The two-fluid generalized Ohm's law in steady state is

$$\mathbf{E} + \mathbf{v} \times \mathbf{B} - \frac{\mathbf{J} \times \mathbf{B}}{en_e} + \frac{\nabla P_e}{en_e} = \eta \mathbf{J} \quad (2.2)$$

where ∇P_e is the electron pressure tensor, \mathbf{E} is the electric field, \mathbf{B} is the magnetic field. The Hall term, $\mathbf{J} = en(\mathbf{v}_i - \mathbf{v}_e)$, has two species. Note that the two fluid means both the electron and ion flow are considered simultaneously. When the reconnection layer is on the order of the ion inertial length, the ions become demagnetized while the electrons do not and thus the diffusion of two flow are different (The magnetic field lines remain frozen into the electron fluid.). The simple schematic of collisionless two-fluid magnetic reconnection[33] is shown at figure 2.10.

During magnetic reconnection, ion heating was observed. In the first paragraph in this section, it is mentioned that the magnetic energy can be converted to plasma kinetic energy during magnetic reconnection. The detailed process of ion heating was suggested by the appearance of the in-plane electric field that accelerates ions in the reconnection region, which was governed by electron dynamics[34], as shown in figure 2.11. The governing equation for this site is the electron momentum equation at the X-point,

$$n_e m_e \frac{dv_e}{dt} = -en_e(E + v_e \times B) - \nabla \cdot \bar{P}_e + en_e \bar{\eta} \cdot J \quad (2.3)$$

where η is the resistivity tensor and v_e is the electron velocity. By taking the R component of Equation 2.3,

$$E_R = -V_{eY}B_Z - \frac{1}{en_e} \frac{\partial p_e}{\partial R} \quad (2.4)$$

can be achieved[34]. Based on this relation, Further useful relation that can describe the scaling of the field strength with plasma parameters was driven by [15]. By integrating the above equation, the radial potential well scaling is achieved,

$$\Delta\phi \approx \frac{B_Z^2}{2\mu_0 e \langle n_e \rangle} + \Delta T_e \quad (2.5)$$

where B_Z is the reconnecting field strength, $\langle n_e \rangle$ is the electron density averaged over R, and ΔT_e is the electron temperature drop across the current sheet. Finally, when the mono-energetic beam assumption described in Section 2.1 was applied, the scaling of ion temperature during reconnection with the operation parameter was driven.

$$\Delta\phi \approx I_{inj} \sqrt{V_{inj}} \quad (2.6)$$

This relation will be used to evaluate merging process at Chapter 4 as,

$$\Delta T_i \propto \Delta\phi \propto I_{inj} \sqrt{V_{inj}} \propto \frac{B^2}{n_e} \quad (2.7)$$

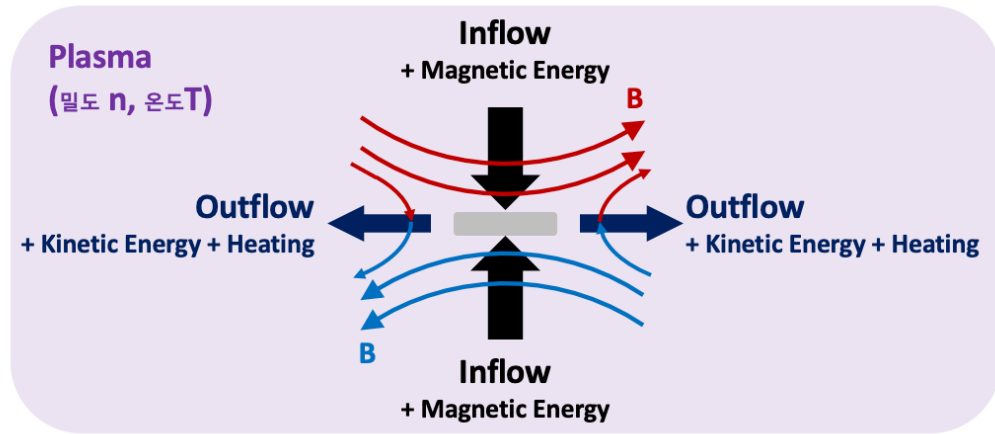


Figure 2.9 Magnetic reconnection layer in 2D

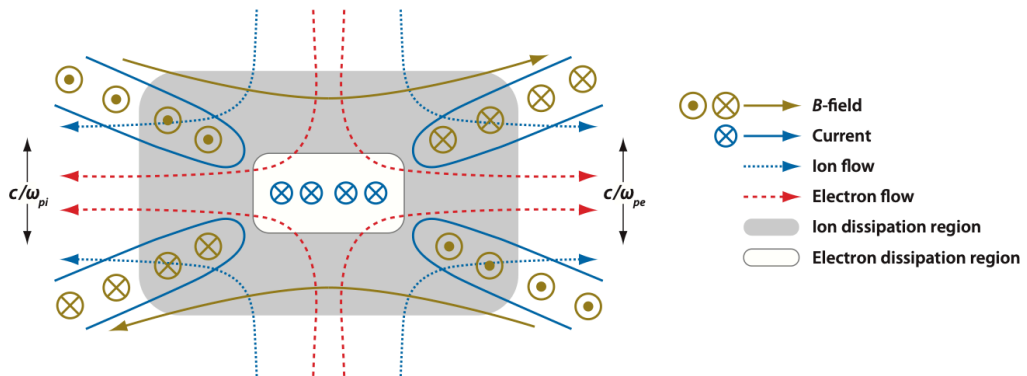


Figure 2.10 Collisionless reconnection layer, Taken from figure 4 of [33]

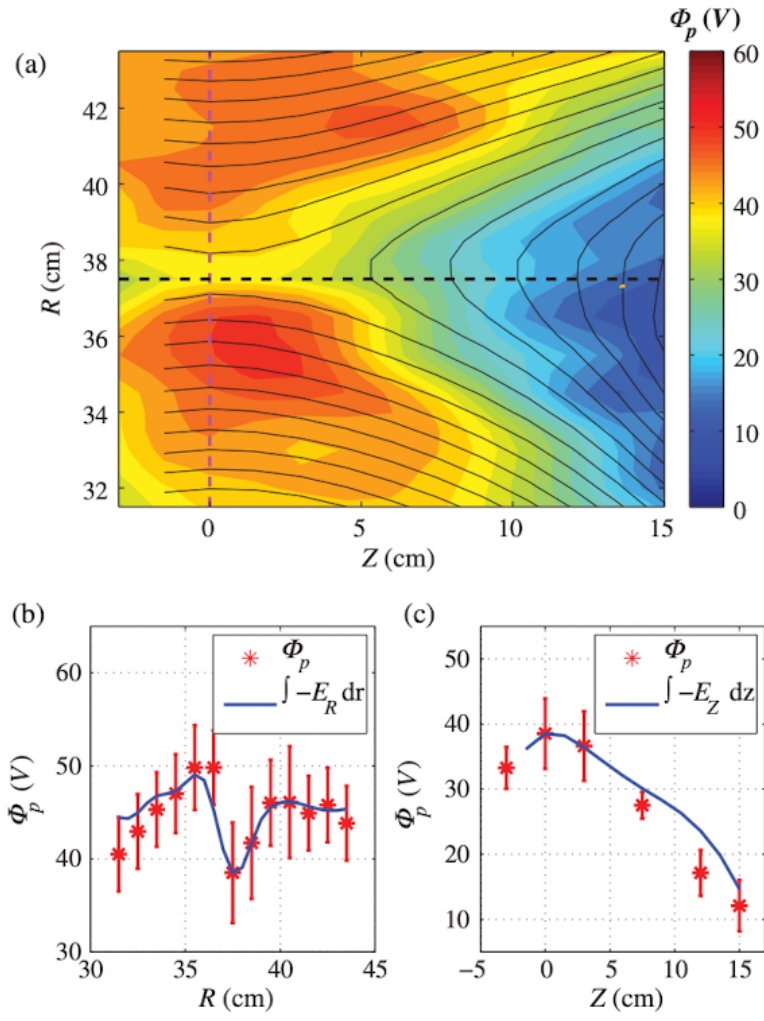


Figure 2.11 Taken from figure 2 of [34]

When there are two colliding flux ropes, they can merge via magnetic reconnection. Extensive experimental studies regarding the merging of two colliding flux ropes are conducted, and it suggests an experimental threshold for merging[35]. Not only the attraction force but stagnation force is measured during the merging process, as shown in figure 2.12. This implies there is stagnation in the merging process. At some condition, it was shown that two mutually attracting flux ropes can bounce back, which imply two flux rope are not always merge[36], as shown in figure 2.13. These findings suggest the attraction force and instability on flux rope may not be enough trigger force for merging. Thus, when the merging of two colliding flux ropes is expected and needed, the onset condition should be proposed for fast and sufficient merging.

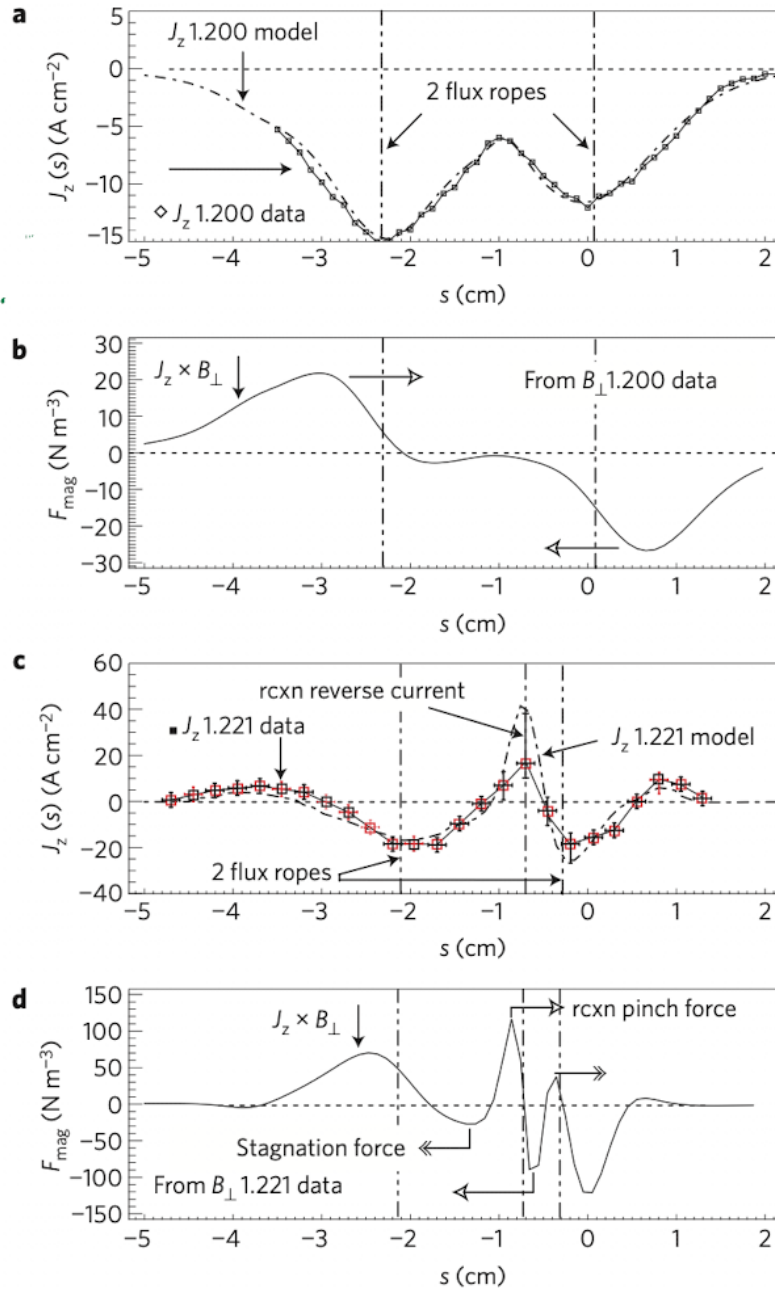


Figure 2.12 Taken from figure 5 of [35]

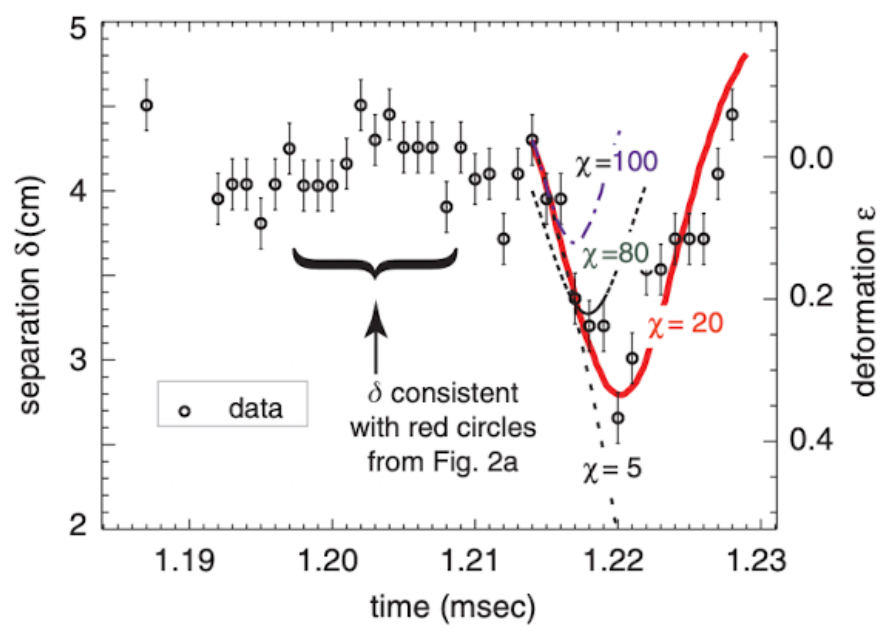


Figure 2.13 Taken from figure 3 of [36]

2.4. Magnetic Helicity Conservation and Taylor Relaxation

The magnetic helicity, K , is a physical parameter that quantifies the linkage of magnetic flux in a closed volume. With ideal MHD conditions, the total magnetic helicity is a conserved quantity. This parameter is a global parameter, so it is useful when addressing the state of plasma. The definition of magnetic helicity, K , is

$$K \equiv \int A \cdot B dV \quad (2.8)$$

where A is magnetic vector potential and B is the magnetic field.

In a toroidal system such as tokamak and ST, there are two magnetic flux components; 1) Toroidal flux, 2) Poloidal flux. Normally, the toroidal field(flux) is set as constant by the external power system. So, the increasing K of tokamak plasma means increasing plasma current as poloidal flux is proportional to plasma current. This relation is shown in figure 2.14. Thus, the relation of $K \propto I_p \Psi_{tor}$ is reliable.

By differentiating Equation 2.8, the time-variant of helicity can be driven,

$$\dot{K} = -2 \int E \cdot B dV + 2\Psi \frac{d\psi}{dt} - 2 \int V_{inj} B \cdot dS \quad (2.9)$$

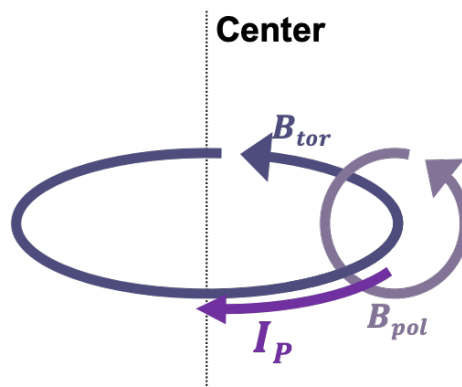
where Ψ is toroidal flux, $E = \eta J$, η is the plasma resistivity, J is the toroidal current density. The first term of RHS means the volumetric resistive helicity dissipation. It is worth noting that helicity dissipation has only a linear dependence upon current, as compared to the quadratic dependence of energy ($W \sim \eta J^2$) dissipation. The second term of RHS means the time-variant AC helicity term. The time-variant term in it means loop voltage of plasma similar to ohmic. The last term of RHS is the time-variant DC helicity. By applying a negative bias to the electrode (bounding surfaces), magnetic helicity can be injected electrostatically (DC). The magnetic helicity in a volume can be dissipated or increased by adjusting all these three terms in RHS. In this thesis, the last term, DC helicity, is a basis that describes LHI technique. In context, a brief explanation is here. By using

an arc plasma gun, the DC helicity injection technique can be met. The area, $\int dS$, is the cross-section of the extraction hole. Then, the injection voltage, V_{inj} , is applied to the chamber. The B is the magnetic field that is normal to the area.

For a more intuitive picture that describes the helicity injection process, the Taylor state, $\nabla \times B = \lambda B$, is used[37, 38]. As mentioned in the previous paragraph, the dissipation rate of helicity and energy is different. The relaxation means the process minimizing the magnetic energy under constant helicity, $\min(W - \lambda K)$. Here, the λ is constant eigenvalue. Each plasma has its own λ for a given condition, and λ can be used to represent its plasma state. The magnetic helicity can flow along the gradient λ . The experimental picture that describes this process is shown in figure 2.16. The flux rope (colored as blue), the plasma that provides helicity to be injected, has more helicity than plasma (colored as purple) in closed flux surface, the plasma to be injected helicity. The red arrows present the flow of helicity, redistributing the current/helicity from injected scale to the global scale.

A small toroidal device, CDX, demonstrated the DC helicity injection discharge, by use of only an external electron beam[39]. The process of DC helicity is addressed as the injected electron beam flows around the main plasma at the edge while helicity is transferred radially to the main plasma with the beam, as shown in figure 2.16. Recently, the PEGASUS team has suggested the macroscopic plasma current driven based on the magnetic measurements during LHI operation[40]. The dynamo EMF-driven toroidal current for the measured fluctuating magnetic signal is reported, as shown in figure 2.17.

Toroidal system:
 K represents the linkage of toroidal and poloidal fluxes



$$B_{tor} \sim \text{constant}$$

$$B_{pol} \propto I_P$$

Figure 2.14 Magnetic helicity in toroidal system.

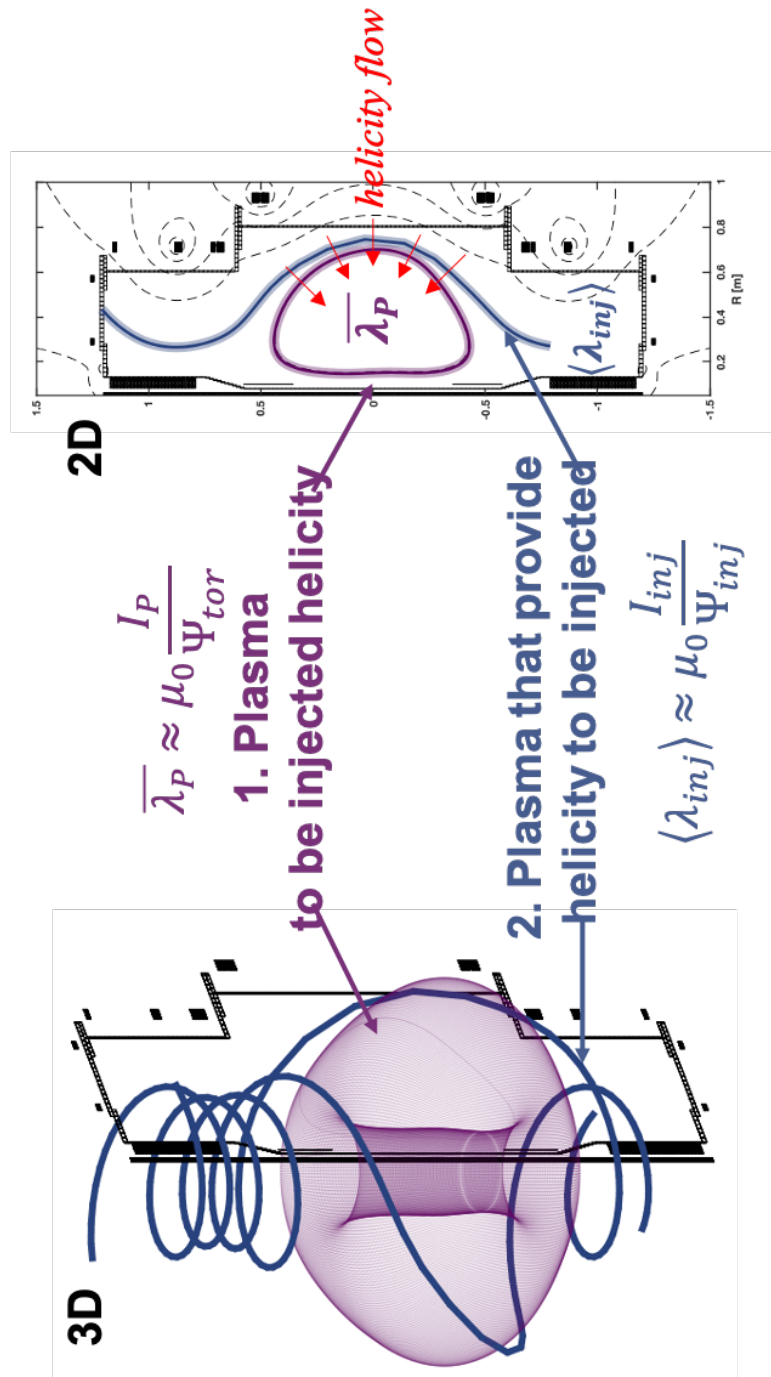


Figure 2.15 The experimental picture of helicity flow using 3D helical flux rope

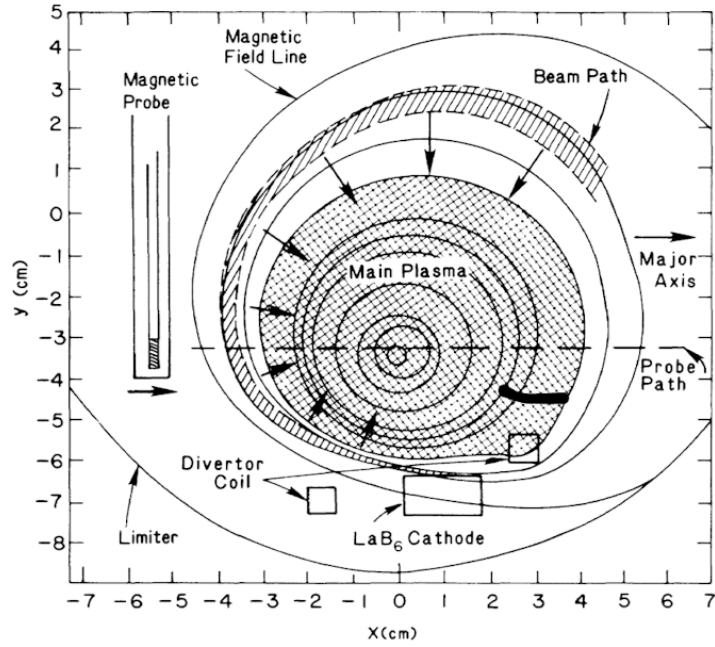


Figure 2.16 Taken from figure 1 of [39]

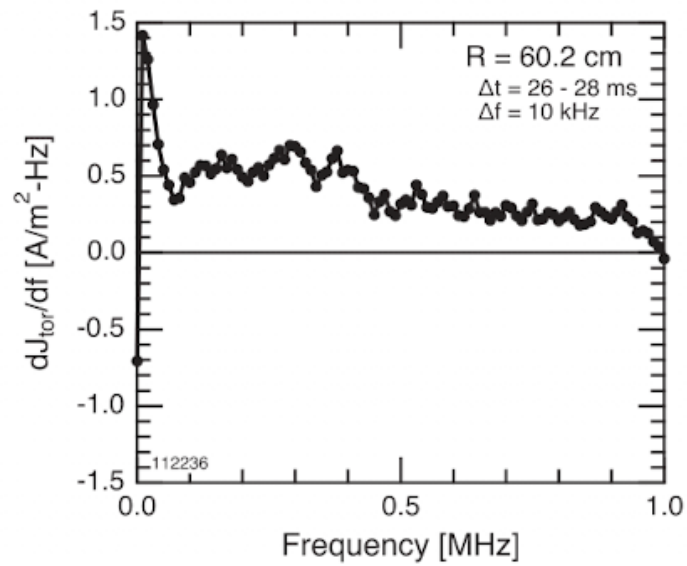


Figure 2.17 Taken from figure 5 of [40]

Chapter 3. Experimental Setup

3.1. The VEST Machine

Versatile Experiment Spherical Torus (VEST) is the very first Spherical Torus (ST) in South Korea, which is constructed at Seoul National University[41, 42]. Its distinctive feature is the elongated chamber that can be divided into three parts; upper, middle, and low chamber. Figure 3.1 show the schematic specification and field coil configuration. VEST has a low-aspect-ratio ST with $A < 1.37$. There are many ports sized 3.7-10 inches on the wall and plates (top and bottom). The 24-turn toroidal field coil set that can drive a toroidal field of 0.18 T is installed, and it has been operated using an ultracapacitor power bank. The poloidal field of 10 sets is installed around the chamber. The vertical location of coils can be varied according to experiment purpose and requirements. Normally, PF #6, #9, and #10 are used for the equilibrium field. The power system for PF coils simply consists of a cap bank, SCR, and coil. The controllable power system is underdevelopment. At the center stack, the PF #1 as an ohmic coil is installed. In addition, PF #2 coils are installed at two vertical ends. The base pressure of 10^{-7} is maintained by a turbomolecular pump and two cryogenic pumps. Daily Glow Discharge Cleaning process proceeds every morning. The gas injection (fueling) for discharge was made by using a Piezo gas valve.

The active studies of ST physics such as innovative start-up, non-inductive heating and Current Drive (CD), high beta, disruption, innovative divertor concept, and energetic particles are ongoing. Recently, an Internal Reconnection Event (IRE) during a disruption of Ohmic operation is the main research topic[29]. Note that, normally, the VEST discharge has been made with the ohmic coil (PF1) and/or pre-ionization using wave-neutral gas discharge. However, in this thesis, the ohmic coil was never used for the experiment as the successful non-inductive CD is the main goal of the thesis. The pulse

lengths of typical ohmic discharge are up to 20 ms, which is limited by VEST TF, PF power system.

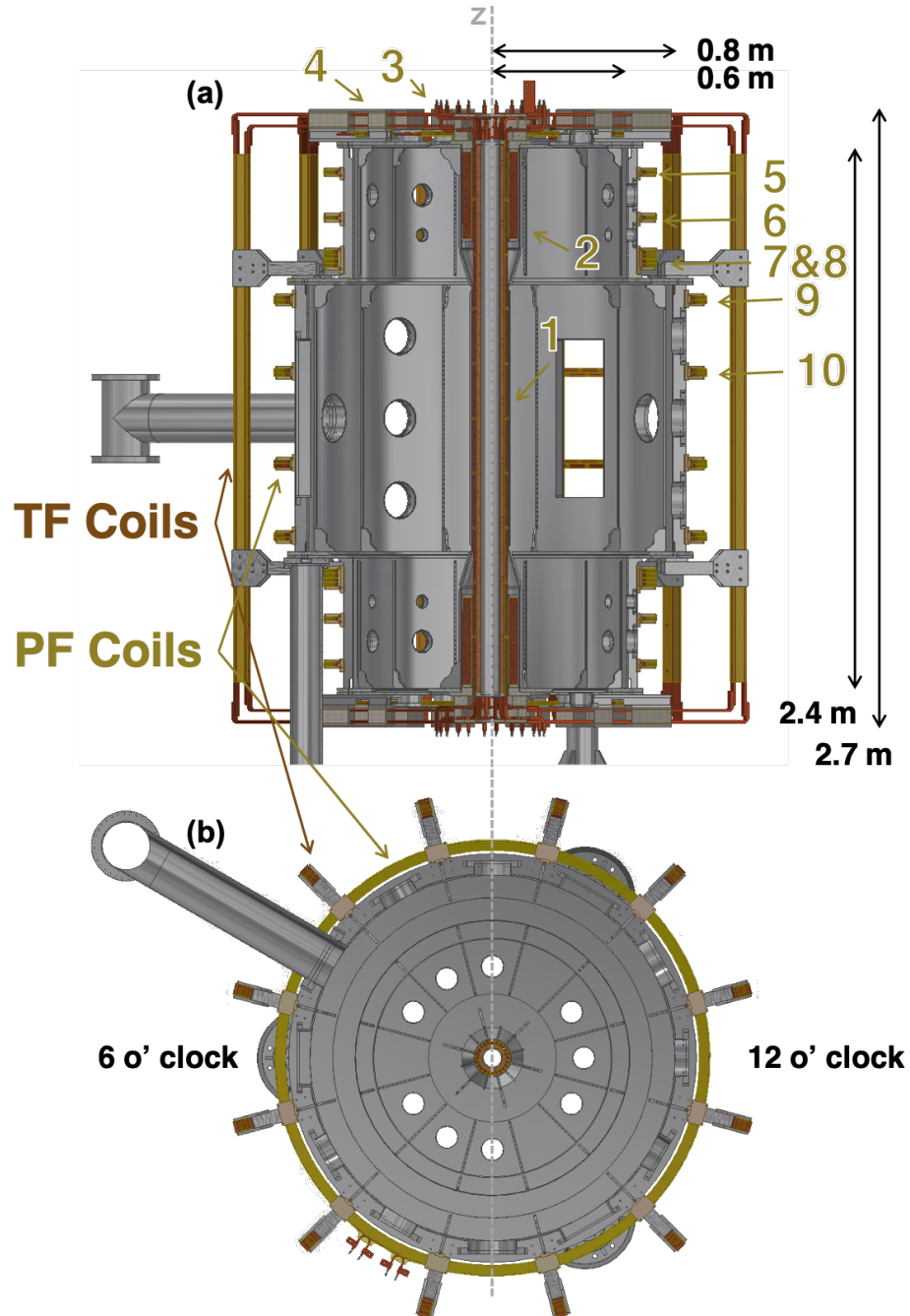


Figure 3.1 (a) VEST cross section showing field configuration and size.
 (b) VEST cross-section Top view (Cutaway at $Z = 0$)

3.2. Diagnostics

VEST has operated various useful diagnostics for both ohmic and LHI operations. Among those, magnetic diagnostics and Ion Doppler Spectroscopy are the most important for experiments in this thesis. In this section, the diagnostics used for this thesis will be introduced.

3.2.1. Magnetic diagnostics

To measure both the poloidal magnetic field component and the MHD activity in VEST, magnetic pickup coils are installed along with the center stack (inboard side) and the interior of the vessel wall (outboard side). The inboard array has 27 pickup coils, whereas the outboard array has 22 pickup coils [43]. The positions of the vertically distributed arrays of the pickup coils are shown in Fig. 3.2. In addition, a Rogowski coil that poloidally encloses the interior of the vessel wall is used to measure the toroidal plasma current, as depicted dotted-orange line in Fig. 3.2. In this study, four magnetic pickup coils are selected, as shown in Fig. 3.2. Three magnetic pickup coils on the inboard side (I02, I11, I25) and one magnetic pickup coil on the outboard side (O11) are selected based on the distance between the coils and flux ropes. The sampling rate for data acquisition is 2.5 M/s.

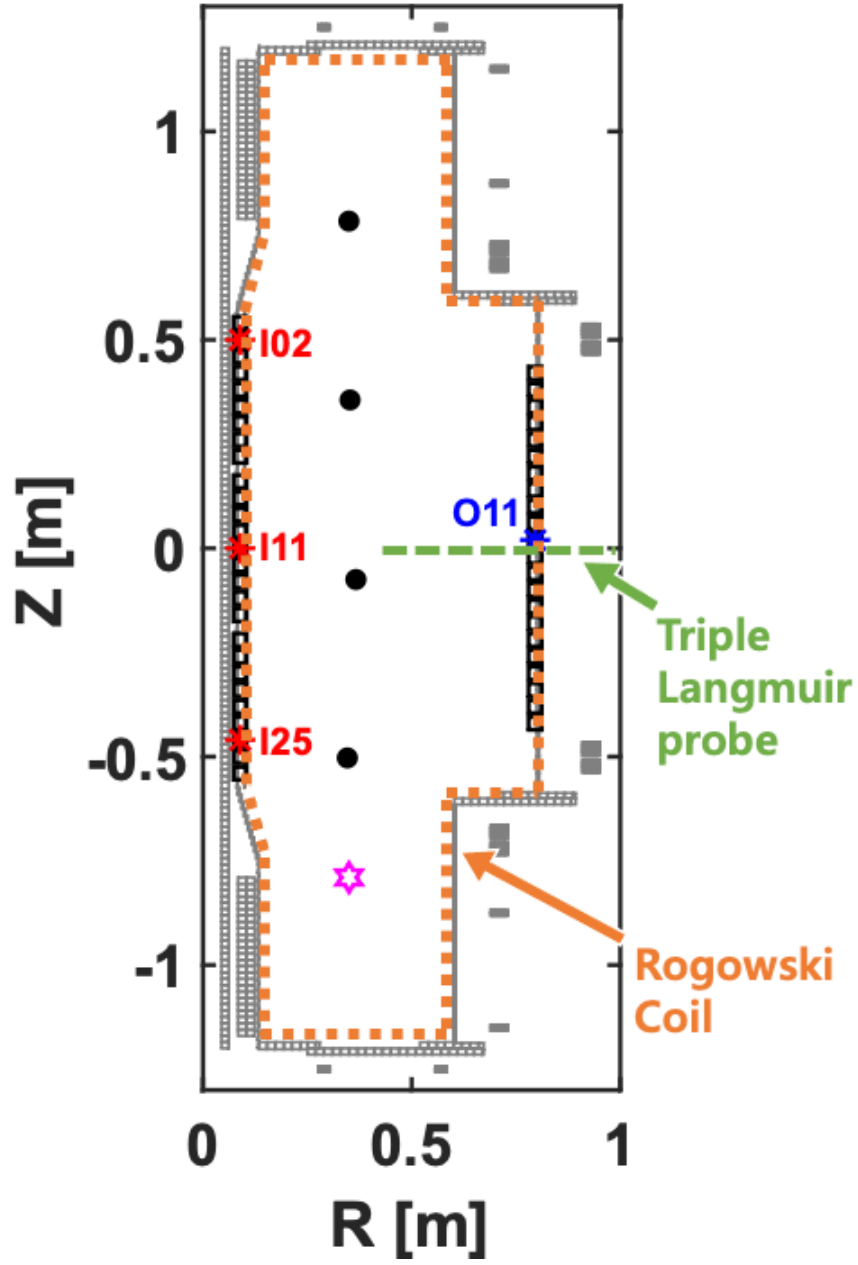


Figure 3.2 toroidal cross-section of VEST. The magenta hexagram indicates the location of the arc plasma gun. The black circles indicate the locations of flux rope used in this study at the toroidal location of the magnetic pickup coil array.

3.2.2. Spectroscopies

3.2.2.1. Ion Doppler Spectroscopy

The Ion Doppler Spectroscopy (IDS) in VEST measures and observes radiation emitted by electrons during atomic energy transitions(changes) in multiply ionized impurity ions. The detailed description of IDS on VEST and diagnostic principles are well described in [29]. The CIII (464.72 nm) is the strongest impurity line in VEST and is used for this thesis to evaluate reconnection activities. Note that the wavelength range for IDS measurement in VEST is 462-474 nm. The measurement time resolution was set as 1kHz (1ms), which is the highest for 10ch usage. As the raw signals were line-integrated, the Doppler tomographic inversion proceeded to get a radial profile that ranged from 0.39-0.7 [m]. The single gaussian fitting was used for spectra analysis. The error bar in IDS measurement results was made from the fitting and inversion process. The calibration has been done every use day to overcome possible errors in measuring.

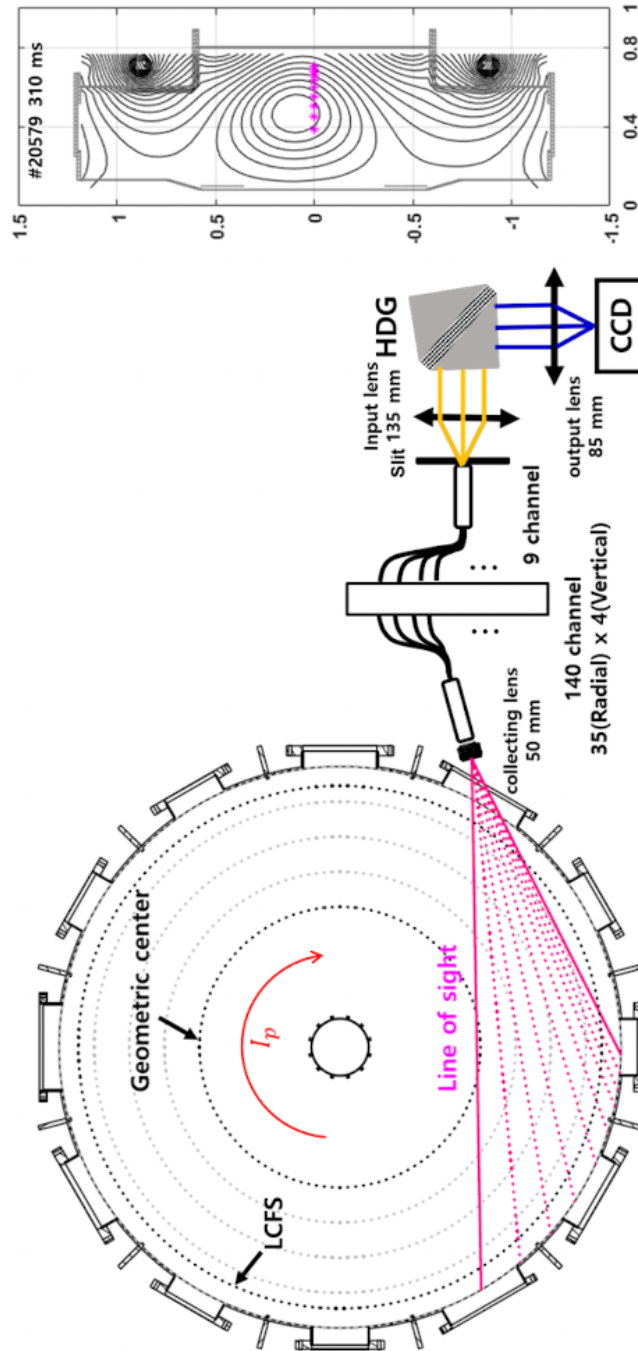


Figure 3.3 Schematic view of IDS system in VEST [29]

3.2.2.2. Filterscope

The filterscope diagnostic system using photomultiplier (PMT) is developed for measuring the time evolution of radiation emitted by several impurity ions during discharge. This system consists of collection optics, Beam splitters (Dichroic mirrors), PMTs and DC power supplies as shown in Fig 3.4. The seven visible spectral lines for measuring are selected; H_{α} (656.3 nm), H_{β} (486.1 nm), H_{γ} (434 nm), O_{II} (441.5 nm),

O_V (650.0 nm), C_{II} (514.0 nm), C_{III} (465.0 nm). To effectively ensure the same line of sight for each impurity line, only one collecting line was installed at $Z = 0$ [m], then the intensities(light) were filtered out as light passed each Dichroic mirror. The calibration has also proceeded, and the signal gain of PMTs was controlled by DC power supply. The

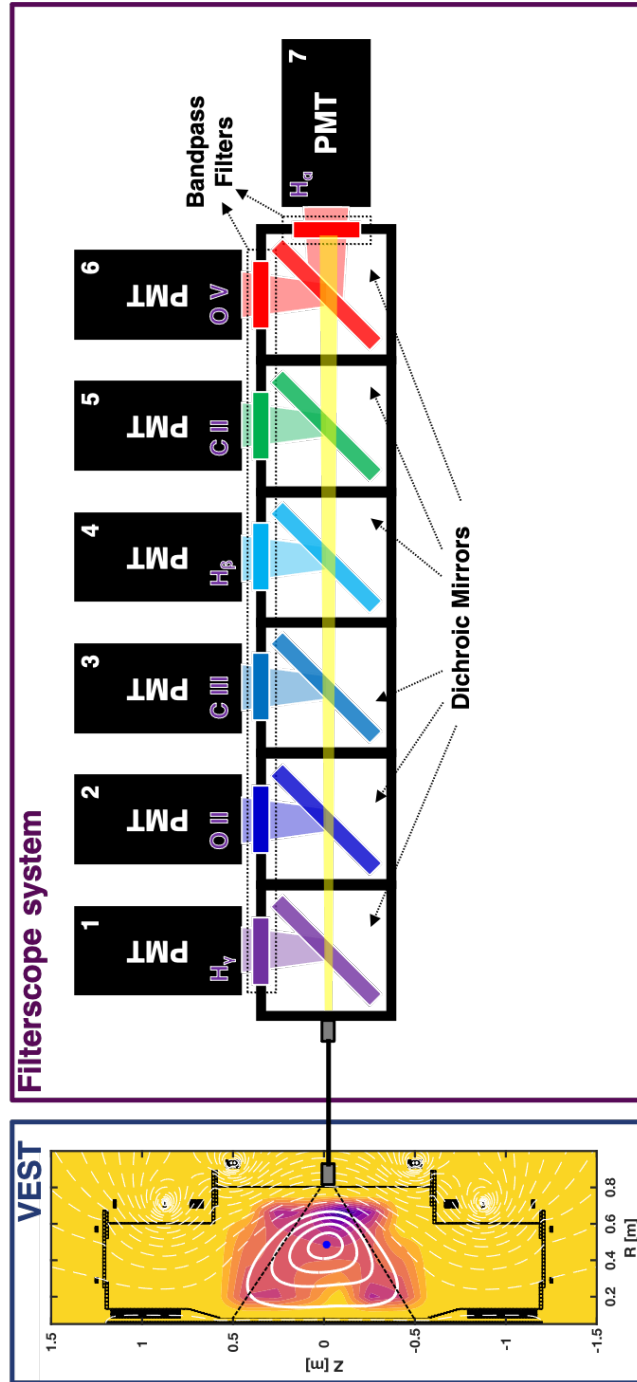


Figure 3.4 Filterscope system in VEST

3.2.2.3. Fast Camera

The fast camera was used, allowing direct observation of flux ropes, their behavior and evolution. However, the camera exposure time is 0.4 ms, which is excessively lengthy for capturing the behavior of plasmas. To get a full range of chamber (1024*1080), this is the maximum rate for imaging. The fish-eye lens was used, giving full vision from the bottom to the top plate. The useful camera projection code considering fish-eye lens code was developed [44], and it is used to get flux rope length and 3D passes of the flux rope. Figure 3.5 show one of the examples. The yellow dots indicate the conversioned-vacuum-field-following-calculation results.

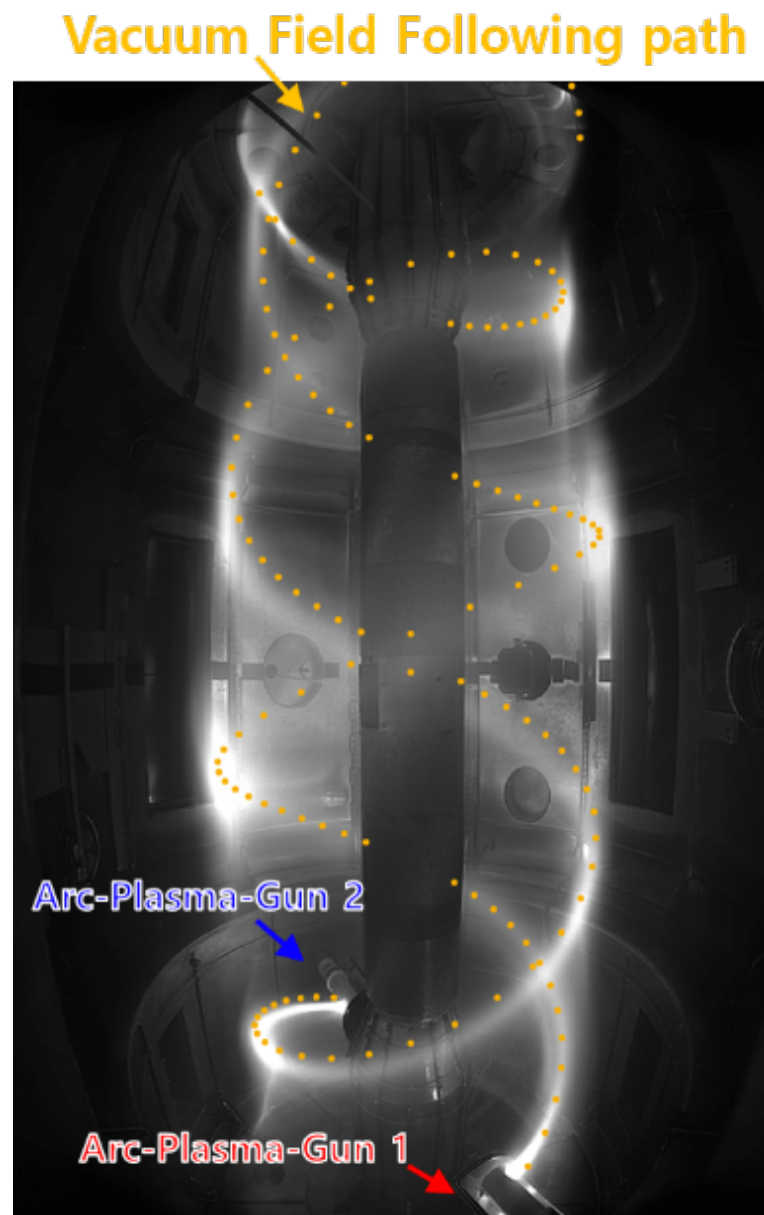


Figure 3.5 Fast camera image of discharges in this study.

3.3. Helicity injection system

For the practical operation of DC helicity injection in ST, two hardware parts/systems are required; 1) The arc plasma guns and 2) Pulsed power systems. These two systems can determine the performance of the current drive via DCHI. Thus, its developments and commissioning are important as much as its operation. In this chapter, DC helicity injection systems developed for several years in VEST are presented.

3.3.1. Arc plasma guns

The first version of the plasma gun (also known as electron source) [45] and its schematic diagram are shown in Figure 3.6. A pulsed electron source based on the plasma washer gun has advantages such as high current density, clean operation, and compact size [17]. The pulsed electron gun consists of hollow cold cathode, anode, and washer stacks that are made up of molybdenum. The arc discharge is generated between the cathode and anode while washer stacks are used to make the arc discharge channel stable between the electrodes [17, 46]. The washer stack is composed of alternating insulating material and metal washers. The metal washer has 10mm inner diameter with 2mm thickness while the ceramic washer, used for the insulating material, has 20mm inner diameter with 2mm thickness. Since the size of the arc channel is defined by the washer stack, the length and diameter of a typical arc channel formed in the electron gun are 26 mm and 10 mm, respectively. Note that each metal washer is electrically floating and isolated by insulating washers. The cathode has been designed as a hollow cold cathode for efficient arc discharge formation with 20 mm inner diameter and 22 mm depth. A piezoelectric valve is used for gas injection through the center of the cathode. The ceramic cup covering the electron gun is installed to bias the source anode of the electron gun with respect to vacuum chamber wall (not shown here). The electron gun has been assembled into a stainless-steel pipe and installed on bottom plate of vacuum vessel. Power and gas

lines to the electron gun are fed through the stainless-steel pipe with electrical insulation from the vacuum vessel. It is designed to be able to adjust the vertical location of the electron gun. For the initial helicity injection experiments, the electron gun is installed at $R=0.5$ m, $Z=-0.625$ m, and integrated into the main control and data acquisition system of VEST[47]. After the voltage is applied across the electrodes of the electron gun, hydrogen gas is injected through the piezoelectric valve to initiate arc discharges.

For more reliable and increased power capability, VEST has operated a DC helicity injection system consisting of two miniaturized arc plasma. The two arc plasma guns with miniaturized-arc-chambers are newly designed based on the previous version, and they can discharge magnetic flux ropes with high currents of up to 2 kA each in 10 ms as shown in Fig. 3.7 and 3.8. The two arc plasma guns are installed with a support-stainless-steel pipe at the side wall of the lower chamber of VEST through a 3.75 inch port, which is located at $Z = -0.79$ m, as shown in Figures 3.7 and 3.8. These arc plasma sources are separated toroidally by 180° and have freedom in terms of both angle-adjustable and radially movable features. For the flux rope discharge and its merging study (chapter 4), the radial position of each arc plasma gun was set to 0.35 m, and 0.27 m for the helicity injection experiment (chapter 5). The gas, hydrogen, is delivered to each arc plasma gun through the cathode of the miniaturized-arc-chamber by a small commercial solenoid pulse valve installed in the support-stainless-steel pipe on the air side. The metal (tungsten) washer has 22mm inner diameter with 2mm thickness while the ceramic washer, used for the insulating material, has 26mm inner diameter with 2mm thickness. Since the size of the arc channel is defined by the washer stack, the length and diameter of a typical arc channel formed in the electron gun are 14 mm and 22 mm, respectively.

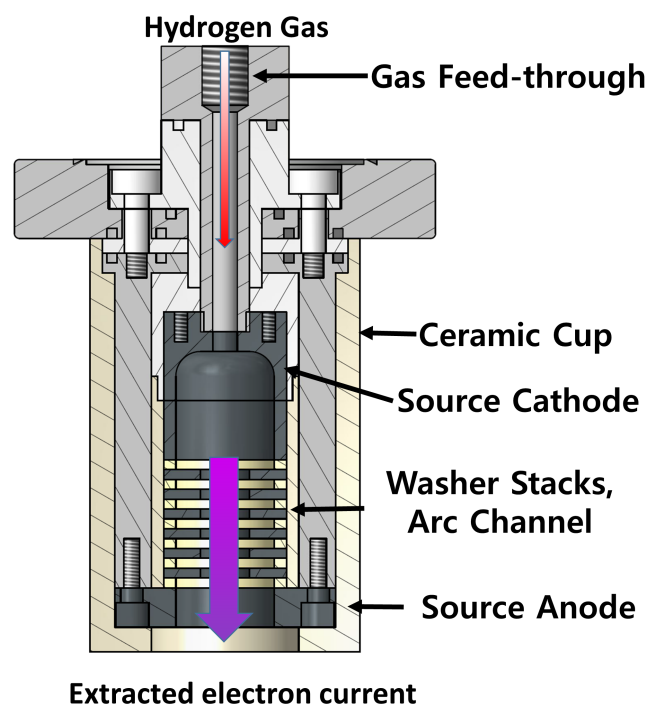


Figure 3.6 A schematic diagram of early version of pulsed electron gun.

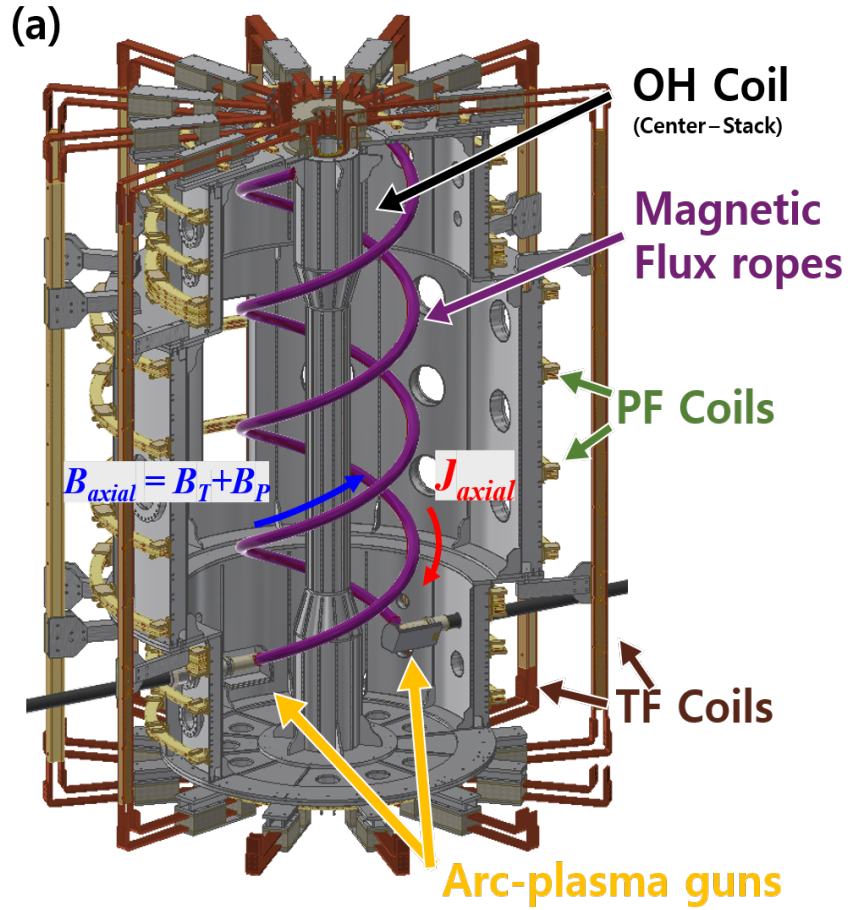


Figure 3.7 (a) Cutaway schematic of the VEST device with local helicity injection system, and (b) toroidal cross-section of VEST. The magenta hexagram indicates the location of the arc plasma gun. The black circles indicate the locations of flux rope used in this study at the toroidal location of the magnetic pickup coil array.

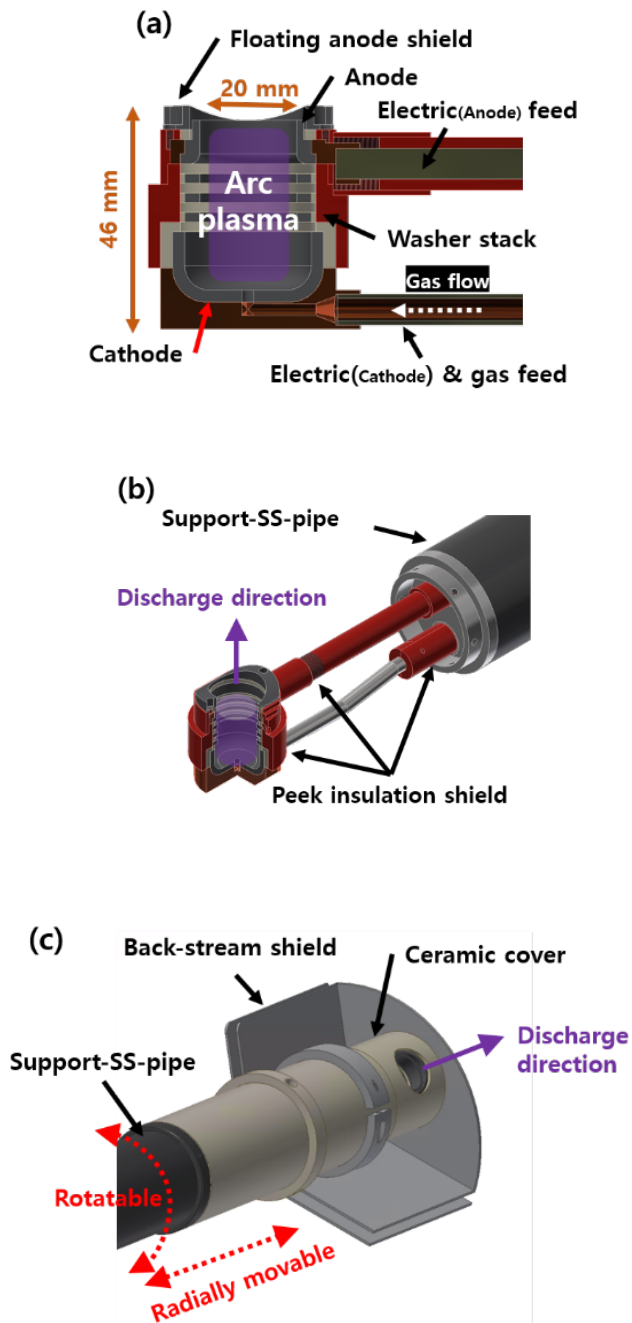


Figure 3.8 Schematics of newly designed arc plasma gun. (a) Miniaturized arc chamber, (b) Feedthrough, (c) Outer housing and fully assembled arc plasma gun.

3.3.2. Pulsed power systems

The pulsed power is an essential part of not only fusion but DC helicity injection. Two pulsed power systems are required for DC helicity injection using an arc plasma gun. The one for arc plasma discharge in plasma gun as a high-density electron source, the other for injection as flux rope discharge. DCHI system in VEST have utilize two different pulsed power systems, such as a single power supply and two power system. The single power supply system was used in the past, then two power supply was used to date.

A single pulse power system for the VEST helicity injection system has been designed with a pulse forming network that consists of capacitors, inductors, and switches[48]. It is designed to provide a square current waveform for the pulse duration of 5 ms (very early version). The capacitance and inductance of the pulse power system is designed to be 0.94 mF and 0.30 mH , respectively in consideration of the impedance matching and pulse duration. With the designed values, the impedance of the pulse power system, ZPFN is $\sim 0.5 \Omega$, which is similar to the expected plasma impedance estimated from the preliminary experiment. The charging voltage of 1.2 kV of the pulse power supply has been used throughout the experiments.

An experimental circuit diagram of the single power system is shown in Fig.3.9. It is characterized by the use of a single pulsed power for both arc discharge formation and electron current injection. Before arc discharge is formed in the electron gun, almost all voltage from the power supply is applied between the electrodes of the gun to initiate the arc discharge inside the gun. After the arc discharge is formed, the voltage across the voltage divider resistance increases sufficiently enabling the injection of the electrons into the vacuum vessel since the impedance between electrodes of the gun decrease by plasma formation. The injected electron current from the electron gun flows toward the vacuum chamber wall, establishing a new injection impedance between the gun and the chamber wall, Z_{inj} . Since Z_{inj} is much smaller than the R_{div} , the voltage across the anode of the

electron gun and the vacuum vessel is mainly defined by Z_{inj} , adjusting the extraction of the electrons. In this manner, the single power supply can drive both arc discharge and injection.

The circuit simulation of the pulse power system is depicted in Fig. 3.10 (a) as well as the measured injection voltage and current, which shows a good agreement and confirms that the single pulse power can be used for the helicity injection properly.

The impedance matching is an important issue for the pulse power system to deliver maximum power to the load since voltage and current waveforms are determined by the impedance matching condition between the pulse power supply and the load. As shown in Fig. 3.10 (b), the load impedance, Z_{load} is a sum of arc impedance and injection impedance. It is obvious that the injection impedance should be influenced by the magnetic field structure (so, the pass length), since the electron current injection length that the electrons should travel until they hit the vacuum vessel depends on the geometric stacking ratio. The impedance of pulsed electron gun during arc discharge, Z_{arc} is also affected by magnetic field strength on the gun. Therefore, the load impedance is expected to be significantly affected by the magnetic field structure during the helicity injection.

The effect of the magnetic field structure on the load impedance has been investigated in VEST in the various field structure, which can be utilized for the impedance matching of the pulse power supply and consequently efficient helicity injection. The experiments have been conducted at B_T of 0.1 and 0.05 T, and B_Z of 6, 4.5, and 3 mT. The injection length of each magnetic field structure is accurately estimated by using a field line following analysis considering vacuum vessel eddy currents and non-uniform vertical field.

The arc impedance and injection impedance as a function of the injection path length in various field structures with its linear fitting are shown in Fig. 3.10 (b). Magnetic field strengths satisfying impedance matching conditions for maximum power efficiency can

be identified by comparing with the pulse power impedance of 0.5Ω as shown in Fig. 3.10 (b). The toroidal and vertical magnetic field strengths for the most impedance matching condition, in which the path length of electron current is ~ 8.6 m, are found to be ~ 47 mT and 8.2 mT, respectively. This result indicates that the load impedance of each magnetic field can be estimated based on the injection length and the pulse power supply can be adjusted for the impedance matching and consequent efficient helicity injection.

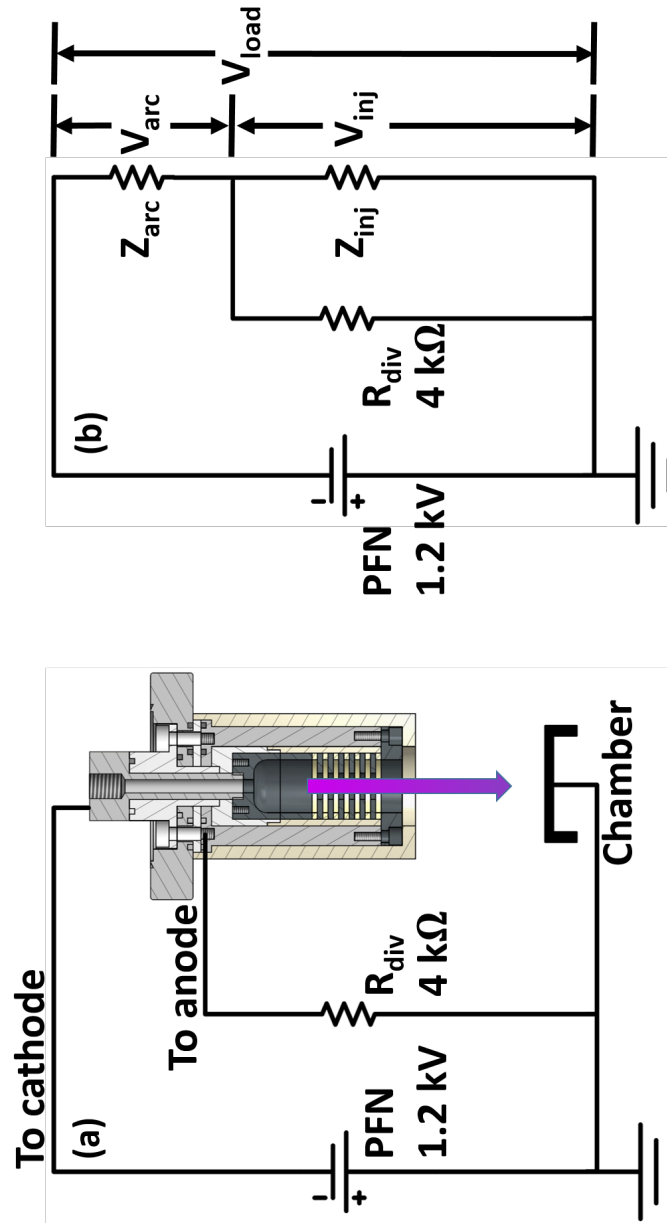
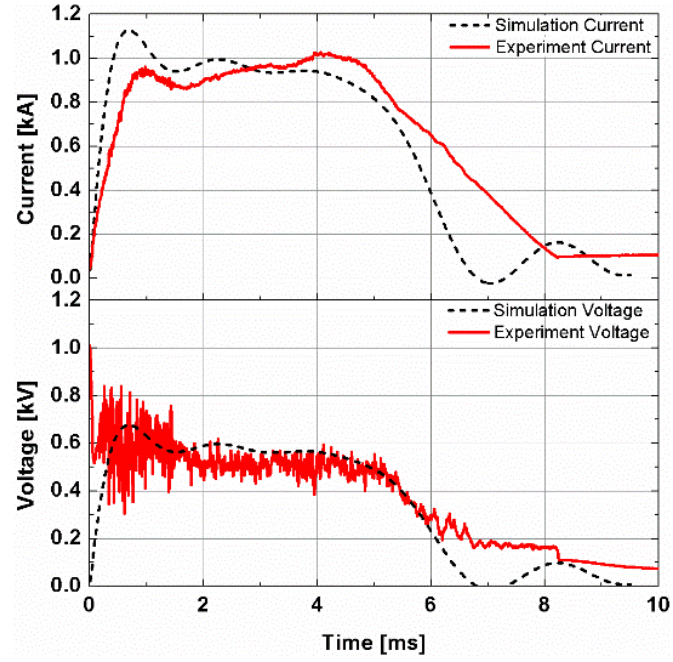
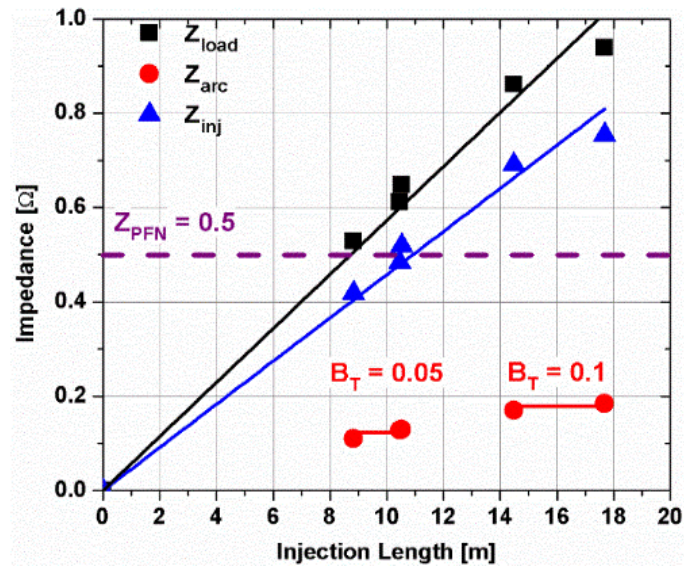


Figure 3.9 (a) An experimental circuit diagram of the helicity injection system, and (b) an equivalent circuit during discharge.



(a)



(b)

Figure 3.10 (a) Comparison of simulated and measured injection current (top) and voltage (bottom) and (b) load impedance, arc impedance and injection impedance as a function of the injection length.

The newly developed high-pulsed power system consists of two pulsed powers that are one for arc plasma source and the other for flux rope discharge power respectively. In figure 3.11, a schematic of the pulsed high power system circuit is shown. The flux rope discharge power is connected to two arc plasma sources in parallel, sharing the electric power during discharge according to its impedance. Note that the impedance of discharged magnetic flux rope can be controlled by using two valve gas injection system. According to experiments, flattop pulse length for both arc and flux rope discharge can be adjusted up to 10 ms, which is doubled compared to the previous system[45]. Pulse Forming Network (PFN) is used for arc plasma source in injectors. The PFN is a functional circuit that shapes current waveform into a square wave[48]. The capacitance and Lab-made inductances are 1.56 mF and 62 μ H respectively. Two PFN are developed and connected to each arc plasma source. Note that in order to deliver optimized power, the characteristic impedance of the PFNs is matched with arc plasma impedance of 0.2 ohm that obtained previous experiment results[45], as shown in Fig 3.12. To attain prompt initiation of arc discharge in injectors, each PFN is connected to a sparker in series that provide a transient voltage of 2 kV by an isolated transformer for a few microseconds at the beginning of each discharge, as shown in fig 3.12 (a) top graph. The flux rope discharge power is provided by the capacitor bank with a nominal total capacitance of 76.5 mF up to 2 kV as shown in figure 3.11. The Insulated-Gate-Bipolar-Transistors (IGBTs) with optimized gate driver and snubber circuit are used as the main switch that safely turns off the high current of up to 4.8 kA. To give static and stable impedance to the power system, the kanthal resistor of 0.2 ohm and shaping inductor of 0.1 μ H are added to the injection discharge circuit. Note that the magnetic flux rope has unstable and time-variant impedance according to its discharge state. The schematic and photos of the HI power system are shown in Figures 3.13-14.

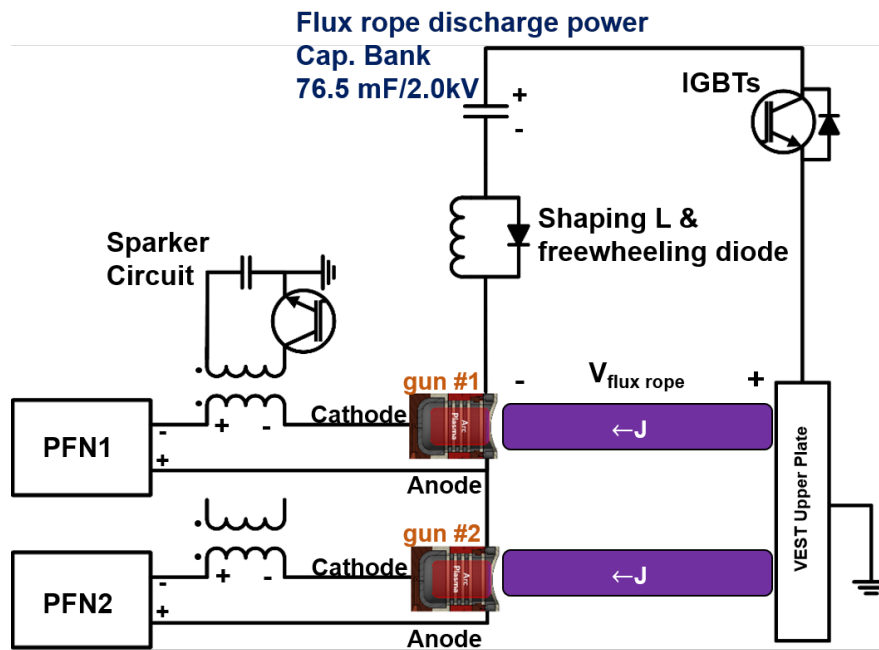


Figure 3.11 Circuit diagram of pulsed power system for magnetic flux ropes. When the arc plasma guns are negatively biased with respect to the VEST upper plate, the flux ropes are discharged. Shown are the pulse forming network (PFN), Insulated gate bipolar transistors (IGBTs).

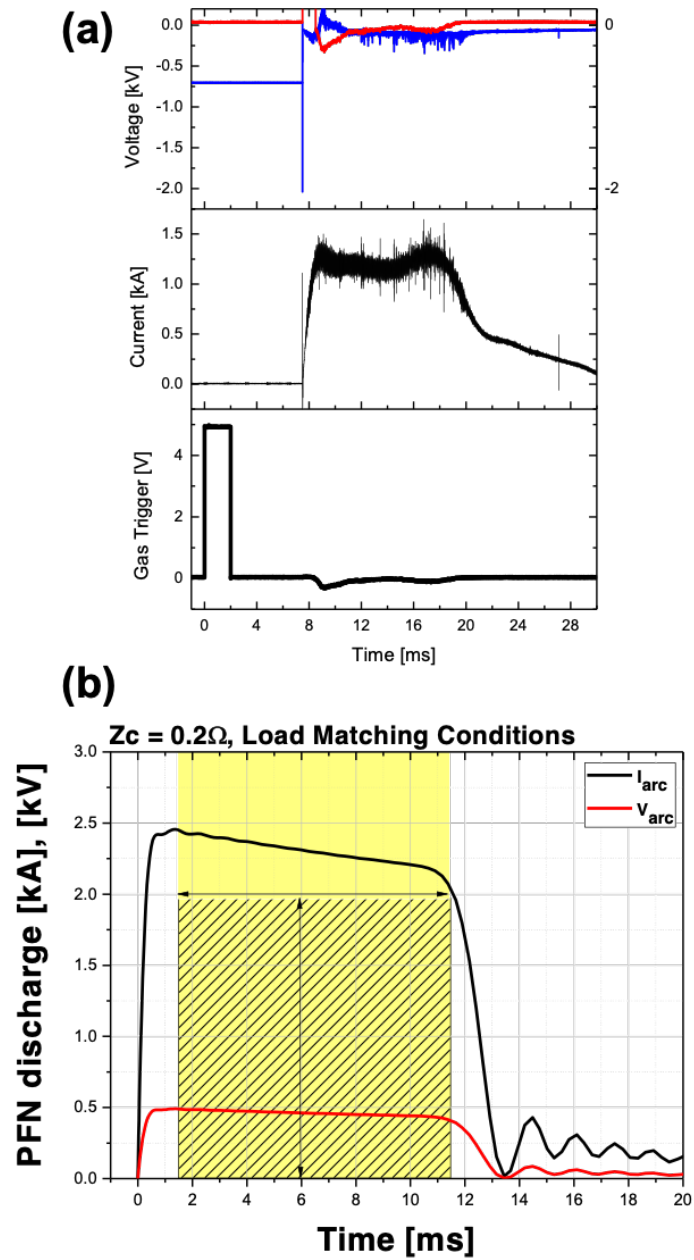


Figure 3.12 (a) Discharge results of PFNs with sparker circuit for arc discharge.
(b) Simulation results of PFN with matching condition.

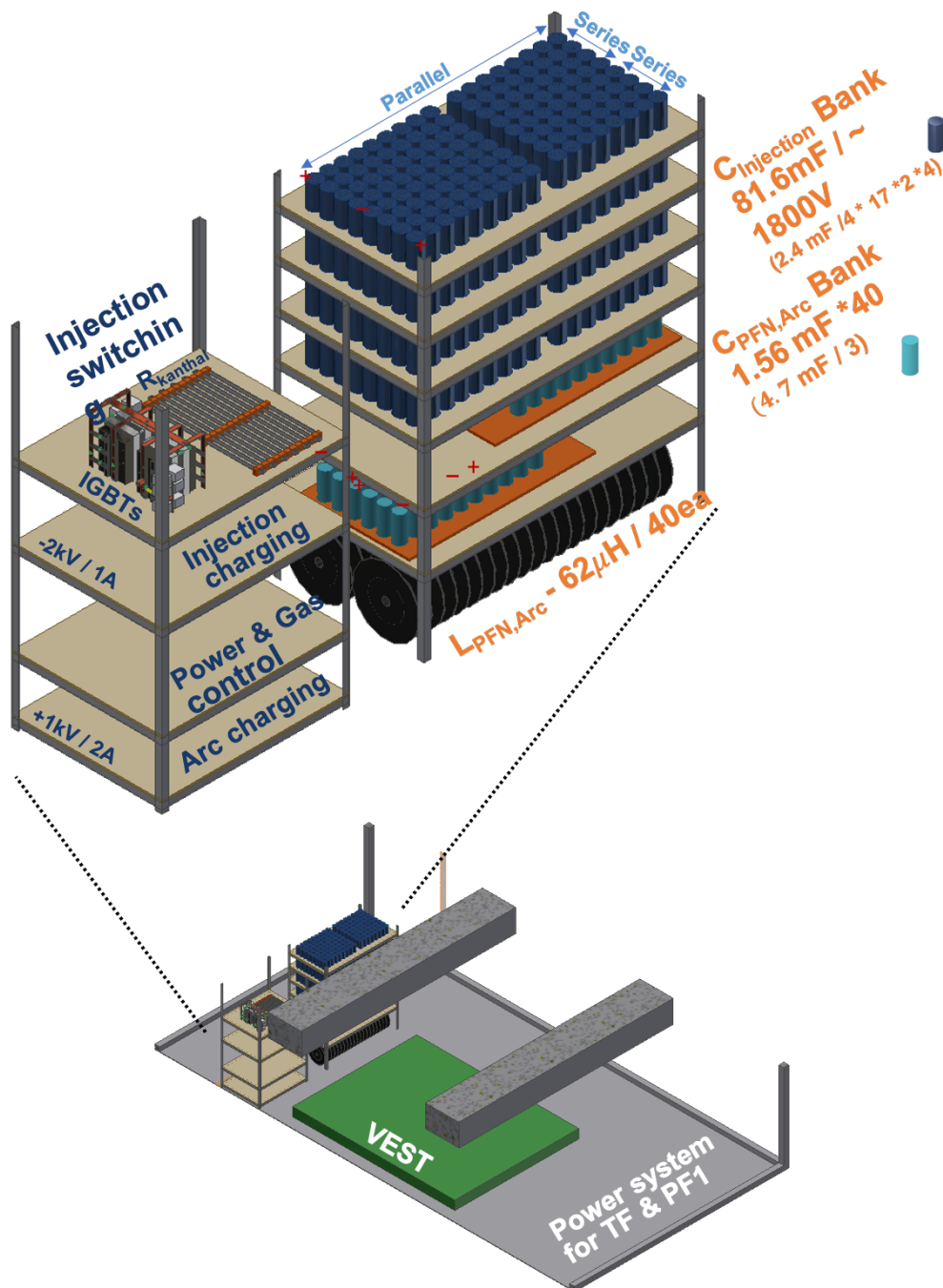


Figure 3.13 A schematic of Helicity injection power system for VEST



Figure 3.14 Photos of Helicity injection power system

3.3.3. Plasma gun operation

The discharge sequence starts by operating the solenoid valves connected to arc plasma guns. The amount of hydrogen gas delivered to the guns is adjusted via valve-open-time control. After 7ms, the arc discharge in the guns is initiated by using PFNs, and as the arc current reached its maximum current (not shown here), the arc plasma guns are biased with respect to the VEST chamber by the flux rope discharge power. A fraction of the arc plasma current in the arc plasma gun is extracted, and the magnetic flux ropes start to be generated along the magnetic field at the given gun locations. Figure 3.15 shows both typical discharge results and the impedance-controlled discharge results with its conditions. The impedance control of the magnetic flux rope at a given pulsed power is accomplished through the open-time control of the solenoid valve, which was used to limit the neutral gas. Blue triangles and red x markers curves indicate controlled discharge results for low and high current modes, respectively, showing that the current waveform increased over time as neutral gas is injected. The black cross markers in Fig. 3.15 show that a relatively high current is obtained through increases in both the gas injection and discharge power, which is normally used for LHI. Note that the flux rope discharge voltage decrease during discharge as the voltage of the capacitance bank undergoes droops.

The kink instability threshold obtained in a given experiment can be higher than the theoretical ideal current threshold. Another characteristic of the magnetic flux rope in VEST is the occurrence of background plasma diffusing out of the arc plasma gun before any magnetic flux rope current is extracted by the flux rope discharge power. This background plasma also follows the vacuum magnetic field at the given gun locations. In this study, the electron density, n_e , and electron temperature, T_e , are measured using a triple Langmuir probe that is radially scannable, located at $Z = 0$ m, as shown in Fig. 3.15(b). It is confirmed that the background plasma also can be controlled using both the pulsed power system and neutral gas injection for the arc plasma gun, as shown in Fig.

3.16. Note that the highest T_e location is 0.3 m, which is the radial point of the vacuum field following path for $Z = 0$. The higher the neutral gas fueling rate, the higher the n_e of the arc plasma in the plasma gun, thereby the n_e of background plasma is also increased [18, 19]. These background plasmas act like ideal walls (increased a), providing the flux rope with a kink stabilizing effect[26], giving an increased current threshold for kink. If the flux rope radius, a , is expanded to 30 mm by the presence of background plasma, the value of I_{KS} is increased from 22 A to 220 A.

There are two useful parameters to quantify both magnetic helicity injection regimes and the current drive capabilities of the particular injection system. The magnetic helicity injection regime can be described by $\lambda_{gun} \equiv \frac{\mu_0 I_{flux\ rope}}{\Phi_{axial}} \text{ m}^{-1}$ where μ_0 is the vacuum permeability, $I_{flux\ rope}$ is the flux rope current, and Φ_{axial} is the vacuum magnetic flux on the guns[49]. For the present VEST LHI system, the magnetic helicity injection regime can range from 4 to 800 m^{-1} . In addition, a parameter known as normalized effective toroidal loop voltage is introduced as $V_{norm} = \frac{A_{gun} V_{flux\ rope(in)}}{R_{gun}}$ for LHI[11] where A_{gun} is the aperture area of gun, $V_{flux\ rope}$ is the flux rope voltage with respect to the vessel, and R_{gun} is the radial position of guns. The typical V_{norm} value of the helicity injection system in VEST can range from 1.4 to 2.4 V-m. Based on the V_{norm} parameter, it can be seen that a high voltage operation of the plasma gun is required to add more V_{norm} for a given gun location. However, the main focus of our present study campaign is to find an appropriate position, R_{gun} , within a given power of up to ~1.5 MW rather than a higher voltage operation. Therefore, the current injector design, rotatable and radially movable, is adopted and operated, and new design for high voltage operation will be applied later.

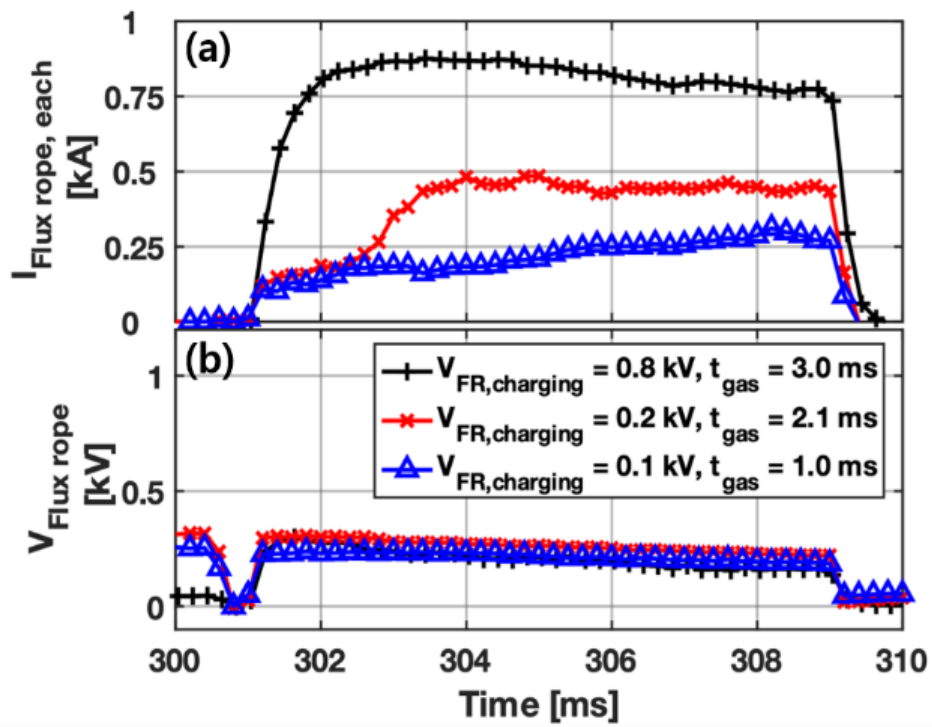


Figure 3.15 Typical discharge results. (a) Flux rope current for each arc plasma gun. Because there are two guns, the total flux rope current is twice that of the waveform. (b) Voltage for maintaining flux ropes. For LHI, the flux rope current and voltage are known as injection current, injection voltage respectively.

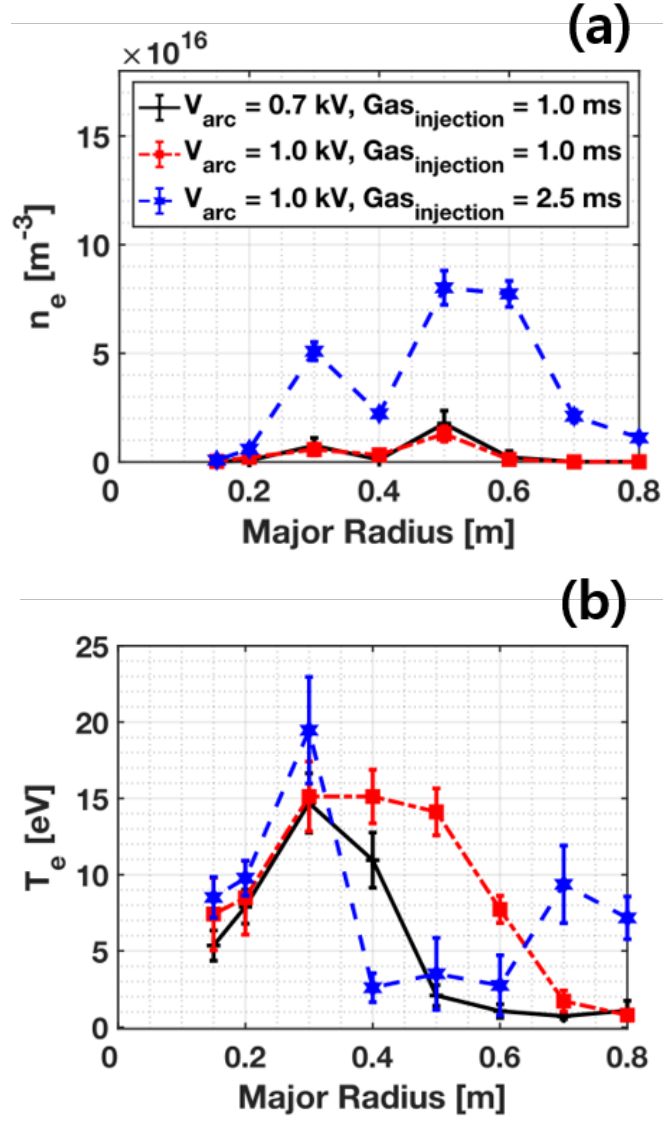


Figure 3.16 The radial profile of background plasma parameters is measured using a triple Langmuir probe at $Z = 0$ m of VEST. (a) Electron density, n_e , (b) Electron temperature, T_{eff} . Background plasma is extracted based on the pressure difference between the interior and exterior of the arc plasma gun. Flux rope discharge power is zero for these measurements.

Chapter 4. 3D helical flux rope merging

The flux ropes can be merged by attraction force, moving toward each other and the external kink instability. In our 3D configuration, the attraction force between ropes is acting on bi-directional (Z^+ and Z^-), so presumably, it does not give any contribution to merging. In addition, flux ropes follow the vacuum magnetic field line, only a time-variant magnetic field reducing the distance between ropes can trigger the merging process. The only remaining factor that can trigger merging is external kink instability. Also, given the appearance of kink mode in flux rope before merging between ropes reported by NIMROD as noted in Chapter 1, it is reasonable to expect kink unstable mode in flux ropes.

In this chapter, two focused experiments were performed to evaluate the MHD stability of flux ropes in 3D configuration and their merging activity. The axial magnetic field for flux rope is the sum of toroidal and poloidal fields, which is the main control knob in this chapter for a given power range.

One of the distinctive features of the magnetic flux ropes in VEST is its unique discharge path along the 3D helical magnetic field line. This does not allow the detailed measurement of internal information of flux rope such as current density profile, plasma pressure, and safety factor by using invasive measurements such as Langmuir probes and other probes. However, the state of a flux rope, i.e., whether it is kink-unstable or not, cannot be confirmed without the aforementioned data. To verify the global status of the flux rope following a 3D helical magnetic field, the magnetic measurements were analyzed in consideration of the fundamental properties of magnetic diagnostics. For a merging experiment, the IDS system as noted in chapter 3.2.2.1 is used to measure ion temperature, which is used for the evaluation of merging.

4.1. Kink instability in flux rope

4.1.1. MHD-Stable discharge

For context, here is a brief explanation of the arc plasma gun discharge. At the beginning of the arc plasma gun discharge, the electron beam is launched and accelerated up to the energy applied to the guns. This electron beam ionizes the neutral gas, resulting in the formation of bulk plasma. The discharged flux ropes are maintained by this beam–plasma interaction over the discharge time. Because this beam is in the plasma, the $n_{\text{beam}} \sim n_i$ relation is [18, 19], and through the use of this relation, the ion density can be estimated as a function of both $I_{\text{flux rope}}$ and $V_{\text{flux rope}}$.

Although the axial field is the 3D helical field for flux ropes in VEST, they may share the property of flux rope in a linear configuration. Before identifying any MHD instabilities that appeared in flux ropes, the flux ropes are discharged in highly stable conditions for a given discharge power. The vacuum axial field strength is set as 88 mT, which is bigger than the poloidal field driven by flux ropes. So, stable flux rope behavior is expected. Figure 4.1 show the three selected discharge results among the 25 scan shots. The shot 35681 in blue shows the highest OV/OII ratio and the lower pressure evolution ($E_{\text{ion,OV}} = 113$ eV, $E_{\text{ion,OII}} = 35$ eV). The shot 35655 in black, the highest discharge current, shows the low OV/OII ratio and the highest-pressure evolution. The shot 35667 in green shows the results between the 35681 and 35655. Figure 4.2 show the IDS measurement results. Interestingly, shot 35681 shows the ion temperature of 68 [eV]. In addition, the ion temperature decrease as injection power is increased. Note that the x-axis in figure 4.2 represents the injection power for a specific purpose, which will be introduced later in this chapter. Figure 4.2 (b) shows the ion velocities measured by IDS. Figure 4.3 show the IDS spectra example for selected shots in figure 4.2.

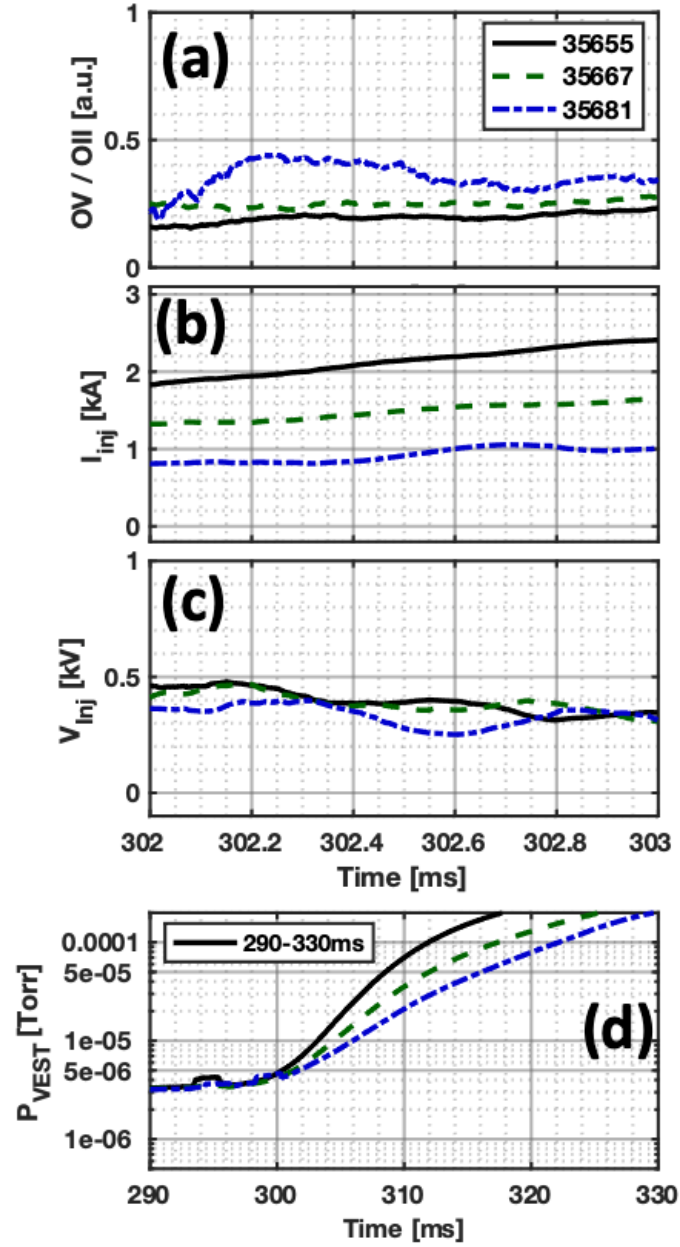


Figure 4.1. Three selected discharge result for high field strength scan. (a) line-integrated OV/OII ratio measured by filter scope. (b) total flux rope current. (c) discharge voltage. (d) neutral pressure time evolution.

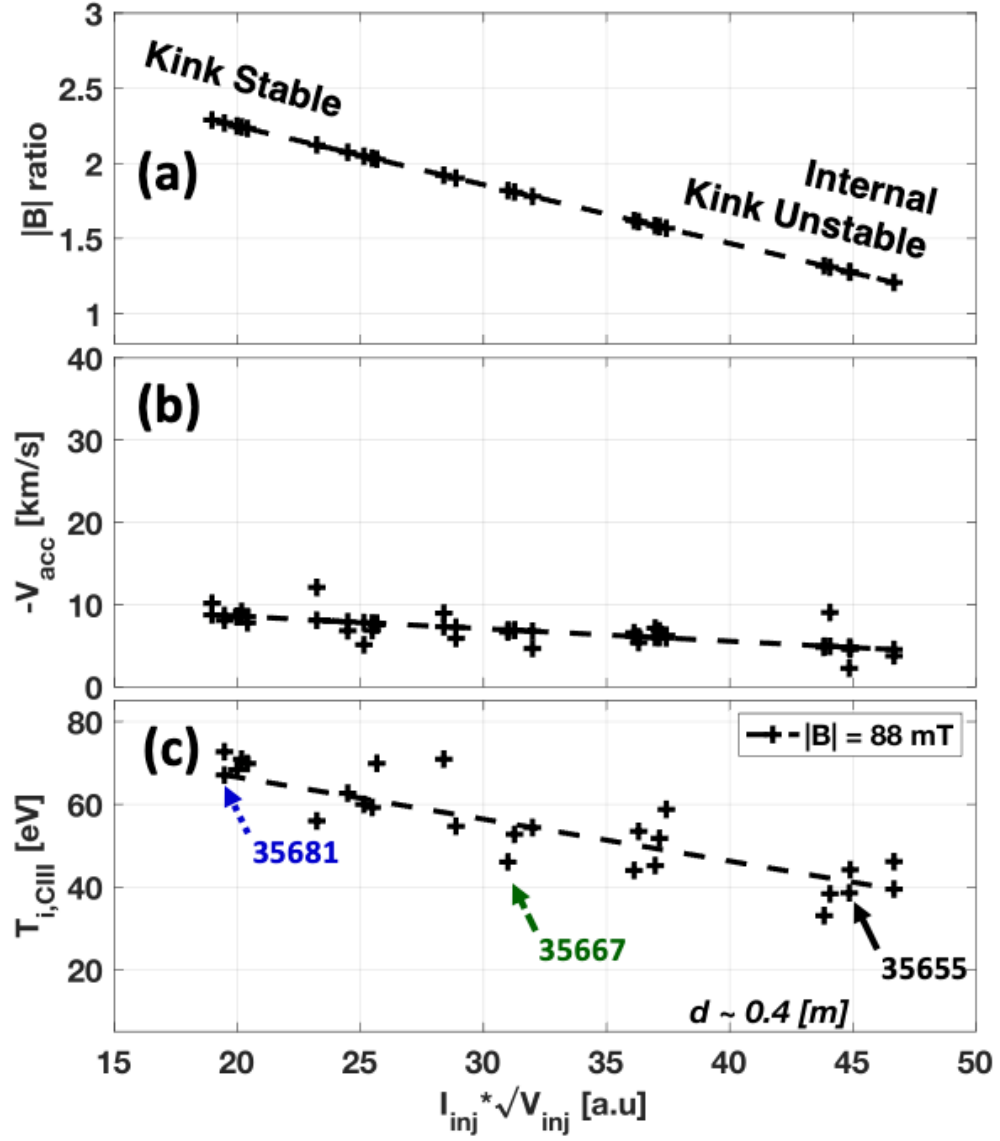


Figure 4.2 The IDS measurement results. (a) the ratio between vacuum field strength of 88 mT to poloidal field strength by flux rope. Note that high ratio value means more stable flux rope state. (b) Acceleration calculated from shift of CIII spectrum (c) Ion temperature of CIII impurity

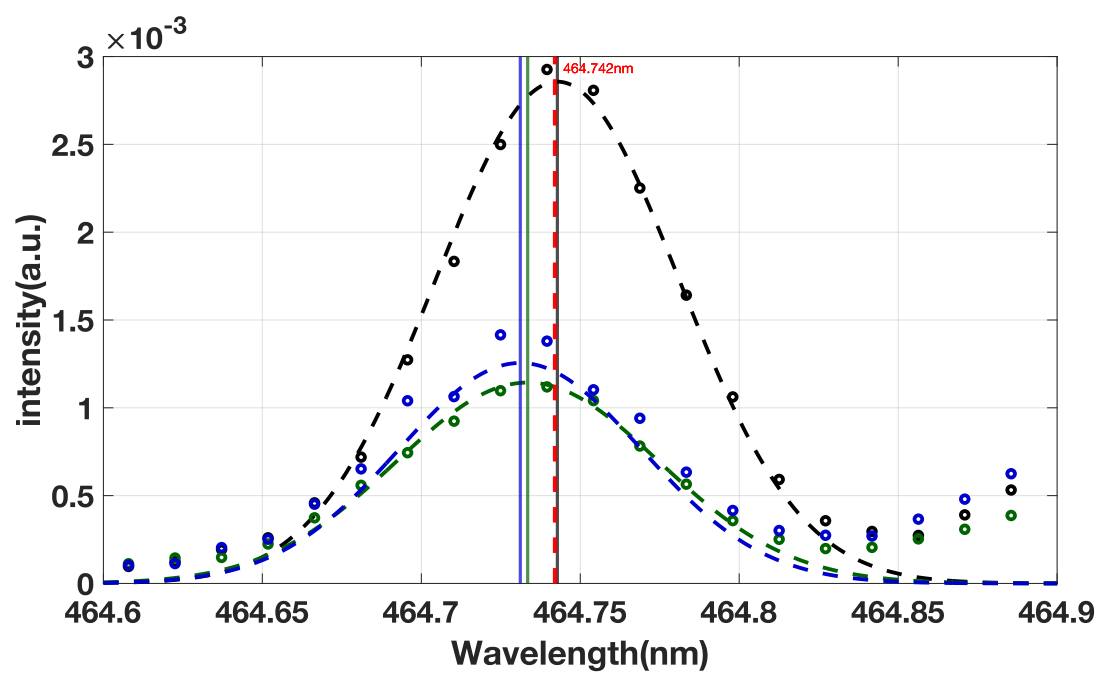


Figure 4.3 Example spectra corresponding three selected data in figure 4.2

It is worth noting that high ion temperature without acceleration means there is no magnetic reconnection activity. To check this presumption, the magnetic signal analysis and the simple calculation regarding a collision between neutral pressure and electron have proceeded. Figure 4.4 shows the cross-spectrogram results from the inboard magnetic pickup coil and Rogowski coil. The coherent signal on this graph means the flux rope undergoes the internal kink mode. So, the flux ropes of shot 35655 are in internal coherent kink mode while the other two shots do not show any meaningful signal. The way how to determine the kink state in flux rope by using spectrograms will be explained in next section 4.1.2. As shot 35681 show the highest OV/OII ratio signal in Figure 4.1, it is assumed its equilibrium electron temperature is around 50 [eV] while 30 [eV] for shot 35667 and 10 [eV] for shot 35655. The mean-free-path, electron-neutral collision frequency, and momentum transfer frequency are calculated and the results are in Table 4.1. Based on these results, it is reasonable to consider that in this condition, flux ropes simply obey the gas discharge physics. For shot 35681, the low neutral pressure condition results in collisionless plasma (relatively long mean-free-path and low collision frequency). This collisionless plasma may keep the ion temperature high as they do not interact with other species. On the other hand, shot 35655 shows the short mean-free-path and high collision frequency, meaning the plasma and neutral pressure strongly interact compare to shot 35681. Thus, they do not keep their temperature, so bulk plasma has decreased temperature. Note that, the high ion temperature of shot 35681 is not contributed by magnetic reconnection activity, and the acceleration in figure 4.2 (b) is not changed according to injection power, which supports the claim of no reconnection activity in this condition. Figure 4.5 show the fast camera image of each shot. The bright image of shot 35655 also supports the claim that a relatively strong-interactive-plasma state.

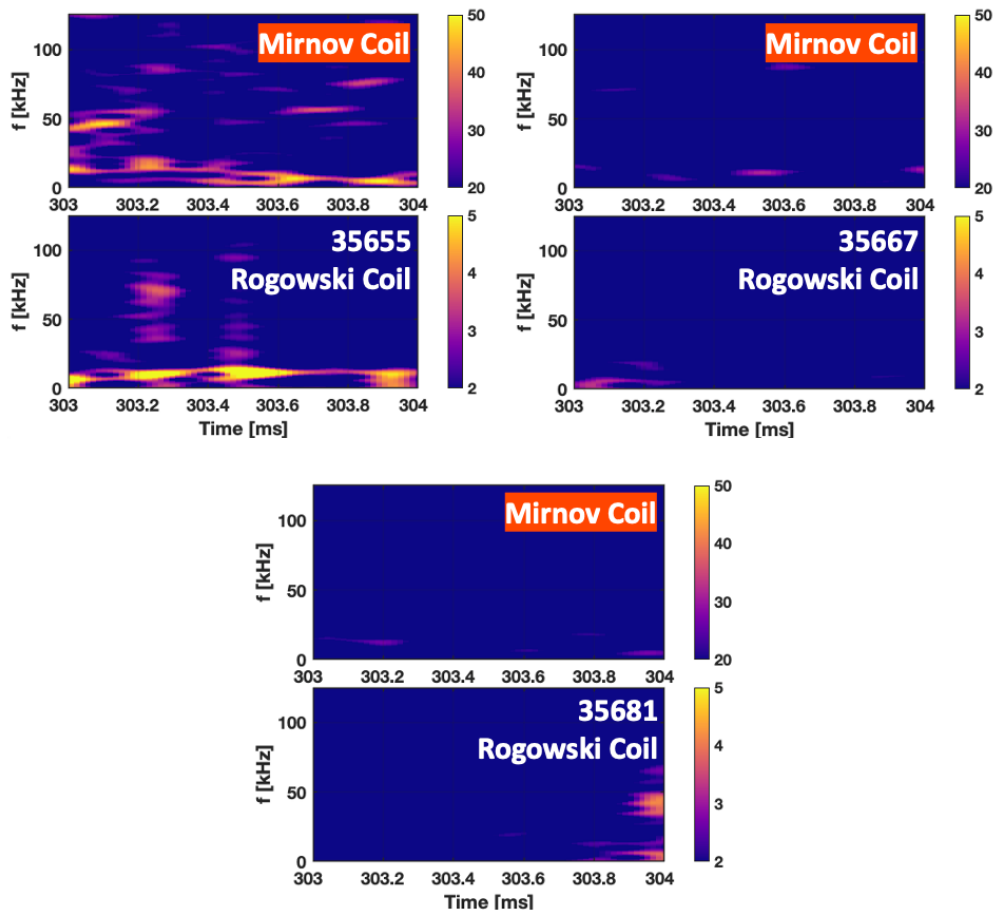


Figure 4.4 The spectrogram from inboard magnetic pickup coil and the Rogowski coil in VEST. The coherent signal of shot 35655 means flux ropes undergoes internal kink mode.

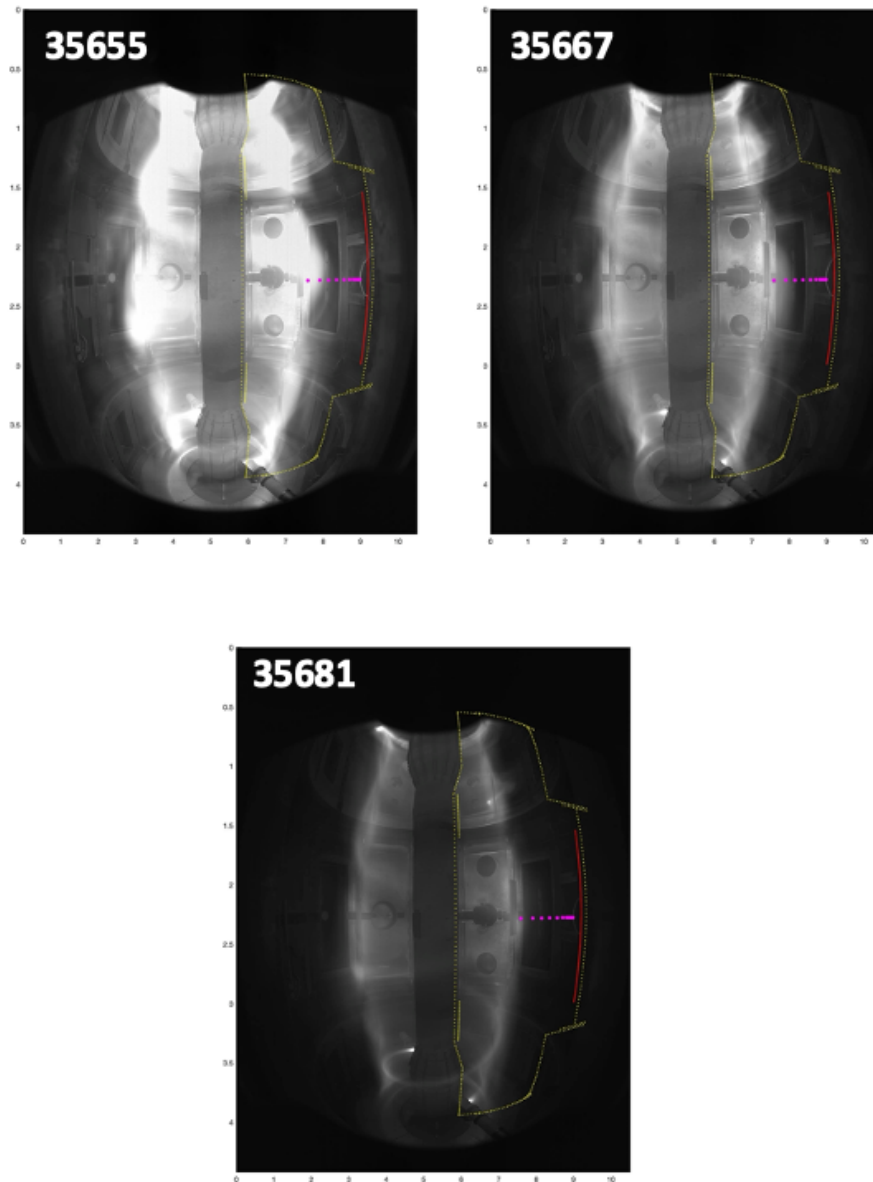


Figure 4.5 Fast camera image of discharges of figure 4.1. The exposure time of each frame is set 0.4ms. The yellow-dot-enclose-line indicate inner wall of VEST, red dot line shows the outer mid limiter.

	T_e [eV]	P [10^{-5} Torr]	λ_{mfp} [m]	ν_{en} [MHz]	$\nu_{m,en}$ [kHz]
35681	50	1.50	20.0	0.24	0.26
35667	30	3.25	6.85	0.53	0.58
35655	10	5.00	2.03	1.04	1.13

Table 1. The calculated mean-free-path, collision frequency and momentum frequency.

4.1.2. Identification of two kink modes [50]

It is described at Section 2.2 that the coherent rotating mode is accompanied by the axial current density perturbations with the same frequency of rotating[25]. This perturbation current can be measured by the Rogowski loop. Theoretically, this axial current density perturbation is induced by rotating motion[22]. Thus, this axial perturbation current related to the coherent rotating mode can be measured by the Rogowski coil in this 3D helical configuration as well as pickup coils mounted on the wall of the VEST.

As the plasma current in the flux rope increases further and far exceeds its kink stability threshold, the external kink instability is driven, resulting in the highly chaotic movements of the flux rope in the laboratory frame[27]. In this kink mode, there is no coherent rotating motion while deformation of the flux rope cross-section without periodic motion occurs. The magnetic signature of the flux rope undergoing external kink instability can be acquired by only magnetic pickup coils, but not a Rogowski coil. If the flux rope moves in the interior of the Rogowski coil loop, the Rogowski coil can measure fundamentally only the signals from the current but not from the movement itself. On the other hand, a magnetic pickup coil can measure the signal driven by both the current and movement (distance) of the rope. Therefore, through comparisons of the spectrograms of both the Rogowski and pickup coil signals, the stability of the flux rope over time, regardless of kink instability, can be confirmed.

In figure 4.6, the spectrograms for two different discharge modes regarding kink instability are shown. The discharge profile is shown at figure 3.8. Note that the current threshold, I_{KS} , for external kink instability is calculated to be ~ 220 A with the assumption of flux rope radius of 30 mm, which considers the background plasma effect that expands the radius. Figures 4.6 (a)-(c) show the discharge results that are under the external kink stability limit and the coherent frequencies of rotating kink mode. In this case, the rotating coherent frequency is observed in both the spectrogram for the pickup coil, shown in Fig. 4.6 (b), and that for the Rogowski coil, shown in Fig. 4.6 (c), over the discharge time. On the other hand, Figs. 4.6 (d)-(f) show a transition from the rotating kink mode to the external kink mode. Because internal kinks have no critical q , a smooth transition from internal kink mode to an external kink can occur[25]. While the coherent signal persists and its frequency is increased until $t=304$ ms, the broadband magnetic signature is driven on the pickup coil, whereas the Rogowski coil exhibit nothing after $t=304$ ms. Note that the Rogowski coil acquires signals from the four flux ropes at a toroidal slice of the magnetic diagnostics (MDs) array in VEST as it passes the Rogowski coil twice by two flux ropes, as depicted in Fig. 3.6. Thus, it is confirmed that the flux rope is either in the rotating kink mode or in the external kink mode.

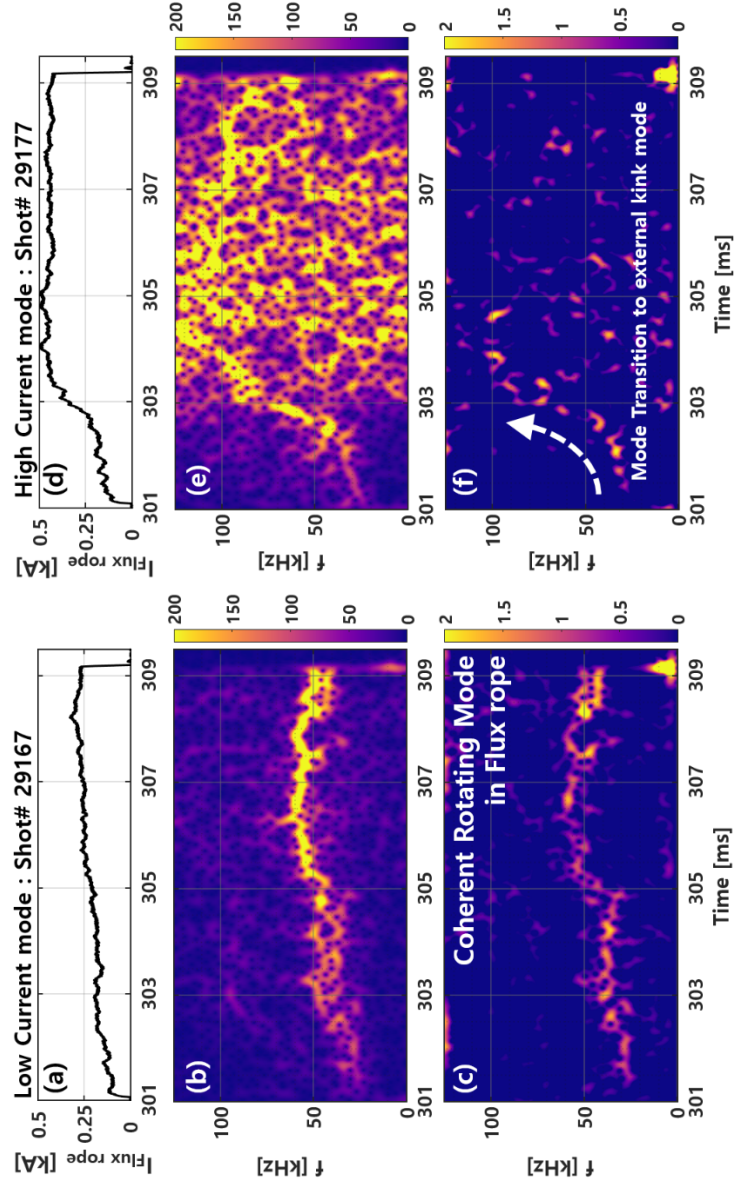
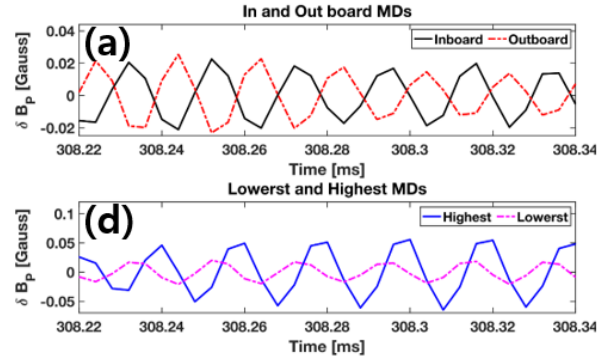


Figure 4.6 Spectrograms for two controlled discharges. (a) Flux rope current evolution for coherent rotating kink mode. (b) Spectrogram for pickup coil, I02, in coherent rotating kink mode. (c) Spectrogram for Rogowski coil in coherent rotating kink mode. (d) Flux rope current evolution for kink mode transition discharge. (e) Spectrogram for pickup coil, I02, in kink mode transition discharge. (f) Spectrogram for Rogowski coil in kink mode transition discharge. Whereas the Rogowski coil is unable to measure signals from varying locations of the flux rope, the pickup coil is able to obtain such measurements.

In order to make sure that this approach is reliable for determining kink states in 3D geometry, the magnetic perturbation signals that should be observed for both kink modes are analyzed. The magnetic field of a flux rope has a helical pattern that is determined by both the current density direction and the axial magnetic field direction in the rope[24, 51]. Because a negative current is expected to flow in the rope because of the negatively biased discharge power, kink oscillation with left-handed helicity ($B_z \parallel -J_z$) is expected. In this experiment, to analyze the oscillation of the kink instability for both low- and high-current modes, four magnetic pickup coils are selected as shown in section 3.2.1. Note that there are four rotating flux ropes at the toroidal location of the pickup coil array in VEST during this experiment; although either the inboard or outboard pickup coil array measures the signals from these ropes simultaneously, the distance between the pickup coil and each flux rope will determine the strongest signal.

Low Current Mode : Shot# 29167



High Current Mode : Shot# 29177

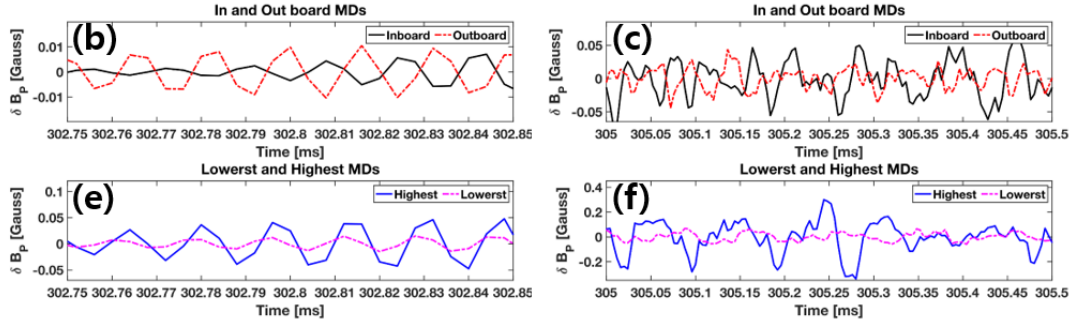


Figure 4.7 Propagation of coherent perturbation along with azimuthal (poloidal) and axial directions for two different discharges. (a)–(c) show azimuthal perturbations obtained from inside(I11) and outboard(O11) pickup coil set, and (d)–(f) show those in axial direction

Figure 4.7 shows the propagation of perturbation along the azimuthal and axial directions about the flux rope for both discharges. For the low-current mode, Fig. 4.7 (a) shows the temporal evolution of δB_θ oscillation measured by both an inboard pickup coil, I11, and an outboard pickup coil, O11, at a similar vertical (Z) location. This measurement shows the temporal evolution of the 180° phase difference, which is sufficient to confirm the rotating signal but not the helicity direction. In this experimental setup, another pickup coil at a different poloidal location is not possible; thus, the helicity direction of the flux rope cannot be determined. In Fig. 4.7 (d), the phase difference between the lowest inboard pickup coil, I25, and the highest inboard pickup coil, I02, shows that the mode propagates along the flux rope, indicating measurement at two different axial positions. The lowest, I25, is measured in the vicinity of the arc plasma source, whereas the highest inboard pickup coil, I02, measured the signal at the other end region. For the low-current mode, the magnitude of the signal increased as the mode propagated along the flux rope, as suggested by the phenomenological mode[22]. Additionally, K_z was in the direction from the arc plasma gun to the upper plate of VEST. On the other hand, for the high-current mode, the temporal evolution and axial phase difference are shown in Figs. 4.7 (b)–(c) and 4.7(e)–(f), respectively. In this mode, there was a kink mode transition, as described earlier in this section. As shown in both Figs. 4.7 (b) and 4.7 (e), before the transition, a coherent rotating signal is measured at both the magnetic pickup coil and Rogowski coil. Note that the temporal evolution shown in fig. 4.7 (b) and the axial phase difference shown in Fig. 4.7 (e) are similar to those for the low-current mode, which are shown in Figs. 4.7 (a) and 4.7(d), respectively. After the transition, the external kink is dominant, whereas a chaotic signal is observed at both the temporal evolution and the axial phase difference, which cannot be used to obtain any meaningful information. During the external kink mode, both perturbations exhibited chaotic results, which indicates that the data are neither repeatable nor predictable. This chaotic behavior

of external kink instability of the flux rope has also been observed in another device[26]. Therefore, the magnetic perturbation that should exist for kink modes is clearly measured, which means the approach proposed here is reliable.

4.1.3. Coupling to kink theory

One of the important conditions for a magnetic flux rope is its boundary condition because such a condition can influence the stability limit of kink instability and other characteristics, such as the rotating frequency[22]. In this study, it has been inferred that the magnetic flux rope is characterized by the boundary condition “line-tied at both ends,” based on three reasons: (1) one end of the flux rope is essentially tied to the arc plasma gun, (2) the incident angle between the other end of magnetic flux rope and the anode is $\sim 15^\circ$, and (3) the degree of insulation, κ , is ~ 0.8 . Sun et al.[23] showed that the incident angle between a flux rope and an anode can determine the boundary condition at the anode side and that an angle lower than 22.5° has the line-tied properties of kink instability. The 3D vacuum-field-following-calculation results exhibit good agreement with the experimental observation, as depicted in Fig. 3.18a. Based on this calculation, the incident angle is determined to be $\sim 15^\circ$. Furthermore, the phenomenological kink theory described by Ryutov et al. (2006) suggested the use of the degree of insulation, κ , which indicates whether the plasma can be insulated from the conducting boundary by finite sheath resistance. The value of κ can be calculated as the ratio of the Alfvén transit time and inductive decay time at the sheath[22]. In our case, the degree of insulation is calculated to be ~ 0.8 (based on typical plasma parameters of flux ropes in VEST and the following assumptions: $a = 2$ cm, $T_e \approx 10$ eV, $n_e \approx 10^{19} \text{ m}^{-3}$, $\frac{c_s}{v_z} \sim 1$, $B \sim 350$ G), which indicate that the magnetic flux rope was not insulated from the upper plate of VEST. Therefore, the magnetic flux ropes in this study have a line-tied condition at both ends. The ideal current threshold for kink instability in a line-tied condition at both ends, $I_{KS} = \frac{(2\pi)^2 a^2 B_{axial}}{\mu_0 L}$, is calculated to be ~ 22 A, given a throughput radius of 10 mm for the arc plasma gun. Note that if flux ropes are in only line-tied condition at one end, the ideal current threshold will be halved to ~ 11 A.

As a part of further verification of the proposed approach, the analysis based on the kink theory is conducted. To couple the phenomenological kink model suggested by Ryutov with the experimental results of this study, a number of conditions must be devised and fulfilled. First, as described in previous section, the magnetic flux rope in this study is characterized by line-tied boundary conditions at both ends. Second, the 3D helical configuration of the magnetic flux rope in VEST can be assumed to be a linear configuration for the theoretical approach. Third, the length, L , of the flux rope is calculated to be ~ 5 m based on the vacuum-field-following-calculation results. Although the radius, a , of the cross-section of the flux rope could not be measured for this 3D configuration, the radius a is expected to be far less than $L = 5$ m, as shown in the fast-camera image in Fig. 3.4. The expected I_{KS} limit in this study was ~ 220 A, which is calculated based on $a = 30$ mm. Therefore, the long-and-thin assumption, $a \ll L$, is satisfied for the magnetic flux rope in VEST.

The frequency of the current-driven rotating-kink mode, accounting for the effects of both the axial flow and line-tied condition, is

$$f_{kink} = -\frac{\pi v}{L} \frac{I_{flux\ rope}}{I_{KS}} = -\frac{\pi M v_{alfvén}}{L} \frac{I_{flux\ rope}}{I_{KS}} \quad (4.1)$$

where v is the axial flow speed, L is the length of the flux rope, M is the Alfvén Mach number ($\equiv \frac{v}{v_{alfvén}}$), $v_{alfvén}$ is the Alfvén velocity, and I_{KS} is the Kruskal–Shafranov limit. This rotating mode is azimuthal in the $m = 1$ mode. In addition, the kink-mode structure can be calculated using the phenomenological model. The perturbed axis of the flux rope, the center of every cross-section of the flux rope, rotates around its axis and is derived using the equation by Ryutov et al.[22] [Eq. (65) and Eq. (67) of Ref.[22].], which has been reorganized for this study as

$$r_{kink} = \exp\left(\frac{z}{L} \frac{M\pi}{\sqrt{1-M^2}} \sqrt{\frac{I^2}{I_{KS}^2} - (1-M^2)}\right) * \sin\left(\pi \frac{z}{L}\right) \quad (4.2)$$

where z denotes the axial position along the flux rope, L is the length of the flux rope, M is the Alfvén Mach number, and I_{KS} is the Kruskal–Shafranov limit.

To calculate the kink mode using Eqs. (4.1) and (4.2), two unknown parameters are obtained. In this study, the Alfvén Mach number is used as a free parameter for the coupling of the kink theory and the experiments and it is set to 0.4, which has been used on another arc plasma gun-based device[21, 24]. The remaining unknown parameter is the Alfvén velocity, v_{alfven} , which is characterized by an inverse square-root dependence on ion density, $v_{alfven} = \frac{B_0}{\sqrt{\mu_0 m_i n_i}}$, where B_0 is the magnetic field strength, μ_0 is the vacuum permeability, m_i is the mass of the ion, and n_i is the ion density in the flux rope. To obtain v_{alfven} rigorously, the ion density, n_i , must be obtained. To obtain the ion density in the flux rope, the impedance model of the arc plasma gun is used in conjunction with the monoenergetic beam assumption[18, 19].

The calculation results for the rotating frequency based on Eq. (4.1) and the other assumptions described in the previous section are shown in Fig. 4.8. For the low-current mode, in which the coherent rotating kink mode is maintained over time, the calculated coherent frequency agreed well with the experimental results, as shown in Fig. 4.8(a). The Alfvén Mach number, M , used here as a free parameter, is set to 0.4 during the discharge time for the calculation. On the other hand, for the transition to the external kink mode, the high-current mode, M , is a time-variant that is increased from 0.4 to 0.7 during discharge time. This is consistent with the change in impedance (current) attained through increases in the gas injection during the discharge through the solenoid valve open-time control, which increases the axial flow, thereby increasing the M number. Before $t=304$ ms, a coherent rotating signal appears in the spectrogram, and the calculated frequency is in good agreement with the experimental results. When the flux rope current is increased further, the broadband signal appears on the spectrogram, and the calculated frequency is

no longer matched. When the current far exceeds the kink threshold, the phenomenological kink theory cannot explain the behavior of the kink mode because it is in a non-linear regime. However, the phenomenological theory may provide a hint regarding this non-linear regime. For example, the strongest signal of the spectrogram appears in the vicinity of the calculated frequency, as shown in Fig. 4.8(b). Thus, the approach for the rotating kink mode frequency calculation is quite successful for the flux ropes in VEST, indicating that the determination of the 3D kink modes based on our approach is reliable.

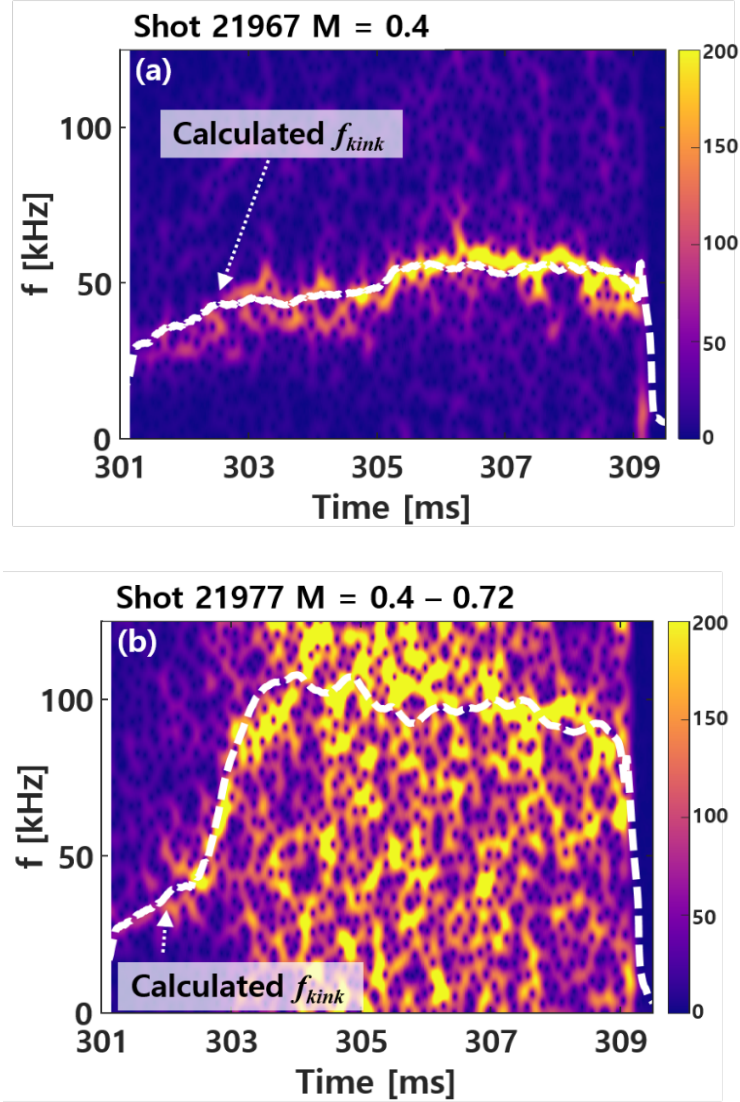


Figure 4.8 Spectrograms for two controlled discharges and calculated frequency of kink mode. (a) Low-current mode subject to coherent rotating kink mode, (b) High-current mode transitioned to external kink mode from coherent rotating kink mode. The two spectrograms in this figure are the same as those depicted in figs. 8(b) and (e). Because these discharges are controlled by gas injection, different Alfvén Mach numbers, M , are used for the calculation. Kink frequency during transition is precisely calculated for the given M number range. Flux rope current evolutions for each discharge are given in figs. 7 (a) and (b) respectively. ($a = 30$ mm, $L = 5$ m, Baxial = 350 G)

It is reported that the rotating frequency is determined by either the Doppler shift by the axial flow or the $E \times B$ force on the flux rope[21, 22, 26, 27, 52-54]. In our case, it is expected that the axial flow in the flux rope is the main contributor to the coherent rotating frequency, as in many other arc plasma gun-based experiments[21, 24, 54]. Note that the arc plasma gun-based experiment resulted in a natural flow because of the pressure difference between the interior of the gun and the vessel chamber. Furthermore, the gas injection also affects the axial flow during the discharge.

The coherent rotating kink frequency, f_{kink} , and its structure, r_{kink} , can be calculated using Eqs. (4.1) and (4.2). Furthermore, the synthetic magnetic signature of the current-driven rotating-kink mode can be calculated. To obtain the synthetic signal of the magnetic signature, a rotating flux rope model is developed based on the principles of electromagnetism, as shown in Fig. 4.9. Although the development of similar simple models and their corresponding calculations were attempted in previous studies[18, 21, 53], the big difference in this study is the use of the calculation results of two combined models: (1) a phenomenological model and (2) a coherent beam with monoenergetic drift velocity. The model used in this study begins with the vacuum-field-following-calculation, as indicated by the yellow dotted line in Fig. 3.5. Based on the calculation, the center locations (R , Z) of the rotating flux rope are obtained. In this case, four center locations are obtained at the toroidal location of the inboard pickup coil array. When the $m=1$ coherent rotating kink mode occurs, it rotates around the center (R , Z). The rotating frequency, f_{kink} , is used in the calculated results from the previous section. On the other hand, r_{kink} is obtained from the calculated results from Eq. (4.2). When there is rotating plasma with f_{kink}, r_{kink} at (R , Z), the theoretical synthetic magnetic signal at each pickup coil location (r_p , z_p) can be calculated. Through the use of electromagnetism principles, the B_θ of the synthetic magnetic signal at (r_p , z_p) is derived as follows:

$$B_{\theta} = -\frac{\mu_0}{2\pi} (I_{flux\ rope} * \frac{\delta r}{(\delta r^2 + \delta z^2)}) \quad (4.3)$$

where μ_0 is the vacuum permeability, $I_{flux\ rope}$ is the flux rope current, and $\delta r = r_p - R - r_0 \cos(2\pi f_{kink} t)$, $\delta z = z_p - Z - r_0 \sin(2\pi f_{kink} t)$ are the radial and vertical differences between the pickup coil and perturbed flux rope center, respectively. When eq. (4.3) is differentiated with respect to time t , the synthetic magnetic signal can also be derived as

$$\dot{B}_{\theta} = \frac{\mu_0}{2\pi} \left(I_{flux\ rope} \frac{r_{kink} 2\pi f_{kink} \sin\left(2\pi f_{kink} t - 2 \tan^{-1}\left(\frac{\delta z}{\delta r}\right)\right)}{(\delta r^2 + \delta z^2)} \right) \quad (4.4)$$

Through the use of Eq. (4.4) and based on four flux ropes at the toroidal location in VEST, the calculations of the rotating model are obtained as shown in Fig. 4.10 with 300 μs time window. Five inboard magnetic pickup coils are selected based on the four flux-rope locations. The cross-correlations are also depicted in Fig. 4.10. Most of the rotating model calculations are in good agreement with the experimental results. Excluding that for the lowest pickup coil, the average cross-correlation value is 0.82. On the other hand, the cross-correlation value for the lowest pickup coil is 0.5, which is quite low compared with those for the other pickup coils. This discrepancy is due to the large phase difference at $t = [307.25\ 307.35]$.

For the low-current mode, i.e., “gentle” wiggling and $m=1$ rotating kink mode, the phenomenological theory and coherent beam assumption are valid. However, for the transition to high-current mode, which is the external kink mode, the broadband magnetic signature and non-linearity occur, and thus the model becomes irrelevant. Nonetheless, combining the theoretical model and coherent beam behavior is quite successful and explains the dynamics well for the $m=1$ rotating kink mode of flux ropes in VEST. Through this calculation, it is confirmed that the coherent rotating kink mode classified by the proposed approach is consistent with its theoretical approach.

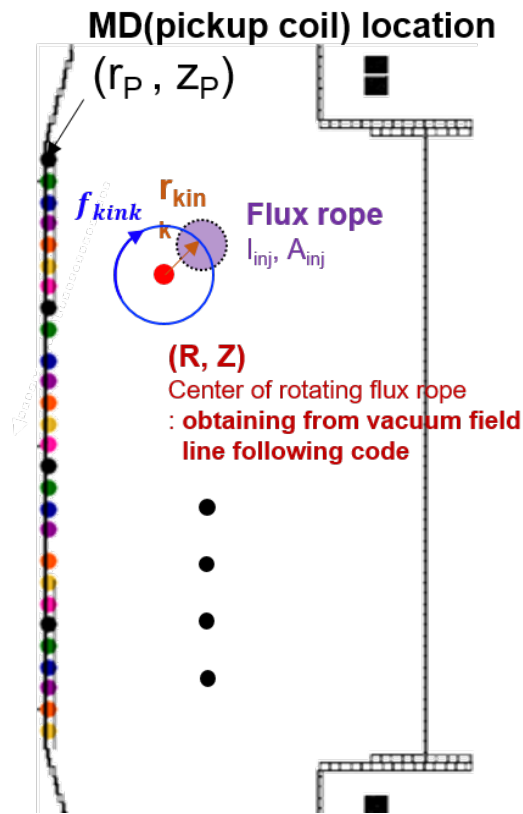


Figure 4.9 Toroidal cross-sectional view for rotating kink mode. The red dot indicates the center of rotating flux rope, as calculated based on vacuum-field-following-calculation code. Values of f_{kink} and r_{kink} are calculated from Eqs. (4.1) and (4.2), respectively. Through the use of simple electromagnetism, a magnetic signature from rotating flux rope can be calculated, as derived using Eqs. (4.3) and (4.4).

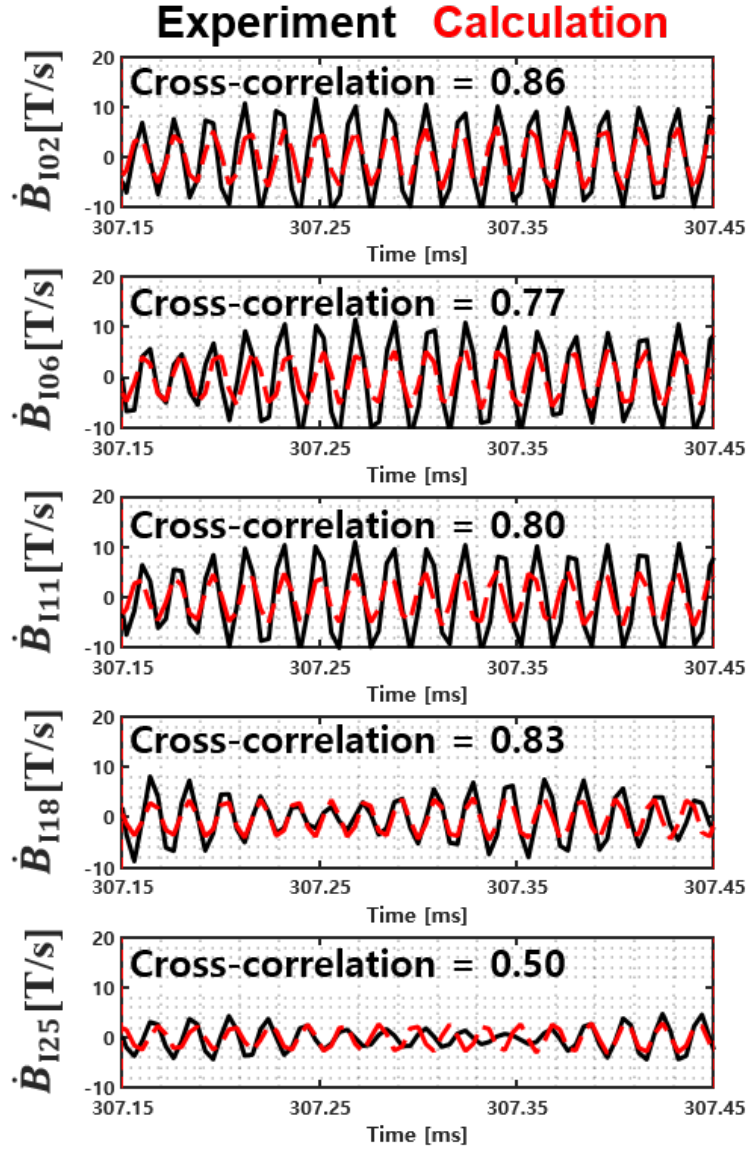


Figure 4.10 Magnetic signatures for coherent rotating kink mode. Black lines indicate experimental results obtained using inboard magnetic pickup coil array, whereas red lines indicate calculations obtained by using the rotating model, as shown in Fig. 4.9 and based on eq. (4.4).

4.2. Conditions for merging

So far, the kink instability in 3D flux ropes, considered the most potent triggering force for merging, is observed and diagnosed effectively without invasive measurement. As merging activity is expected by the external kink mode in flux ropes, the CIII ion temperature is measured in this merging experiment to evaluate merging activity. These experiments will be referred to as the rope-rope merging experiments, and Figure 4.11 show the rope-rope merging experiment configuration.

Since lowering vacuum field strength (axial field) results in highly dynamical and moving flux ropes in the chamber, selecting the IDS channel is also important. It is also expected that the velocity distribution would be different according to the direction; perpendicular or parallel to the magnetic field. However, the highly dynamical state of flux rope makes it hard to choose the channel of IDS considering the direction. As the exposure time of IDS is 1 ms, which is quite long compare to merging process, the measured ion temperature would be thermalized-mean-representative value. The Doppler tomographic inversion technique is used to measure the radial ion temperature profile in this experiment. The highest ion temperature is selected for a given shot. Typically, in this experiment, the high emissivity location of inversion is where the ion temperature is high.

Local magnetic reconnection experiment with 3D magnetic field and flux ropes

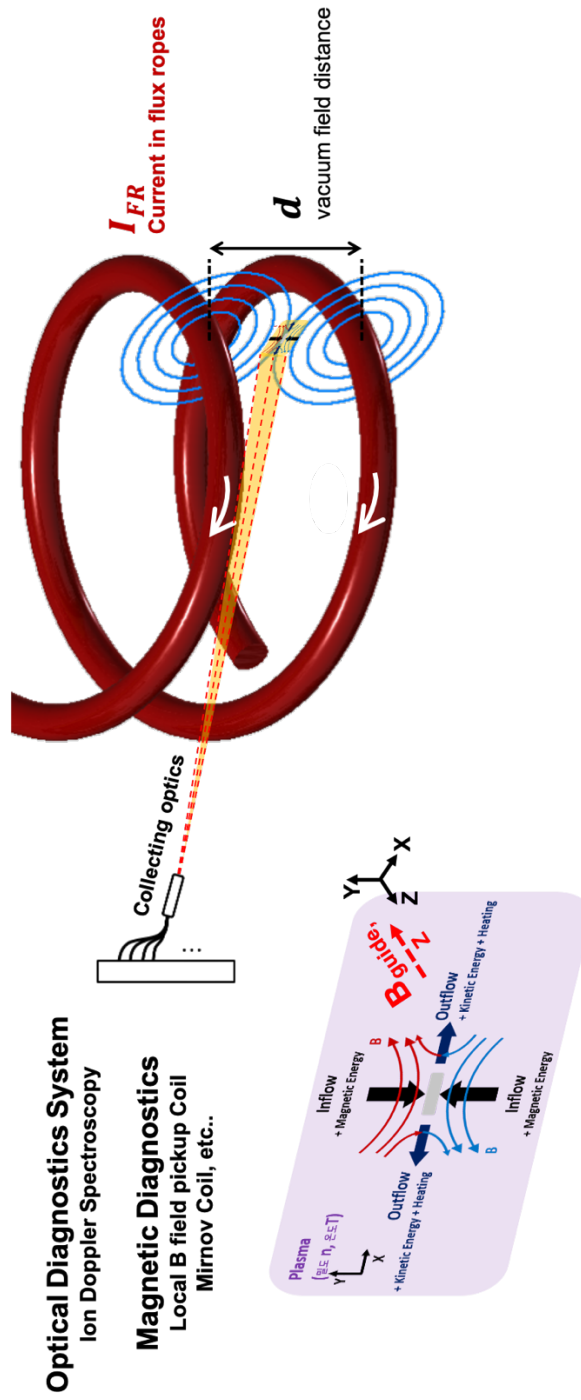


Figure 4.11 Rope-rope merging experiment configuration.

4.2.1. Dependence of merging on the guide field

In section 2.3, the parameter that can estimate the in-plane reconnection electric field using discharge parameters based on 2D reconnection theory is introduced[15]. This parameter of $I_{inj}\sqrt{V_{inj}}$ will be used for indicating the control knob for experiments. In addition, increasing injection power is accompanied with increased neutral pressure for high current discharge. The wall interaction with flux rope can result in impurities from the wall as the discharge current is increased.

Figure 4.12 show the $I_{inj}\sqrt{V_{inj}}$ scan(x -axis) results from the rope-rope merging experiment with reduced axial field strength compare to section 4.1.1(Figure 4.2). To clearly show the difference according to axial field strength, the same data in figure 4.2 is also depicted with a black cross in figure 4.12. The most noticeable difference is the linear tendency in both ion temperature and toroidal velocities with discharge parameter, which imply the merging process via magnetic reconnection. Figure 4.13 show the spectra of selected shot points colored in green, blue and black in figure 4.13. Figure 4.14 show the discharge details of three selected shots in rope-rope merging scan. The OV/OII ratio measured by filter scope shows similar evolution, but for shot 35885, the lowest injection power colored in blue, show a slightly higher ratio value. Note that in figure 4.12 (a), the poloidal field calculation results for black line show $|B|$ ratio higher than 1, which means it can be kink stable condition. However, in this calculation, the flux rope's radius, a , is set as a free parameter of 0.03 [m]. To check its kink stability, as suggested in section 4.1.2, spectrograms of the magnetic pickup coil and Rogowski coil are checked. Figure 4.15 show the spectrograms of three shots (#35885, #35871, #35862). The spectrograms of the magnetic pick-up coil clearly show the chaotic signal due to external kink mode in flux rope, while spectrograms of the Rogowski coil show a very quiet signal. Note that, the external kink mode in flux rope cannot leave any magnetic signal on the Rogowski coil. The fast camera images for each three selected shots are shown in figure 4.16.

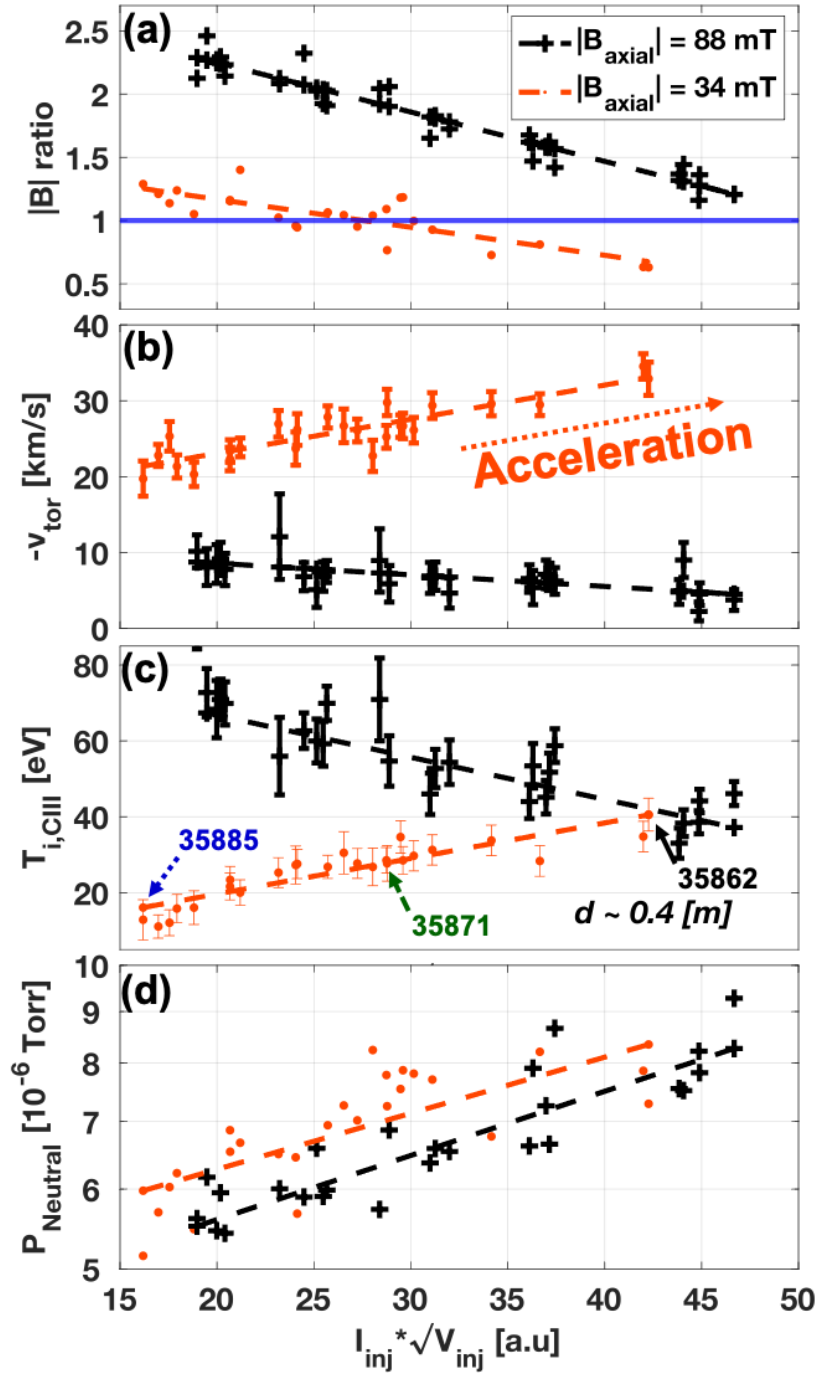


Figure 4.12 The injection power scan with reduced axial field strength

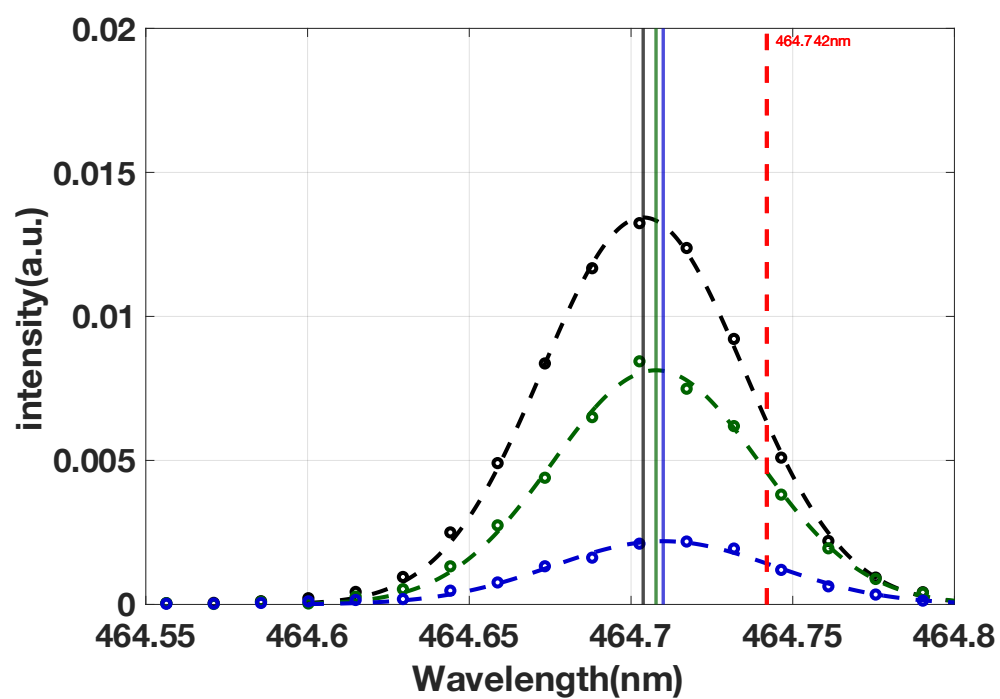


Figure 4.13 Example spectra corresponding three selected data in figure 4.13

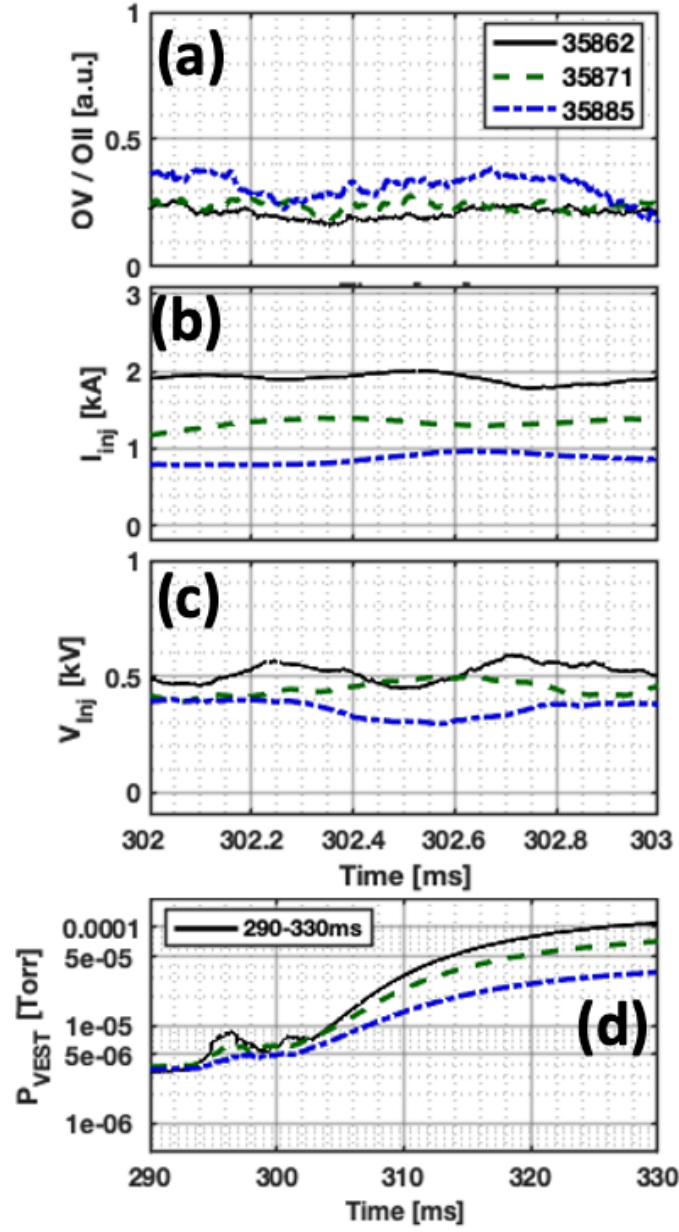


Figure 4.14 Three selected discharge result for low field strength scan. (a) line-integrated OV/OII ratio measured by filter scope. (b) total flux rope current. (c) discharge voltage. (d) neutral pressure time evolution.

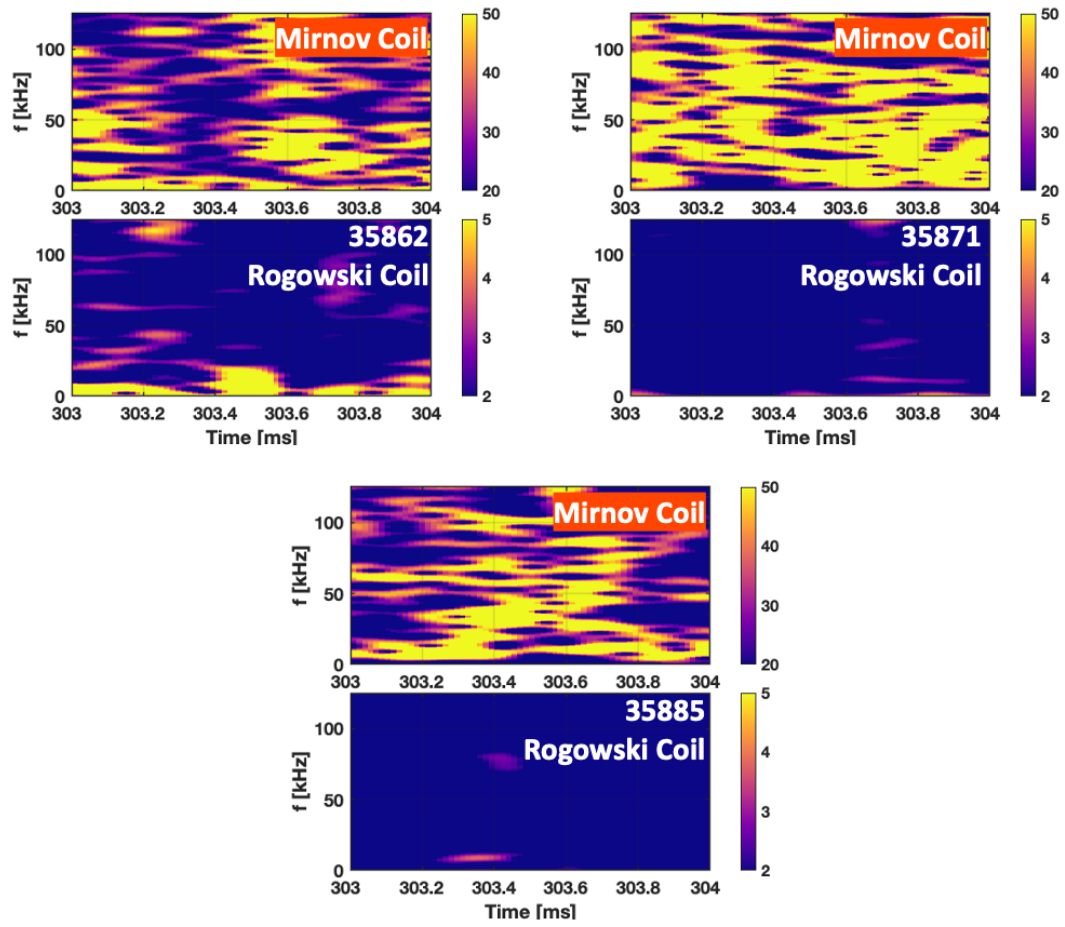


Figure 4.15 The spectrogram from inboard magnetic pickup coil(up) and the Rogowski coil(down) in VEST. The chaotic signal on magnetic pickup coil means flux ropes undergoes external kink mode.

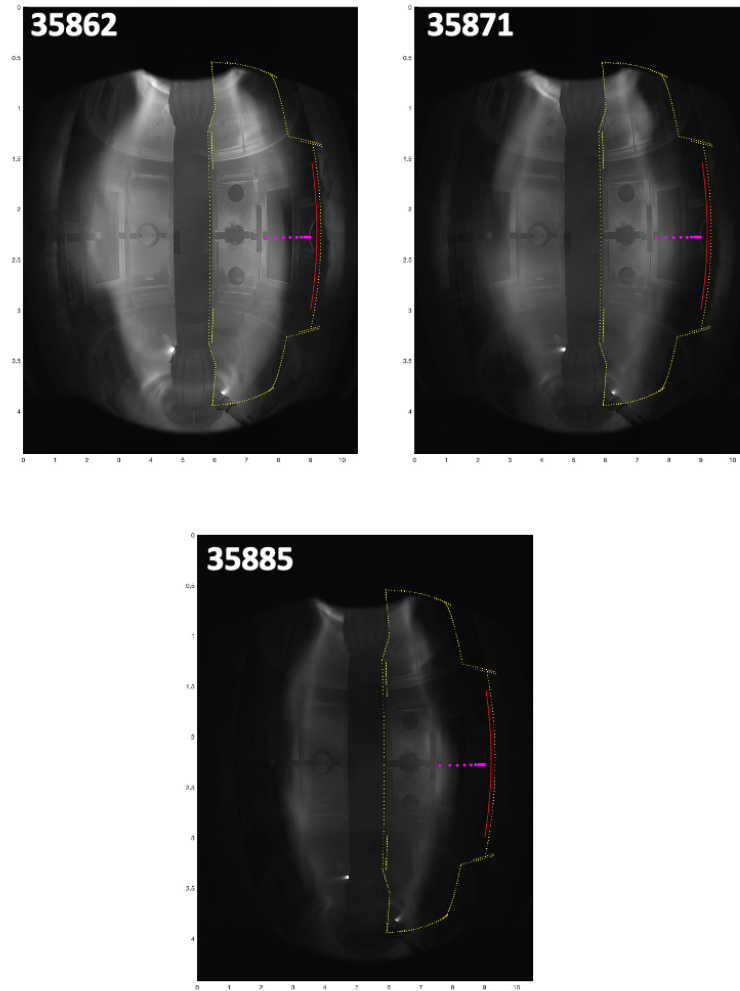


Figure 4.16 Fast camera image of discharges of figure 4.13. The exposure time of each frame is set 0.4ms. The yellow-dot-enclose-line indicate inner wall of VEST, red dot line shows the outer mid limiter.

From all these results (Fig 4.12-16), the important results can be concluded as following. With high guide field strength (black lines in Fig 4.12), the flux ropes show the glow discharge like tendency; the neutral pressure determine T_i, T_e . Thus, increased neutral pressure has result in decreased T_i with relatively steady v_{tor} . However, relatively high confinement tendency may observable in this scan results, which result in high bulk ion temperature. On the other hand, with the low guide field strength (orange lines in Fig 4.12), show external kink mode confirmed by the spectrograms. However, increasing T_i with increasing v_{tor} is observed, meaning external kink has forced flux ropes to merge. In addition, relatively low confinement tendency may observable in this scan results, resulting in low bulk ion temperature. Note that, the evaluation of guide field strength is determined relatively by the current in flux rope and its radius.

4.2.2. Dependence of merging on the field pitch

Unlike the 2D reconnection environment, the rope-rope merging experiment is conducted with a guide field (toroidal field). It is well known that the effect of the guide field[15, 55], which is in a linear relationship between its strength and ion temperature. However, it is also known for flux ropes merging that the guide field act as impeding force for merging[35, 36]. Here, the difference is due to its occurrence. When there is no triggering force for merging (pushing ropes or attracting each other), the guide field can impede the merging. On the other hand, when flux ropes are forced to be merged by other external forces, then the guide field can act to confine the high-temperature ions, so give linear relation. In addition, not only its impeding(repulsion) force for merging but also its role in the kink stabilize effect are expected. Moreover, in 3D merging reconnection theory, this guide field can reduce B_{rec} strength[56, 57].

Figure 4.17 show the simple calculation results regarding the effect of the guide field on B_{rec} strength. In ST configuration, the reconnection angle can be calculated[56, 57], and for VEST configuration it can be equated as

$$\cos \theta = \frac{B_{rope,upper} \cdot B_{rope,lower}}{|B_{rope,upper}| |B_{rope,lower}|} = \frac{(\frac{24 * I_{TF}}{R_{major}})^2 - (\frac{I_{flux rope}}{d})^2}{(\frac{24 * I_{TF}}{R_{major}})^2 + (\frac{I_{flux rope}}{d})^2} \quad (4.5)$$

Here, I_{TF} is current in toroidal field coil, R_{major} is major radius location of flux ropes, $I_{flux rope}$ is current in flux rope and d is the distance between flux ropes. As expected, the more they closer, the more reconnection field strength can be achieved. The toroidal field strength is set as 34 mT at $R = 0.4$ m for comparing with experimental results that will be shown in the following sections. Note that these calculation results are only valid with flux ropes in MHD stable state as the calculation does not include any MHD phenomena such as kink and attraction force. Nevertheless, reducing the distance between flux ropes can help with high unstable flux ropes, and these are shown in Fig 4.18.

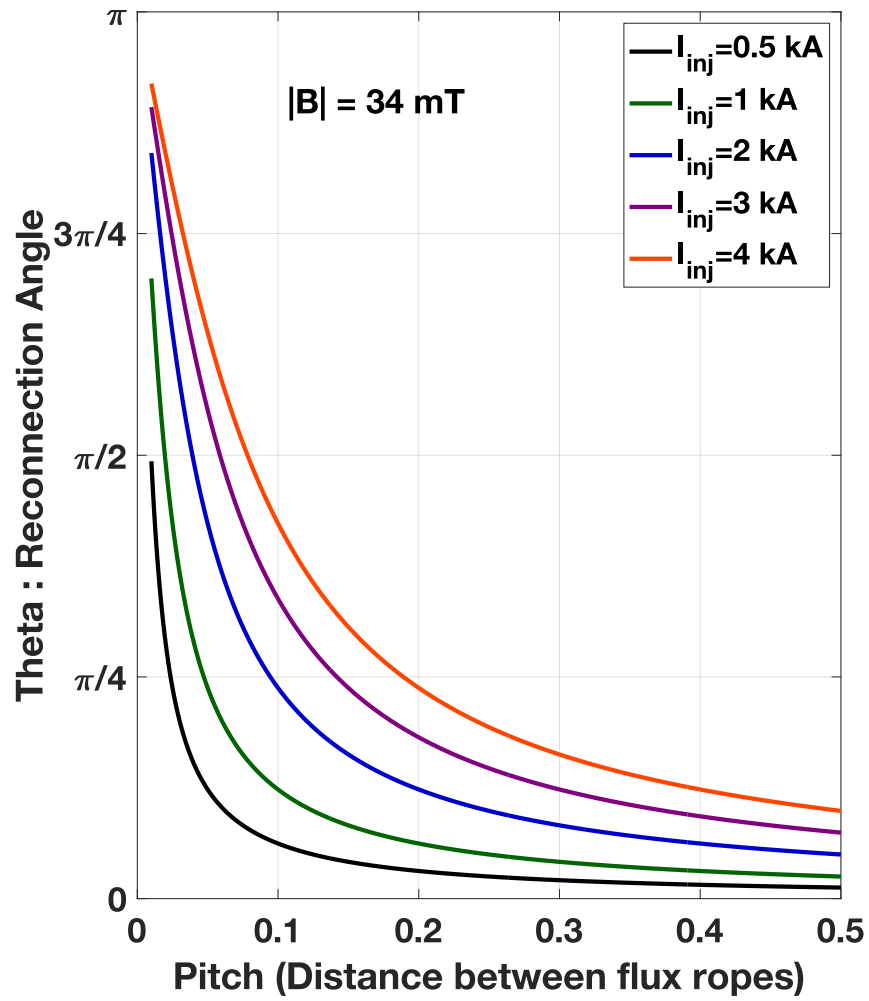


Figure 4.17 The effect of guide field on reconnection field strength

In figure 4.17, the reconnection field strength during merging can be increased as the distance between ropes is decreased. Also, it means that the kink instability is not the only condition for 3D rope-rope merging.

To check the rope-rope merging dependency on the distance between flux ropes, d , the 3D helical magnetic field configuration in VEST is adjusted by slightly increasing PF coil current while the toroidal field remains unchanged. The d can be seen in Fig 4.11. As a result, the four different distance, 0.34 m, 0.38 m, 0.41 m, and 0.44 m, was made for the experiments. The results are shown in figure 4.18. The overall results and their tendency are consistent with the calculation results in figure 4.17.

Note that this distance means the distance set by the vacuum magnetic field. The actual distance can be much reduced as the flux ropes are undergoing highly unstable external kink mode. To check the stability of flux ropes, the spectrograms of data at both ends on the axis for each flux rope current are depicted in figure 4.19. Interestingly, during the merging process, the magnetic signal on the Mirnov coil is reduced while the spectrograms of the Rogowski coil are relatively low signals, which means the flux ropes are in the external kink unstable state.

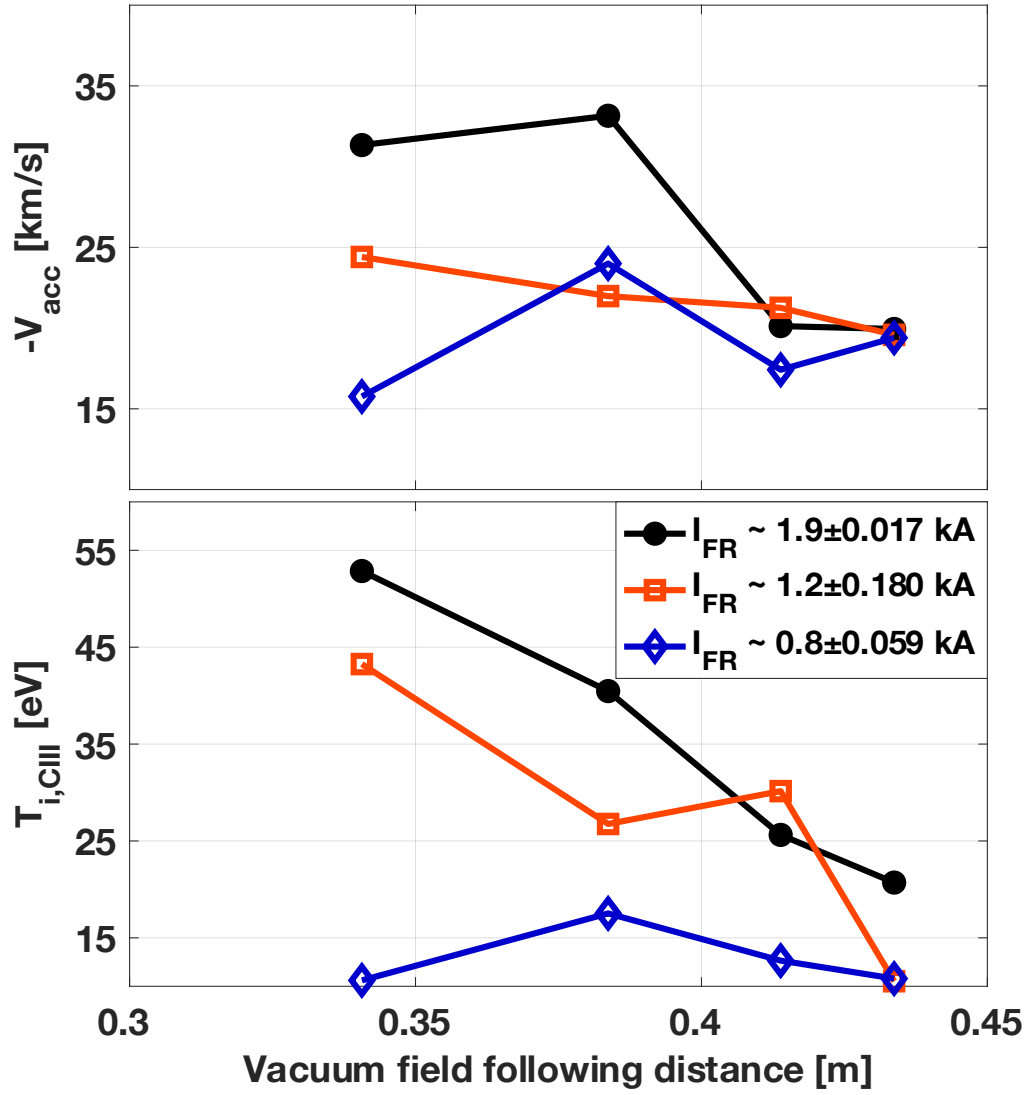


Figure 4.18 The merging dependency on the distance between flux ropes

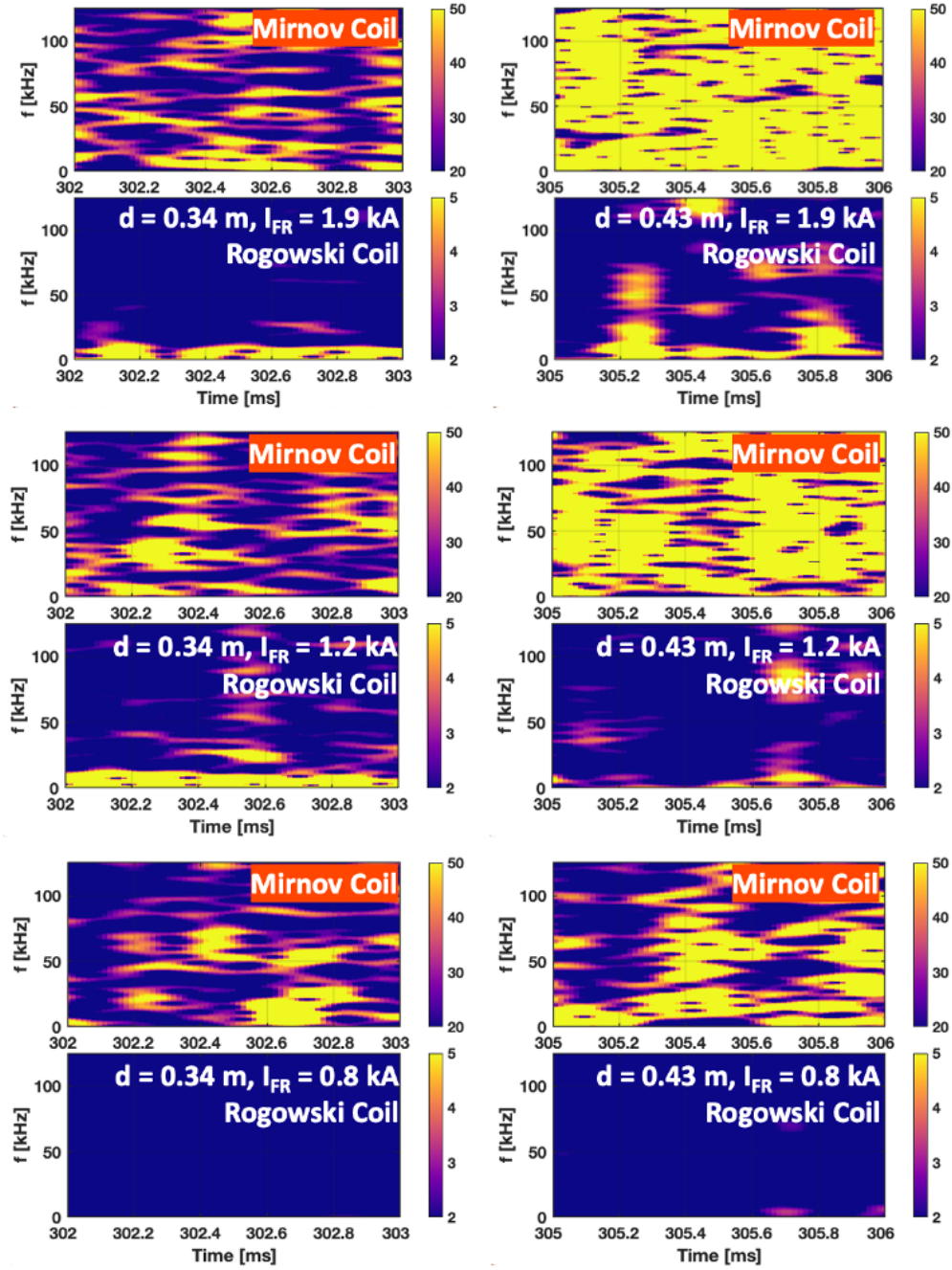


Figure 4.19 The spectrograms of two end points for each flux rope current in figure 4.16.

4.2.3. Impedance changes of flux rope during merging

One intuitive picture during rope-rope merging is the broken and shorten length of the flux rope. This process is also suggested NIMROD simulation [13, 14]. These activities should be observable by other data that related to flux rope discharge; namely, the impedance of flux ropes, Z . In this impedance, there are two main components that describe flux rope length; impedance and resistance. The relation between parameters can be expressed effectively as follows.

$$\frac{V_{FR}}{I_{FR}} = Z_{FR} = L_{FR} \frac{dI_{FR}}{dt} \frac{1}{I_{FR}} + R_{FR} \quad (4.6)$$

During the experiment, all the current in flux rope and voltage that sustain flux rope is acquired by an oscilloscope with 5MHz sampling as shown in Section 3.3.3.

In figure 4.20, the changes of impedance during rope-rope merging at early discharge time are depicted. Two shots are selected and depicted in Fig 4.20 (a). The black line (Shot#35964) indicates the successful rope-rope merging case, while the green line (Shot#35967) indicates the case barely processed rope-rope merging. When rope-rope merging happens, so at least one toroidal ring may be achievable, the impedance is decreased in half, as shown in figure 4.20 (c) and (d) with a colored line with a right Y -axis. During time duration $1[t=301.1, 301.4]$, the impedance of 0.8 is measured. The global twisting(deformation) of a flux rope can introduce extra impedance for flux ropes with some n -turn. After $t=301.5$, the impedance of flux rope decreased up to 0.4. Rope-rope merging has decreased the turn number by at least 1 (So, $n-1$ turn). Thus, decreased helical turn may result in reduction on both L_{FR} and R_{FR} , so Z_{FR} . Interestingly, the mid-localized field amplification is observed at this time, as shown in Fig 4.20 (e). On the other hand, when rope-rope merging does not proceed for some reason (not shown here), these tendencies are not observed as shown in Fig 4.20 (d) and (f).

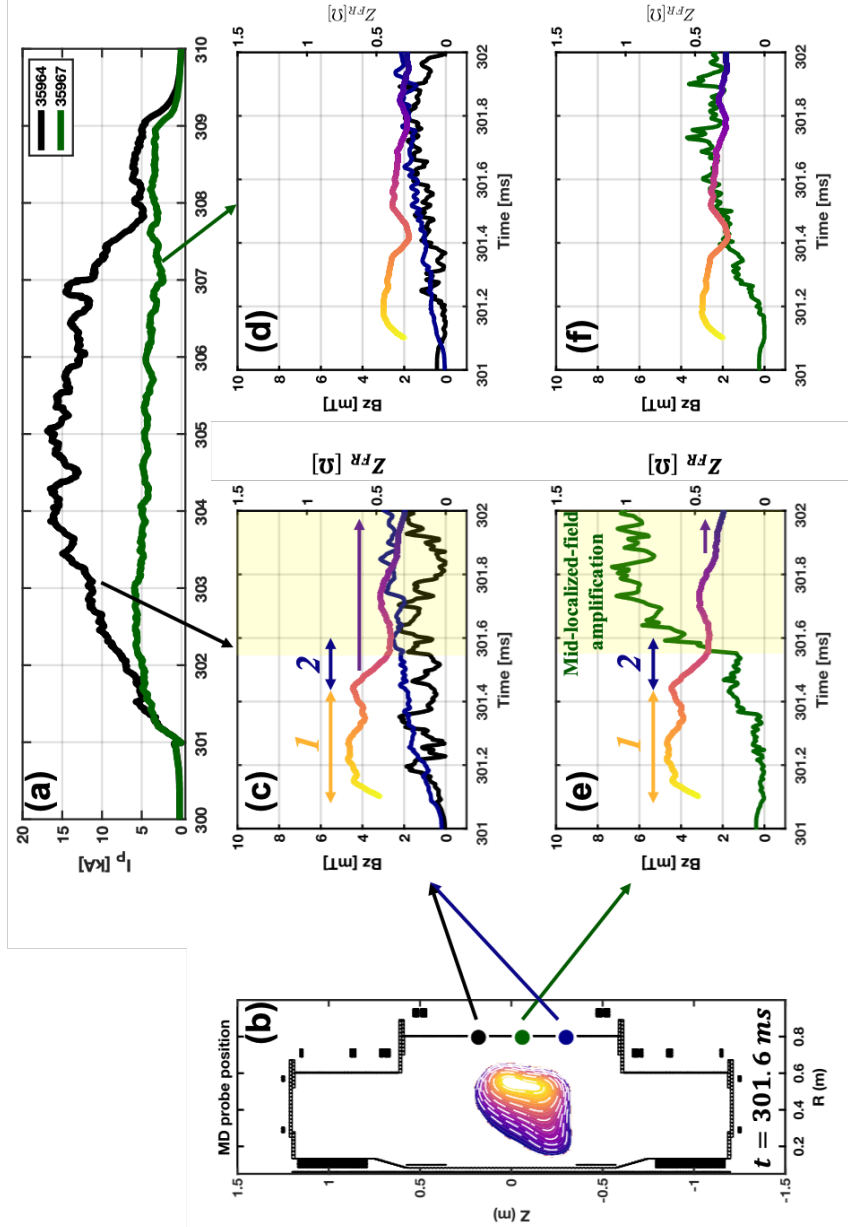


Figure 4.20 Impedance changes during rope-rope merging and localized B-field amplification. (a) Discharge profile during rope-rope merging, (b) Cross-section and selected Mirnov coils, (c and d) B_z signals at two vertical ends (black and blue in (b)) for two shots in (a) and (e and f) B_z signals at $Z=0$ [m] (green in (b)) for two shots in (a)

4.3. Discussion

In this chapter, extensive research regarding kink instability in flux ropes and their merging between two kink-unstable flux ropes is conducted. Interestingly, the flux ropes in 3D configuration have shown the characteristics observed in a linear configuration, which are from the MHD stable to highly unstable kink mode. The behavior of flux ropes is well explained by both phenomenological theory and monoenergetic assumption. Moreover, the merging between flux ropes triggered by highly unstable external kink instability is observed. Without an external kink state, no merging is triggered.

So far, the operational condition for merging in 3D flux ropes is the strength of the guide field. The guide/toroidal field acts as not only a repulsion force between two ropes but also as the kink stabilizing control knob. Thus, the guide/toroidal field must be limited up to the level comparable with the poloidal field driven by flux ropes. For the operation of ST or tokamak, the toroidal field (guide field for rope-rope merging experiments) is required to be as high as possible for the safety of tokamak plasma. However, its high value can result in operation failure for LHI from the start as the rope-rope merging process cannot proceed. In order to operate LHI successfully in high toroidal field strength, a high current of the LHI system is required.

Finally, for the successful rope-rope merging in 3D helical configuration, the condition $|B_{pol,flux\ rope}| \ll |B_{tor,axial}|$ is important; condition #1.

Chapter 5. Demonstration of local helicity injection

As indicated in section 1.5, the practical usage of magnetic flux ropes in VEST is the realization of a non-inductive current drive via the LHI technique. In this chapter, additional conditions for both driving plasma current non-inductively and reaching the Taylor relaxation will be introduced in Sec 5.1. In addition, non-inductively driven tokamak-like plasma results and its characteristics such as edge-localized ion heating and MHD characteristics will be addressed in Sec 5.2.

5.1. Conditions for the transition to HI phase

5.1.1. The effect of proximity

In this chapter, the sustained current drive with LHI will be addressed. It is obvious that without helicity injection or Taylor relaxation, the tokamak-like plasma cannot be maintained in LHI experiments. To inject magnetic helicity via the Taylor relaxation process, the close proximity between plasma in a closed flux surface and flux ropes is required. This close proximity will be referred to as “coupling” or just simply “proximity”.

It is easy to think that the high proximity easily can be maintained during LHI as two high current plasma flowing in the same direction co-existed. However, during the LHI technique, maintaining the high proximity condition is difficult. For context, here is a brief explanation. The magnetic field in VEST has two components; a toroidal field driven by TF coil and a poloidal field driven by PF coil. For tokamak and ST plasma, the main role of the poloidal field driven by the outer PF coil is to provide radial force balance. It is well known that tokamak(-like) plasma undergoes a naturally MHD unstable state driven by the pressure gradient in a closed flux surface. For successful tokamak operation, MHD equilibrium should be achieved by balancing between two MHD forces; 1) Outward force driven by, 2) Inward force driven by $J_{tor} \times B_{V,ext}$.

Thus, the location of main plasma in closed flux surface is adjusted by the radial force balance, so the vacuum vertical field driven by outer PF coil; the tokamak-like plasma subject to the constraints of radial force balance, $\mathbf{J}_{toroidal} \perp \mathbf{B}_{vertical}$. On the other hand, the magnetic flux ropes follow the magnetic field line and are in the force-free state, $\mathbf{J}_{flux\ rope} \parallel \mathbf{B}_{axial}$. These two plasmas (main plasma and flux rope) react differently to outer vacuum vertical field.

Relatively short coupling time results and their explanation are shown in Figs. 5.1. A toroidal plasma current of 15 kA is achieved using only flux ropes with a total current of 1.5 kA from the arc plasma guns (black lines in Fig. 5.1(b)). The multiplication factor is defined as $MF \equiv I_{Toroidal\ current} / I_{flux\ rope}$, and the highest MF of 10 is achieved, as shown in Fig. 5.1(a). The geometrical factor, G , is the total number of toroidal transits of magnetic flux ropes under the given experimental conditions, such as plasma gun location, magnetic field configuration and its time evolution. It can be obtained using vacuum-field-following calculation. Three distinct phases can be distinguished based on both the geometrical factor, as indicated by the red line, and the MF , as indicated by the black line, in Fig. 12(a): (1) $t = [301\ ms, 302\ ms]$, (2) $t = [302\ ms, 306\ ms]$, and (3) $t = [306\ ms, 309\ ms]$.

For $t = [301\ ms, 302\ ms]$, $MF < G$, the magnetic flux ropes are discharged along the 3D helical magnetic field, and it is expected that flux ropes are external-kink unstable because the plasma current of 1.5 kA far exceeded the predicted I_{KS} of 55 A. The highly dynamic movements of the flux rope are captured in the fast-camera images shown in Fig. 5.2(a). The kinking flux rope starts merging, forming a tokamak-like state with CFS in the toroidally-averaged sense. The enclosure of yellow dots indicates the inner interior wall of VEST, while the enclosure of magenta dots indicates the CFS in the toroidally-averaged sense obtained by current density fitting in Fig. 5.1(c) and 5.1(d). The red vertical line in (b) and (c) indicates the mid limiter.

For $t = [302 \text{ ms}, 306 \text{ ms}]$, $\mathbf{MF} > \mathbf{G}$, the additional toroidal plasma current is driven and maintained by the DC helicity injection, as shown in Fig. 5.1(b) and Fig. 5.2(b). The current density distribution fitted using the finite element method (FEM) at 304.5 ms is visualized in Fig. 5.1(c), which shows the appearance of a CFS in a toroidally-average sense. Note that, during LHI, the magnetic signals are highly stochastic and asymmetric in 3D configuration, so the axisymmetric-current-ring assumption used in FEM is valid only toroidally-averaged-sense. Also, FEM fitting results mean the overall magnetic system has its lowest order moment an $n=0$ component that acts as toroidally-averaged tokamak-like plasma. Considering the magnetic flux contour colored in yellow in Fig. 5.1(c), it is expected that flux ropes follow the magnetic field line at a given gun location, reaching close proximity to the plasma edge is expected. The FEM results also show that high current densities are fitted at the low field side. Successful non-inductive current drive via DC helicity injection using magnetic flux ropes takes place up to this time. After peaks of $I_{Toroidal \text{ current}}$, however, the flux ropes reappear while plasmas in the toroidally-averaged CFS are separated from the flux ropes. The reduced proximity between tokamak plasma and flux rope is shown in both Figs. 5.1(d) and 5.2(c). It is expected that this decoupling results in decreasing toroidal plasma current. Note that the toroidally-averaged tokamak-like plasmas is radially moved by radial force imbalance. The spiraling $I_{flux \text{ rope}}$ (injection current) streams are also assumed as axisymmetric current rings for the FEM-based fitting. The total toroidal currents fitted are comparable to the measured $I_{Toroidal \text{ current}}$, the error of which is less than 4% for both 304.5 ms and 305.6 ms (Figs. 5.1(c) and 5.2(d)). For $t = [306 \text{ ms}, 309 \text{ ms}]$, $\mathbf{MF} < \mathbf{G}$, highly dynamical flux ropes reappear as shown in Fig. 5.2(d), indicating that the LHI process is halted.

To support the claims of non-inductive current drive via LHI, a counter discharge (shot# 33545) is also shown in fig. 5.1 (a)-(b) with blue lines. The only difference between

the two discharges (black and blue line in fig. 5.1 (a)-(b)) is the vertical field, $B_{vertical}$, applied for radial force balance. The evolutions of vacuum $B_{vertical}$ are shown in figure 5.3 (a). Due to the large perturbation to the flux loop and pickup coil signals from the plasmas, the $B_{vertical}$ shown are calculated on the mid-plane at $R = 0.4$ m using a vacuum field model of VEST coils and chamber. Note that the eddy current in chamber is considered for calculation. It is reported that a small variation in the applied $B_{vertical}$ between discharges results in a much larger effect upon the toroidal current[16]. By adjusting the vacuum vertical field, the sustained current drive-in tokamak-like plasma via LHI is achieved. Figure 5.4 show the discharge results. Note that while the injection power and the other condition remain as same, very sensitive changes in vertical field change are made. The magnetic reconstruction using FEM for shot 35964 will be shown in this section with IDS measurement results. The shot result depicted in the purple show the failure of LHI with low injection voltage. It is useful to see the clear difference compared to other shots. One more important result is in the top graph of showing CIII-CII line ratio. The filter scope system in VEST is used for this measurement. When the tokamak-like plasma is formed via LHI, the CIII/CII line ratio evolution is also increased, which means increased confinement.

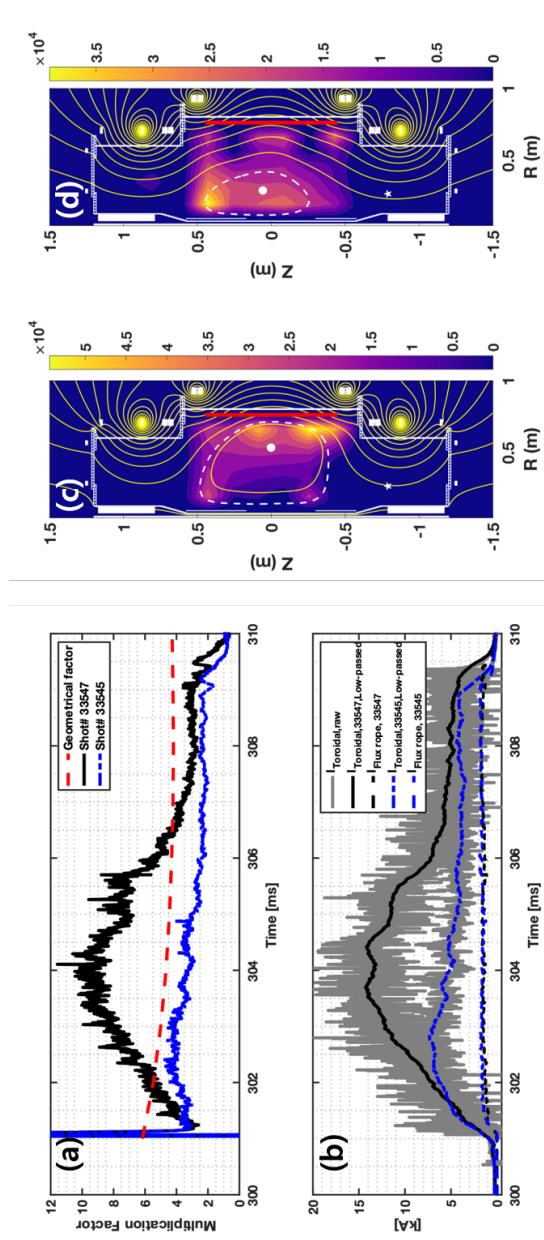


Figure 5.1 (a) Evolution of MF (b) Time evolution of toroidal plasma current and flux rope current. Black(shot# 33547), Blue(shot# 33545). The current density (kA/m^2) distributions for shot# 33547 are fitted (c) at 304.5 ms with the mean magnetic fitting error of 4.4 % and (d) at 305.6 ms with the mean magnetic fitting error of 5.2 %.

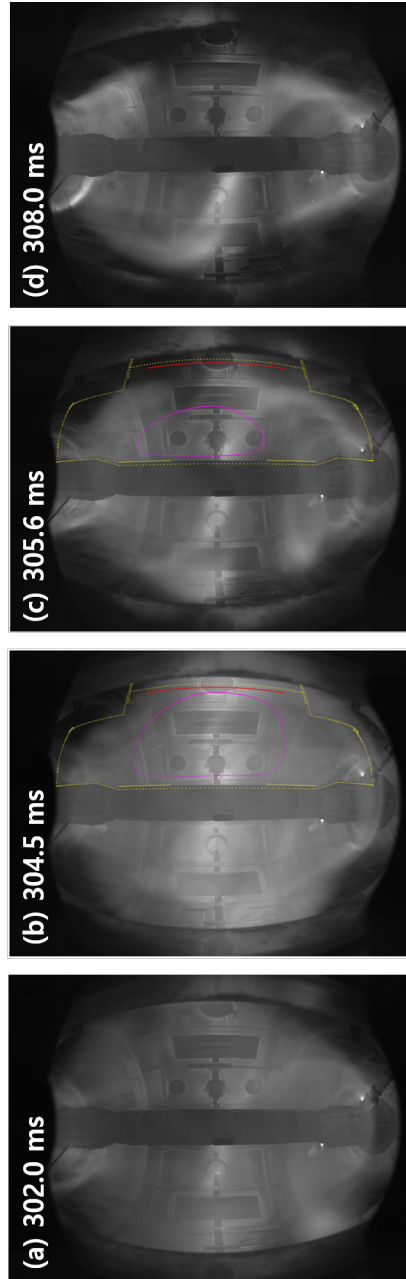


Figure 5.2 Fast-camera images for shot# 33547 shown in Fig. 5.4. Exposure time for each shot is **0.4 ms**. (a) Pre-Taylor relaxation time, (b) during Taylor relaxation at peak toroidal current, (c) reduced Taylor relaxation by radial force imbalance for tokamak plasma, (d) Taylor relaxation is halted.

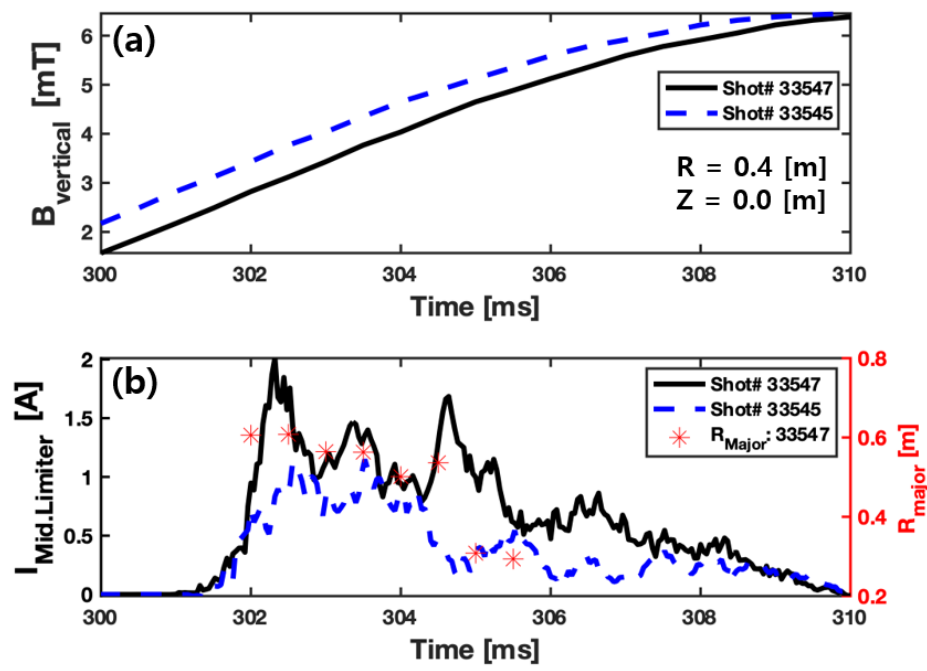


Figure 5.3 (a) The evolutions of the applied vertical magnetic field, and (b) the mid limiter signal for shot# 33547 (black) and shot# 33545 (blue) respectively.

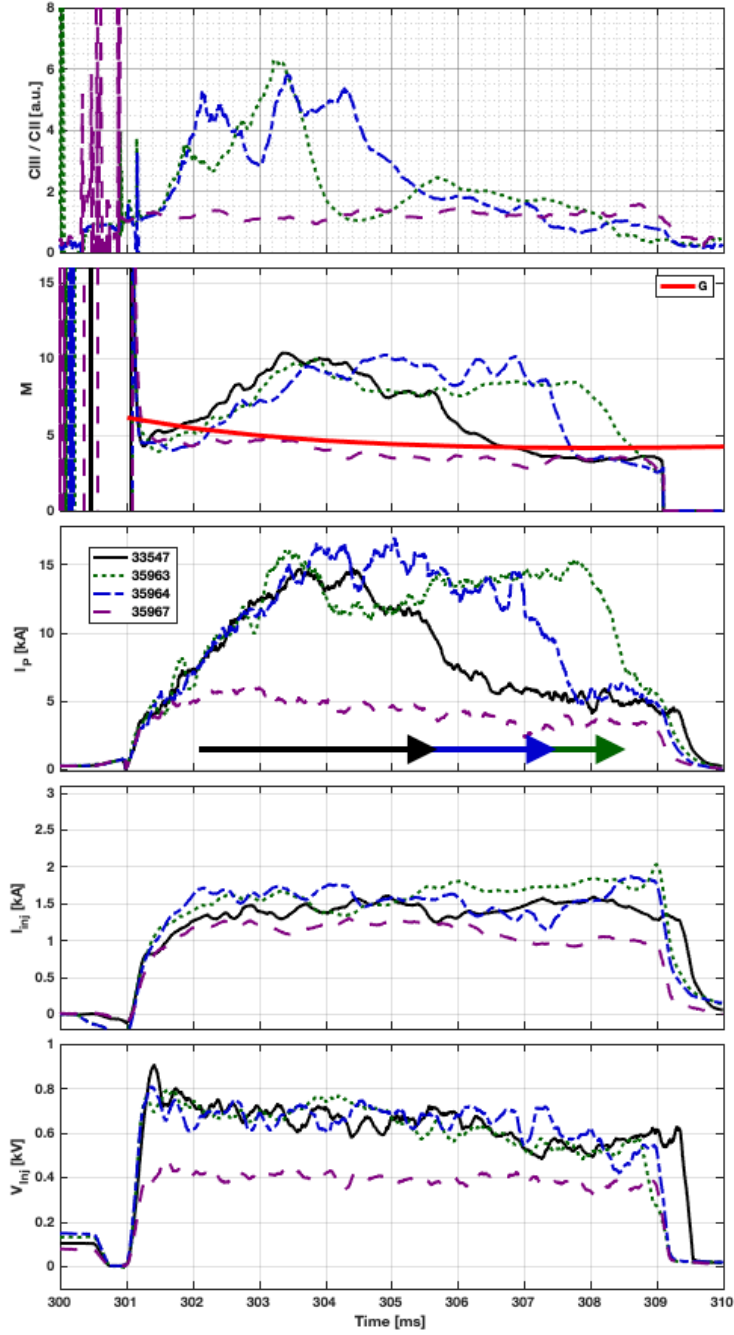


Figure 5.4 The effect of coupling for LHI. With sensitive control of vacuum field, sustained coupling is obtained, resulting in increased pulsed length. The purple line show the failure of LHI, which show the clear difference with other shots.

During the LHI experiment in VEST, as shown in Fig 5.3, the current in the outer PF coil is increased over the discharge time because the present outer PF coil power system in VEST has poor current-waveform controllability. Therefore, the proximity cannot be maintained properly. The rigorous value of proximity cannot be measured as it has dependence on the toroidal location and there is no proper and accurate measurement for this purpose. However, the effect of proximity can be achieved by using various diagnostics simultaneously. For the purpose of finding the effect of proximity, the magnetic reconstruction using FEM[58] and IDS[29] in VEST are used in this section.

Figure 5.5 show the effect of proximity during LHI operation in VEST. The two shots are selected for comparison, but magnetic reconstruction of only the successful result (shot# 35964) is depicted. The white box indicates the distance between the main plasma and flux rope, and their location is obtained by the reconstruction results respectively. While relatively high proximity is maintained ($t = [301\text{ms}, 305\text{ms}]$), increasing and maintaining plasma current is measured. As the proximity is reduced by the increasing vacuum vertical field, decreasing plasma current is observed. Figure 5.6 show the fast camera image at low proximity condition.

Another measurement results that show the importance of proximity are radial ion temperature profile measured by IDS in VEST. One expected phenomenon with high proximity is high ion temperature as they can merge and inject helicity. Figure 5.7 shows both the magnetic reconstruction and the radial ion temperature profile for a given time. The black line in each magnetic reconstruction result indicates the radial profile of ion temperature. One noticeable feature is peaked profiled during high proximity (up to 305 ms). The end of helicity injection due to lowered proximity between plasma and flux ropes is clearly observed for shot# 35964 from the 306 ms. IDS measurement results also show the flatted radial profile. These results strongly support that magnetic reconnection is an important component of magnetic relaxation[38].

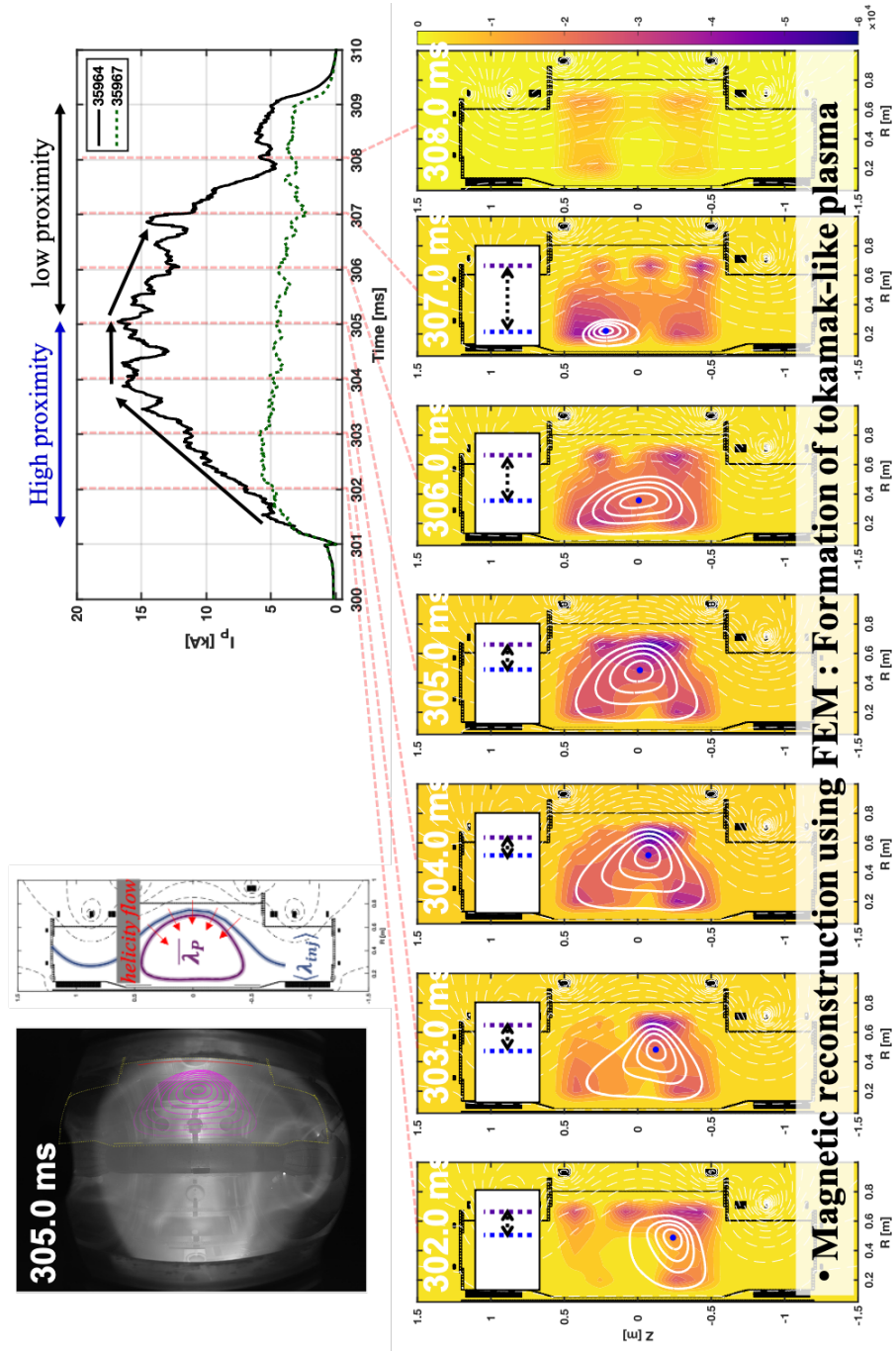


Figure 5.5 The effect of proximity. The white box indicates the calculated distance between the two plasmas.

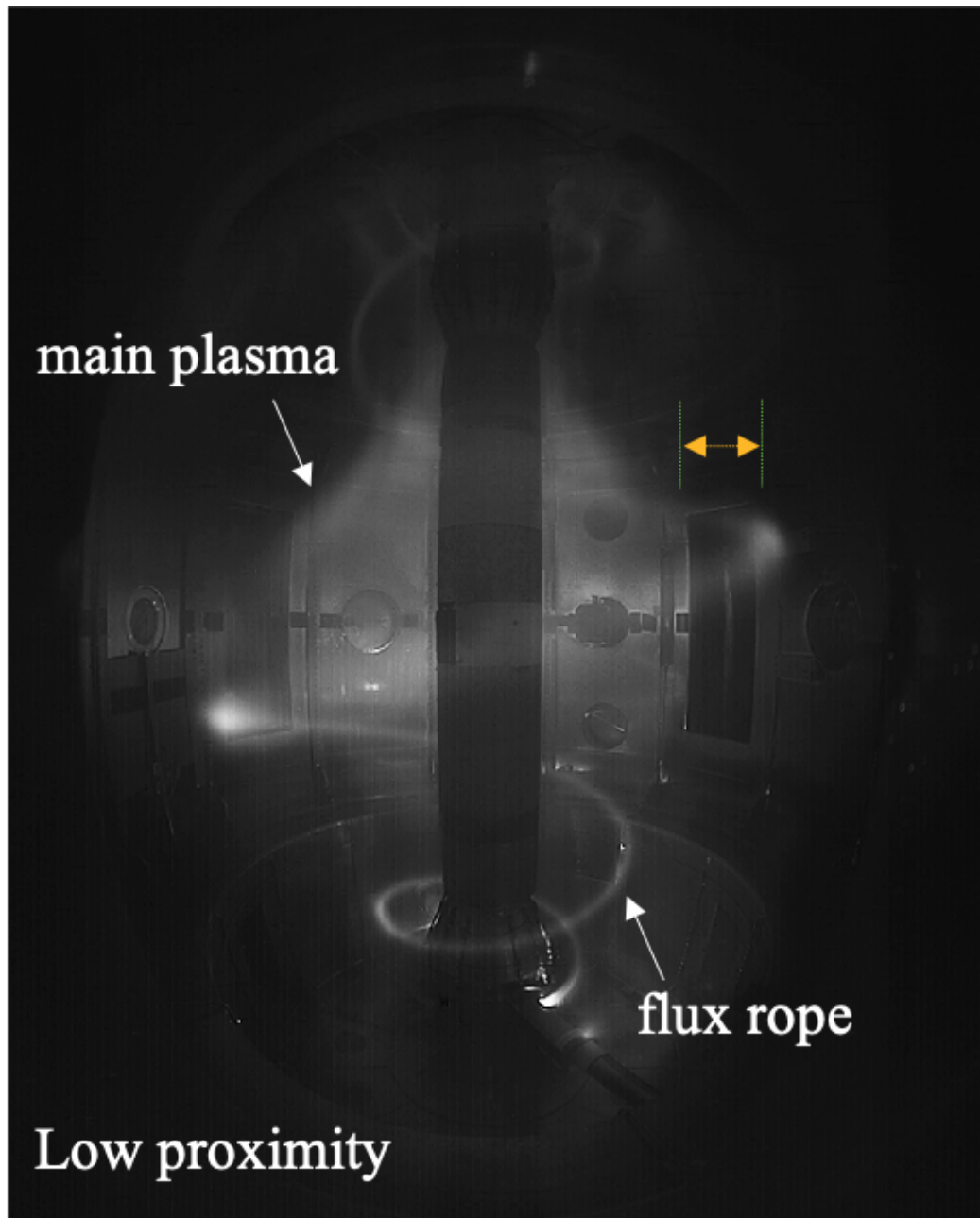


Figure 5.6 Fast camera image at low proximity.

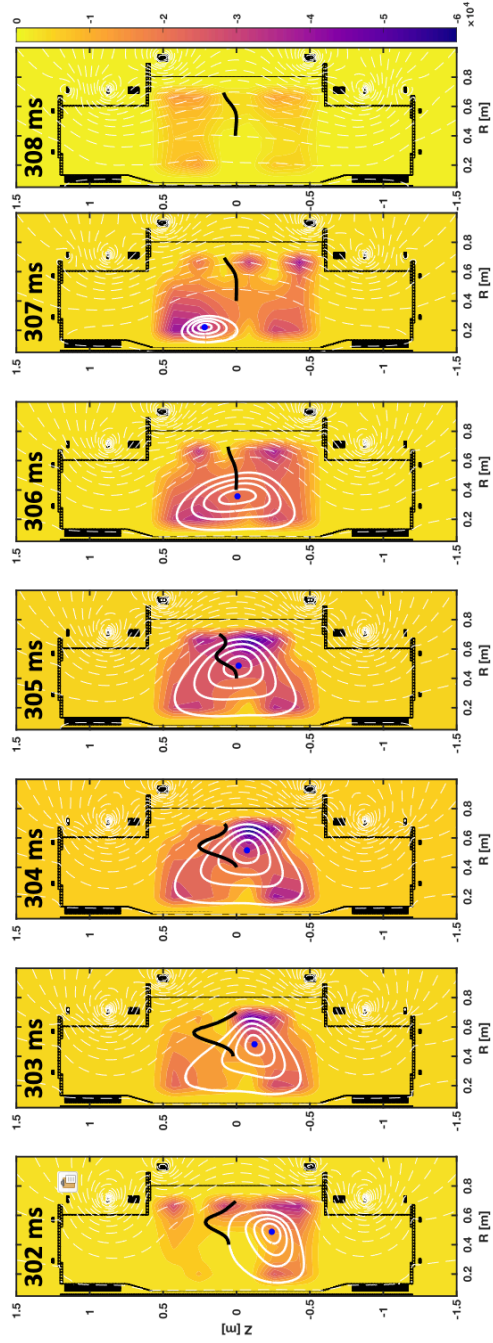


Figure 5.7 Magnetic reconstruction results using FEM for shot 35964. The white closed line shows the toroidally averaged CFS. The black line at the middle of figure is ion temperature profile for a given time.

Similar results using the field following calculation is achieved. As magnetic reconstruction results give the information of toroidally averaged plasma in closed flux surface, the total magnetic field that guides flux rope can be used to field following calculation. Figure 5.8 show the results for Shot# 35964. The Yellow line indicates the location that passed by each injector. As main plasma is decreasing, their toroidal transits are also reduced.

Lastly, the Taylor states, λ , are calculated for Shot#35964 by using FEM-reconstruction results. As mentioned at section 2.4, the gradient lambda is required to inject helicity. With high proximity ($t = [301\text{ms}, 305\text{ ms}]$), the effective toroidal transits (3D winding) of flux rope (turn number) are decreased (shown in Figures 5.8 and 5.9). This can result in the 3D-spatially reduced $\bar{J}_{edge}(G, \text{Reconstruction})$. On the other hand, with the low proximity, \bar{J}_{edge} is recovered, so $\langle \lambda_{inj} \rangle$. However, the effective 3D windings of flux rope are still low because the plasma in CFS still exists, thereby giving high B_{axis} for flux ropes. The error bar in each point is obtained from the reconstruction results.

Finally, it is obvious for the successful LHI operation condition maintaining high proximity is important; condition #2.

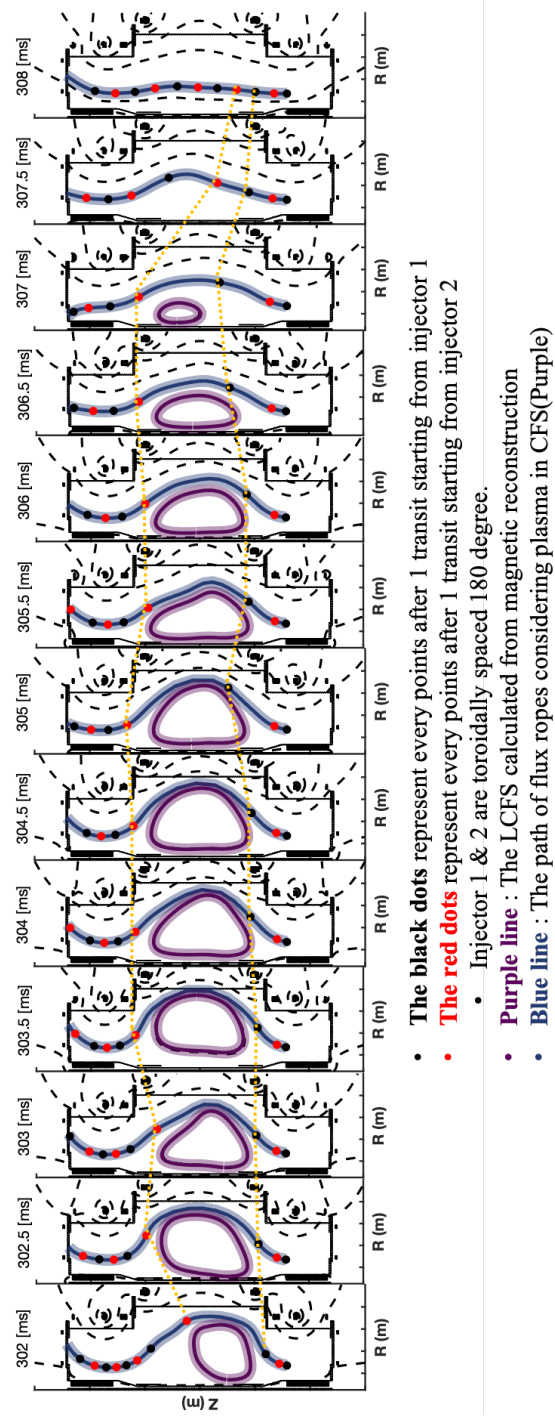
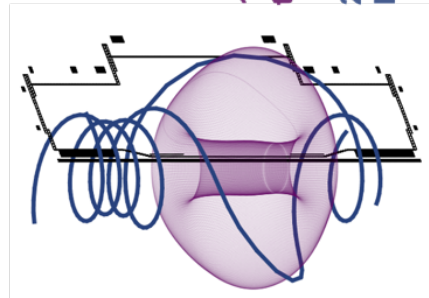


Figure 5.8 The vacuum field following considering FEM-reconstruction results.



$$\overline{\lambda_P} \leq \langle \lambda_{inj} \rangle$$

$$\frac{\mu_0 I_P}{B \phi_{AP}} \leq \frac{\mu_0 j_{edge}}{B_{edge}}$$

1. Plasma to be injected helicity
2. Plasma that provide helicity to be injected

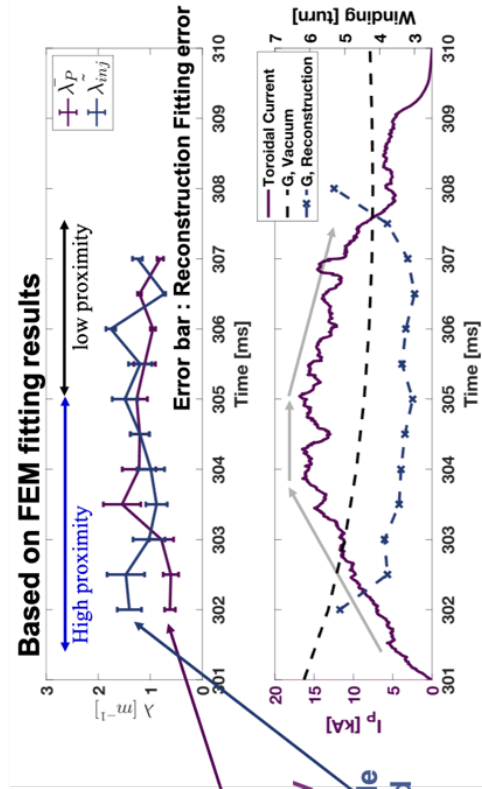


Figure 5.9 Calculation of the Taylor state for Shot# 35964

5.1.2. Operating regime for LHI technique

The LHI experiment is conducted under conditions different from those previously used in chapter 4. The radial location of the arc plasma gun for LHI remains 0.27 m. The LHI in VEST is normally performed with a long helical path length of more than 5 m and a low toroidal field magnetic-field strength of 0.017 T at $R = 0.35$ m, which is less than 10% of the full toroidal field strength of VEST. The magnitude of toroidal field strength is set for the stable operation of LHI at HFS as it is the one that determines the initial field pitch to avoid collision between plasma guns and the flux ropes (current stream), while the strength of the vertical field, the other variable for field pitch, is set to low to provide initial relaxation with relatively low flux rope current in this study. Note that the present magnetic field strength condition for LHI in VEST is obtained based on the number of empirical-trial operations, which is the only successful condition. This condition of field strength results in a low kink threshold, I_{KS} , for the flux ropes. For example, the I_{KS} of the following LHI experiments in VEST is ~ 55 A ($a = 3$ cm, $L \approx 8.6$ m, $B \sim 170$ G). The flux rope current is on the order of kiloamperes, thus, far exceeding the external kink threshold. As the flux rope current increases from zero, either the characteristics described in the previous sections or similar phenomena are expected to occur, and it should appear on both spectrograms of the magnetic diagnostics and spectroscopy.

As the release of an axisymmetric ring is expected through the rope-rope merging at the early phase of the LHI technique, it also should be force-balanced by the outer poloidal field. Thus, not only kink state and rope-rope merging but also a vertical field, at least for one axisymmetric ring, is required. By considering the kink state, the limit of guide field strength for merging, and the vertical field required for radial force balance, the experimental operating map for a successful transition to the Taylor relaxation phase from rope-rope merging can be obtained. Note that, as indicated at previous section, this also means the maintaining high proximity.

By using both Condition #1 from Section 4.2.1 and Condition #2 from Section 5.1.1, the magnetic field operation map for successful LHI operation can be achieved. Figure 5.10 show the experimental operating map of 34 mT. As the high compression force from the axial field is expected, the flux rope radius, a , is set as 1 cm, which is the radius of the injector. One noticeable feature is $\frac{1}{R_0}$ dependencies on the toroidal field. As a result, a major radius higher than 0.4 m is the region that can expect a highly kink unstable mode in flux ropes, thereby rope-rope merging activity. However, when rope-rope merging takes place, so an axisymmetric ring is released from the activity, it will decay right away, as the vacuum vertical field in the poloidal field is too high to balance the radial position of the ring. Finally, the merging activity can take place for the axisymmetric ring, but the plasma to be injected helicity via Taylor relaxation is decay away as soon as it shows up. It is worth noting that the vertical field cannot be reduced as too low strength of the vertical field will result in too low pitch in the vicinity of the injector, which can cause the failure of operation for an injector with high power.

On the other hand, when the field strength of both toroidal is reduced up to 17 mT, the radial force balance condition can be met at outer region, giving both high proximity with a highly kink unstable regime as shown in figure 5.11. Note that the 3D helical configuration (pitch, time evolution) in both 5.10 and 5.11 is maintained. The lowered compression force on flux rope may result in an expanded radius.

Figure 5.12 show the two LHI discharge results in both figure 5.10 and figure 5.11. Interestingly, the black line that represents $|B| \sim 17$ mT shows the increased toroidal plasma current in VEST, which is show, presumably, the formation of tokamak-like plasma. However, the green line that represents $|B| \sim 34$ mT shows the steady time evolution of toroidal plasma current. Note that the only difference is the vacuum magnetic field strength condition, other conditions such as injection power, and neutral pressure

injection remain the same.

So far, the scenario for LHI operation has been considered whether the vacuum vertical field can be overwhelmed by plasma in a closed flux surface or not. However, the results of this approach highly count on the initial setup for plasma in closed flux surface. The operating map introduced in this chapter has also used the assumption, but it is only one of flux rope's radius, a . So, it is a quite robust and reliable operating map for LHI operation.

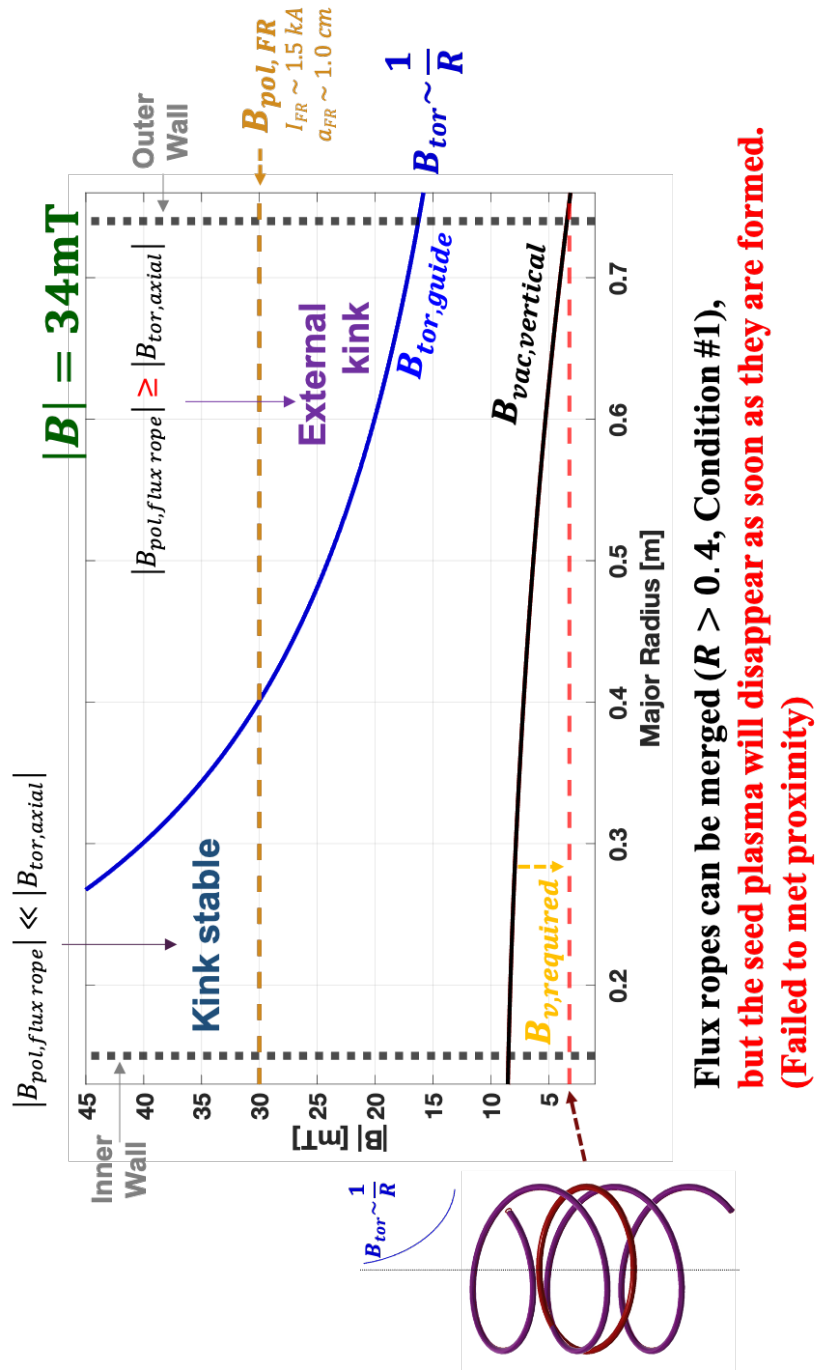
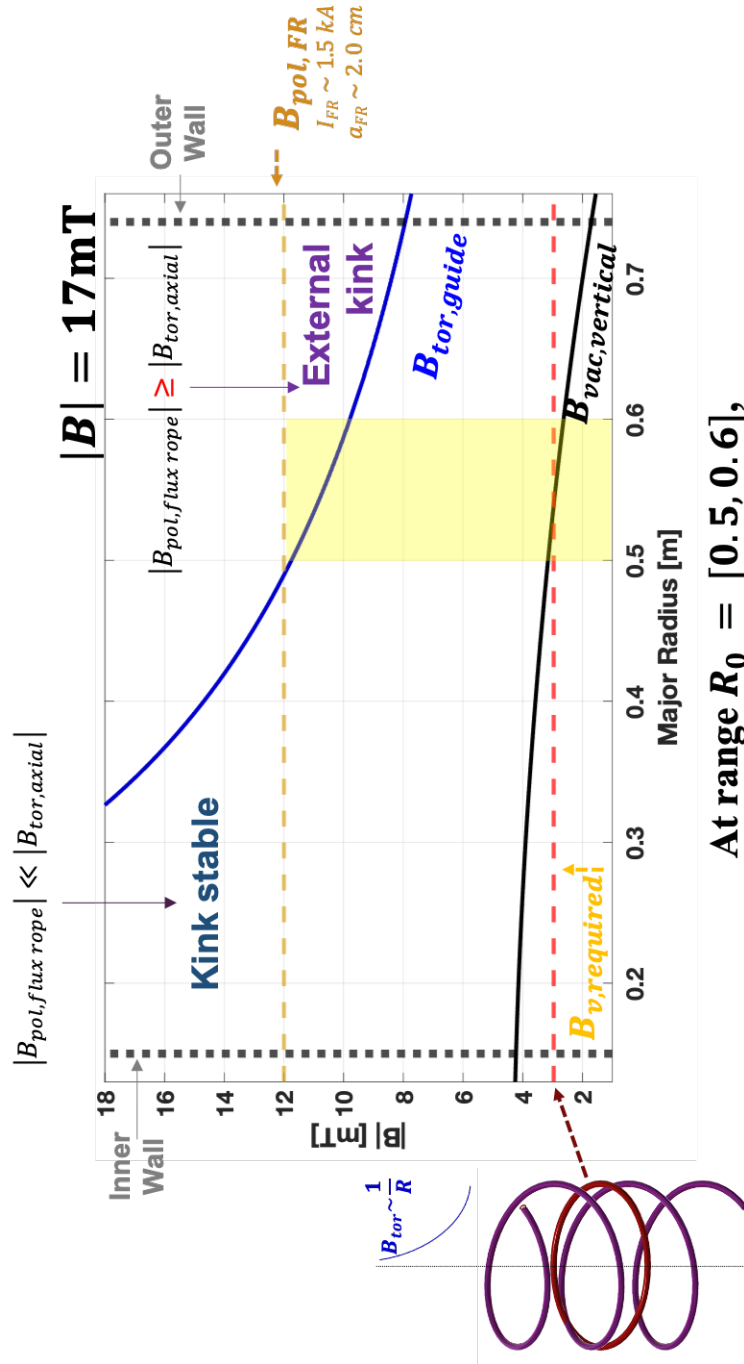


Figure 5.10 LHI operating map for $|B| = 34 \text{ mT}$



At range $R_0 = [0.5, 0.6]$,
Both condition #1 and #2 can be met simultaneous!

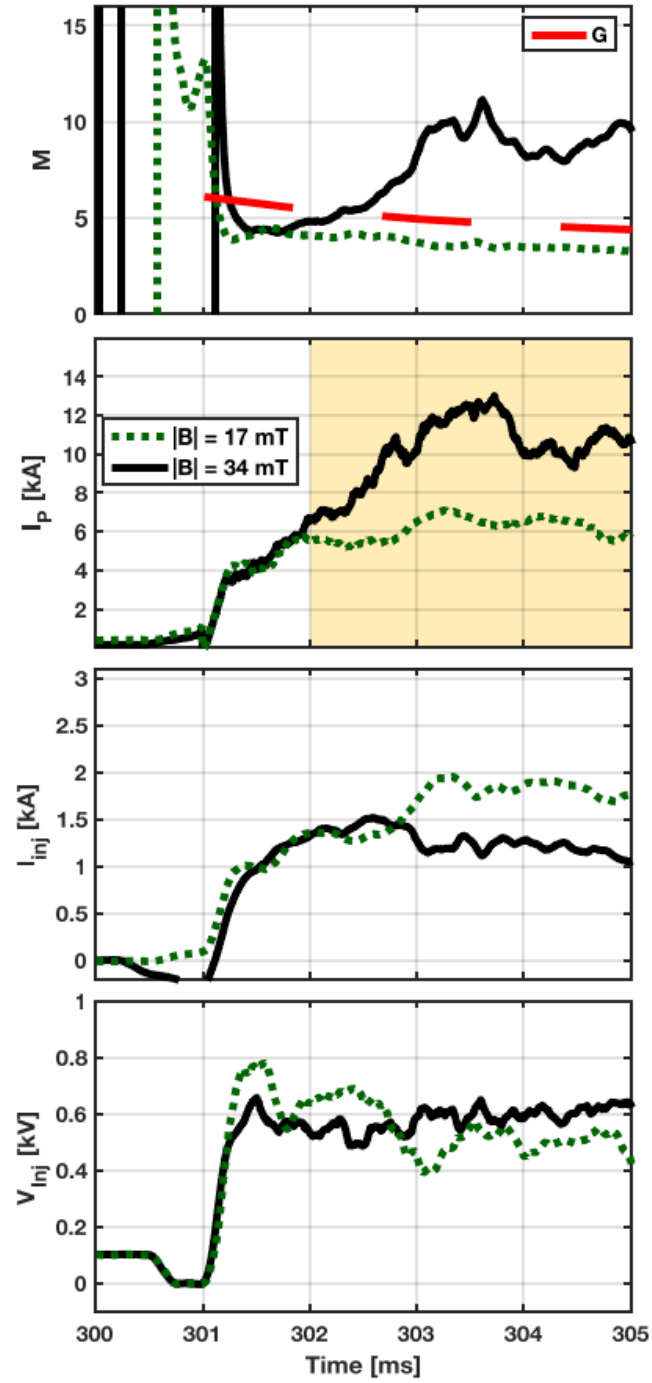


Figure 5.12 LHI discharge results for operation map experiment.

5.2. Characteristics of plasma driven by LHI

5.2.1. Anomalous ion heating

This section focuses on the observation of anomalous ion heating during LHI in VEST. Ion temperatures and acceleration during LHI with merging activity are measured using the IDS shown in Chapter 3.2.2.1. As mentioned before, the LHI technique highly counts on merging and magnetic reconnection activity from the start to the end. Thus, a high ion temperature or unique profile is expected during LHI.

The IDS measurement results for shot 35963 are shown in figure 5.13. To check its anomalous profile, the counter discharge result (Shot 35967) is also depicted. When the plasma current is driven non-inductively, so the merging activity is expected, the peaked spatial profile of CIII ion temperature is observed. The yellow shaded area indicates the location of flux rope confirmed by the fast camera and magnetic reconstruction. All the IDS measurement data in this section are processed using Doppler tomographic inversion technique. At the time 304.5 ms, for shot 35963, the degradation of I_p by impurity from the wall will be mentioned in the section 5.2.2 with Thomson scattering measurement. A similar tendency is also observed in the IDS results in figure 5.13. The emissivity and the temperature were reduced compared to the results before and after that time. The magnetic reconstruction results using FEM and ion temperature profile results are shown in figure 5.14. The white-closed lines in each graph indicate the closed flux surface in a toroidally-averaged sense. The colored contour in the graph shows the current density distribution. The current densities are located in the vicinity of the outer wall. Note that, in section 5.1.2, the only outer region is the only location where flux ropes can be merged by external kink mode. For plasma in closed-flux-surface, edge-localized ion heating is observed. It is not that surprising as injection helicity via the Taylor relaxation process requires ‘coupling’ (close proximity), they should be merged via magnetic reconnection. At 308 ms, decoupling (lowered proximity) results in flatted profile, which means the end of the

helicity injection process.

The same result for shot 35964 is shown in Figures 5.12 and 5.7. A similar tendency persists during the discharge time. Though the end of injection helicity due to lowered proximity between plasma and flux ropes is clearly observed for shot 35964 from the 306 ms.

The observation of edge-localized anomalous ion heating is also reported by the PEGASUS[15]. The main difference is the LHI scheme. In Burke, et al, the LHI experiments were conducted by outboard LHI while the inboard LHI scheme is used in VEST. As a result, the ion temperature profile had peaked at the most outward location (around the injector). The experiment results in this thesis also show the peaked profile but, it has peaked at the point between plasma in CFS and flux ropes. Also, Burke, et al, have reported the multi-gaussian results as two velocity distribution is expected; 1) main plasma, and 2) plasma from the injector. It is reasonable to expect similar two gaussian fitting can be done in VEST. An example of the trial result is shown in figure 5.16. Figure 5.16 (a)-(b) show the two gaussian fitting results, while figure 5.16 (c)-(d) shows the single gaussian fitting results that are used for the IDS results in this thesis. The reduced residue (5 times) in figure 5.16(a) looks promising compared to 5.16 (c). However, there is the possibility of the low signal intensity may lead to the appearance of a second gaussian. The verification remained for future works.

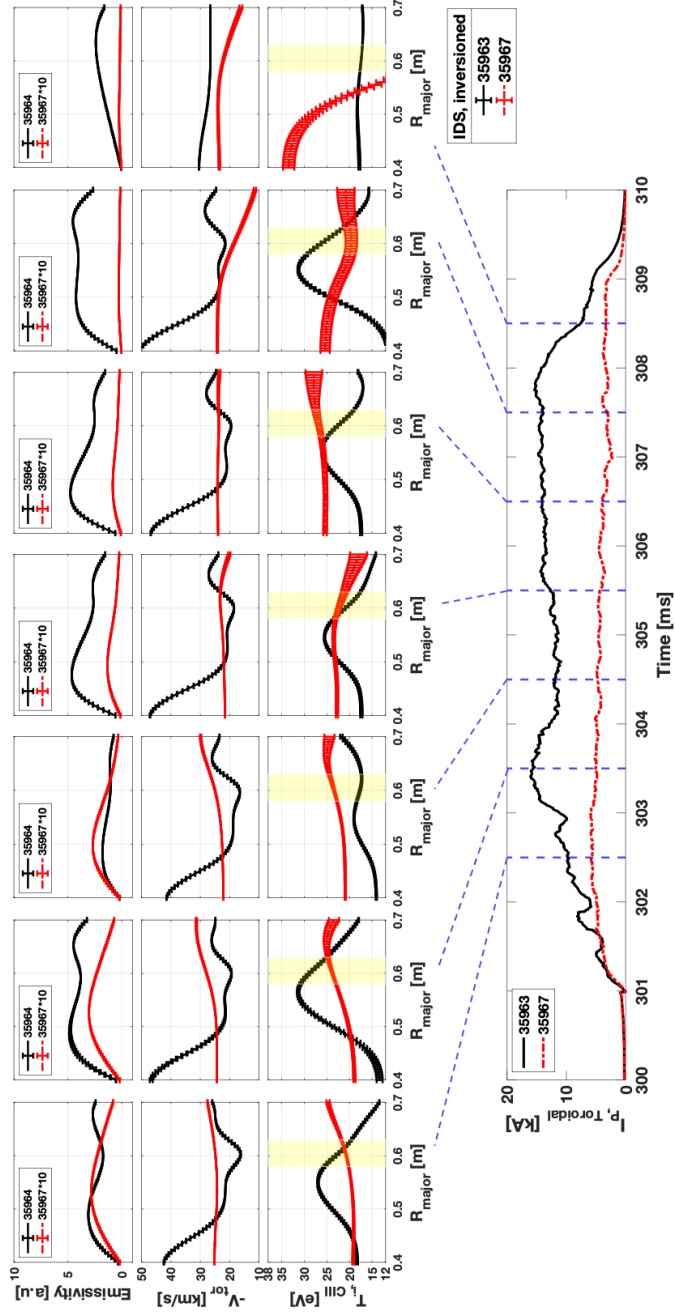


Figure 5.13 IDS measurement results of Shot 35963. To check its anomalousness, the counter discharge of shot 35967 is shown in red. The graphs in top row show the emissivity. The graphs in middle row show the toroidal velocity while the graphs in low row show the ion temperature profile.

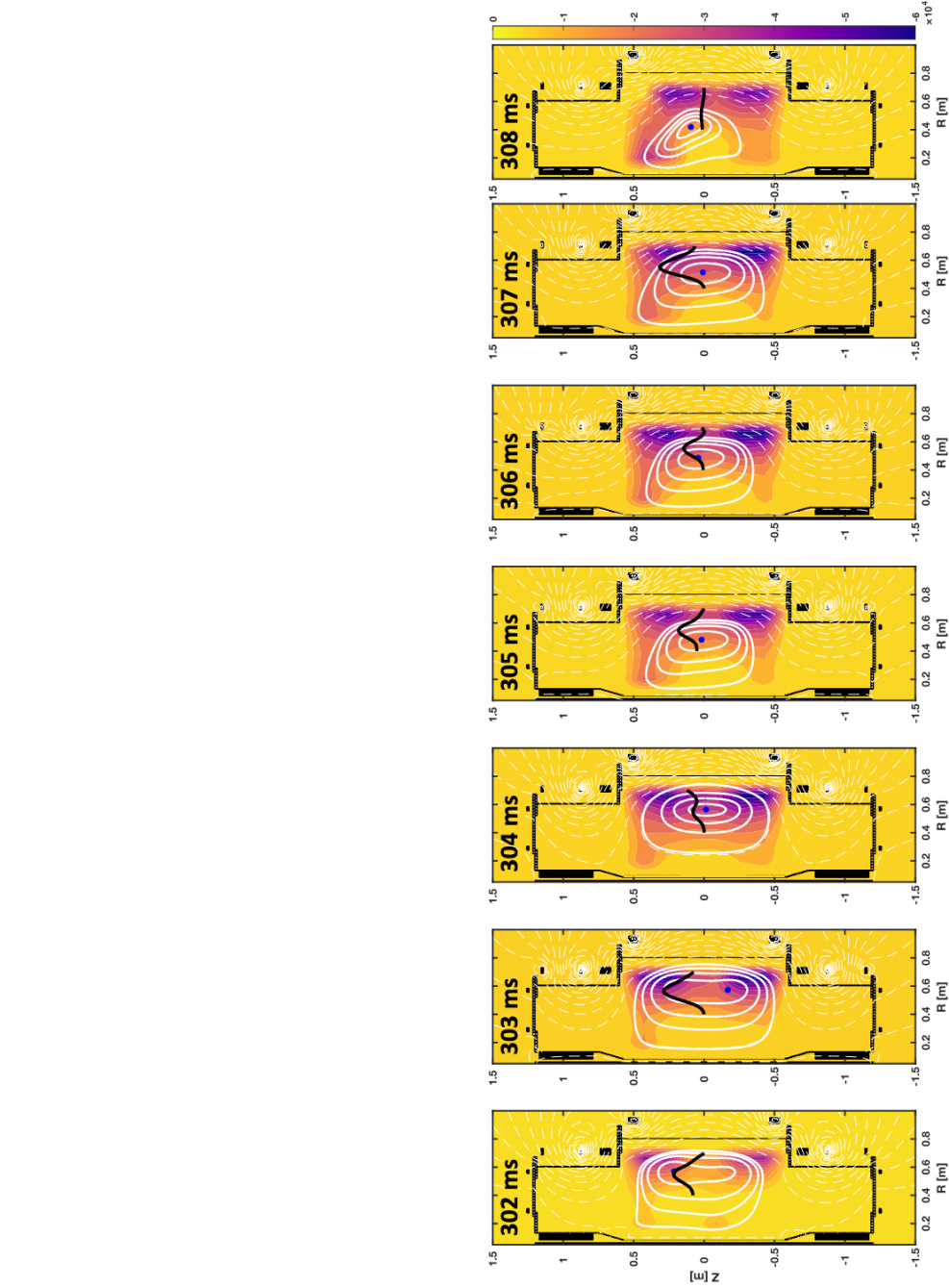


Figure 5.14 Magnetic reconstruction results using FEM for shot 35963. The white closed line shows the toroidally averaged CFS. The black line at the middle of figure is ion temperature profile for a given time.

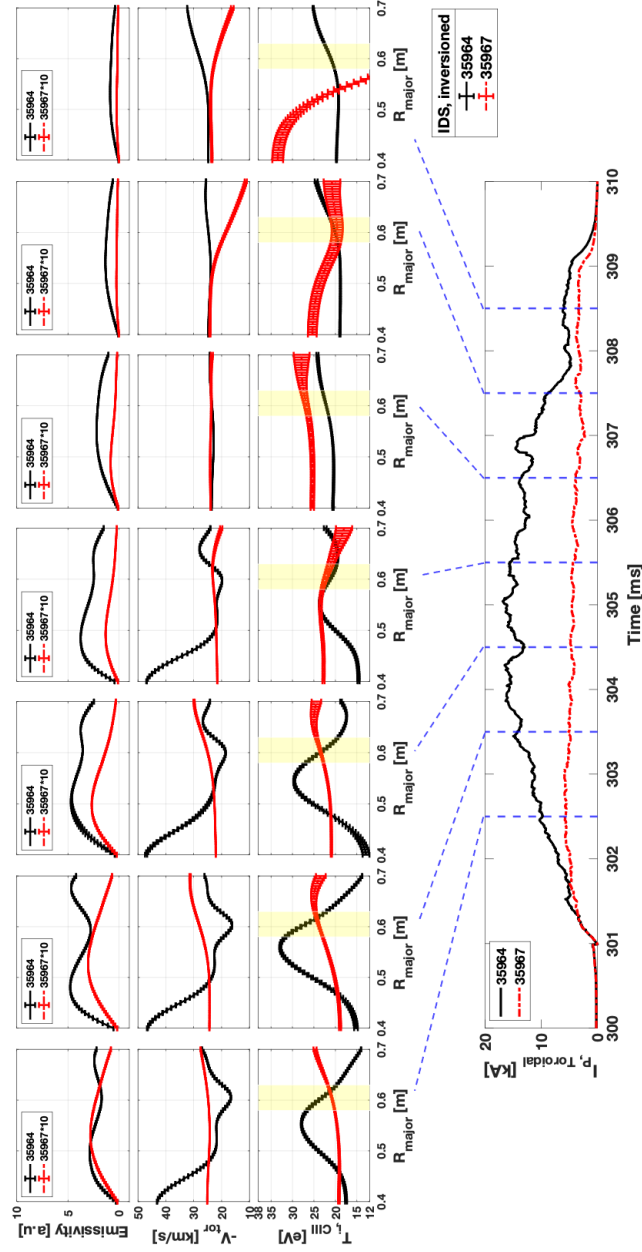


Figure 5.15 IDS measurement results of Shot 35964. To check its anomalousness, the counter discharge of shot 35967 is shown in red. The graphs in top row show the emissivity. The graphs in middle row show the toroidal velocity while the graphs in low row show the ion temperature profile.

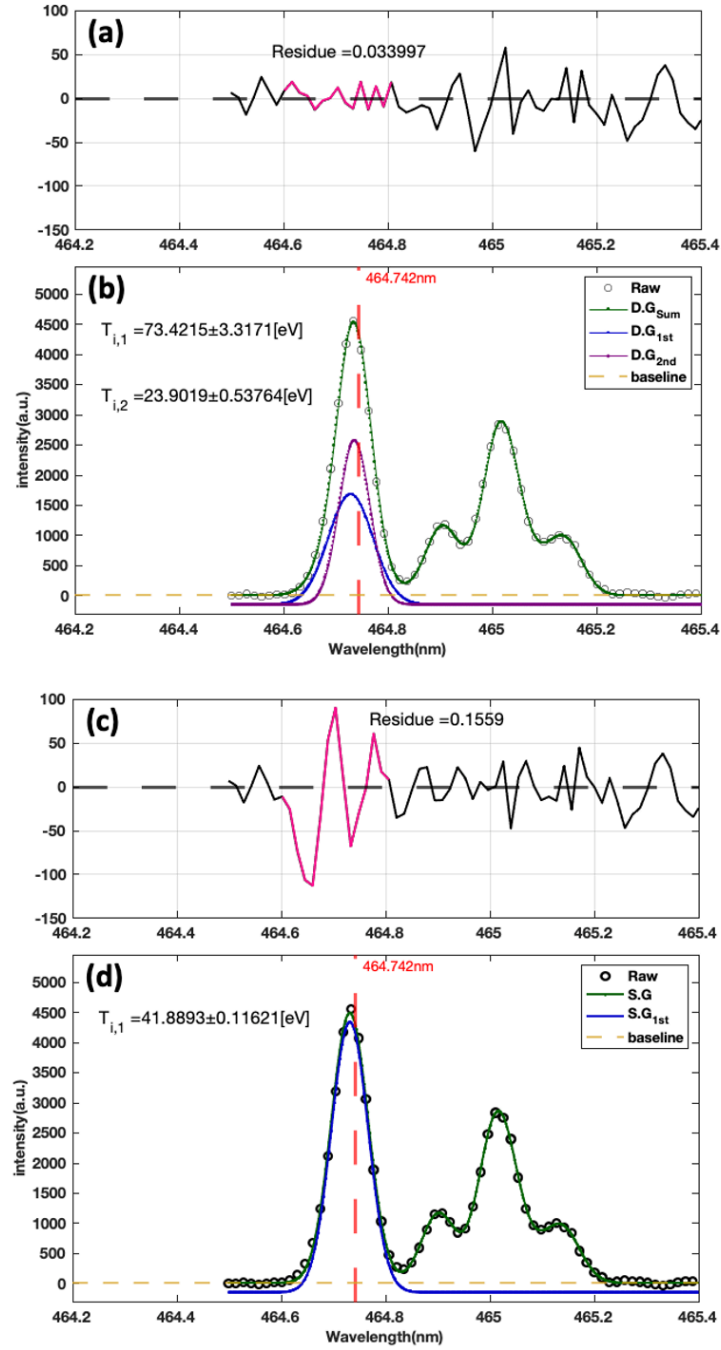


Figure 5.16 The example of trial result of two gaussian fitting for IDS

5.2.2. Initial measurement of T_e , n_e profile

In addition, to support the formation of tokamak-like plasma further, the radial and time evolution of electron density, n_e , and temperature, T_e , and are measured using the Thomson scattering system in VEST, and shown in figure 5.17. The data points at $R = 0.7$ are measured via the triple Langmuir probe. During the discharge, n_e of $\sim 10^{19} \text{ #/m}^3$ is maintained. In shot 35963, there is a deep profile in the plasma current at 304-306 ms. The reason is presumed to be impurity injection from the wall. As a result, degradation in both n_e and T_e is also observed at TS measurement data of 35963. As the tokamak-like plasma performance recovered, increased data in both n_e and T_e is also observed. The sustained tendency and its value mean increased confinement along with the radial locations. Note that the CIII/CII line ratio results in figure 5.4 also means the increased electron temperature, thereby increased confinements. It is obvious that flux ropes are located in the low field side region, as confirmed by the fast camera.

In addition, the soft x-ray signal is measured for shot 35963, 35964, 35967 as shown in figure 5.18. The signals were not processed (inversion), so the line-integrated signal was depicted. As the toroidal plasma current is driven via LHI (Shot 35963, 35964), the strong SXR signal is getting strong, meaning the formation of hot core. When no plasma current is driven (Shot 35967), the quiet signal was measured, which indicates no confinement or heating on electrons.

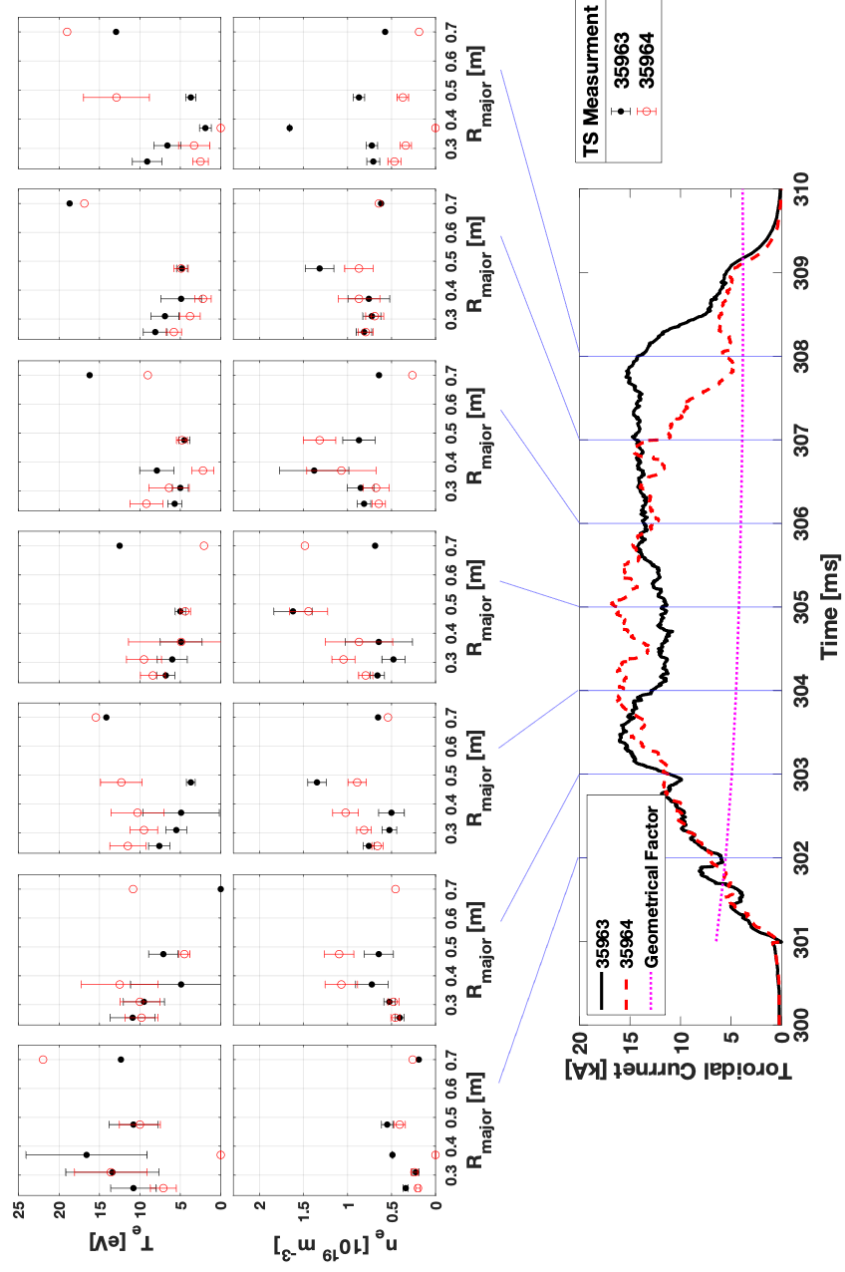


Figure 5.17 Radial and time evolution of n_e and T_e using Thomson scattering measurement system in VEST

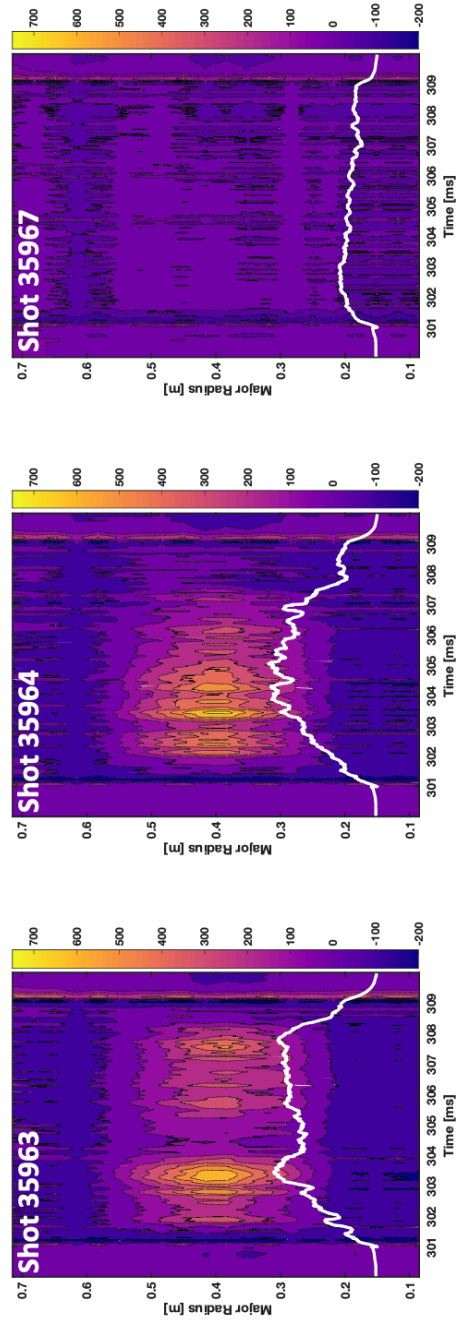


Figure 5.18 Radial and Time evolution of Soft X-ray signal. The filter #1 that can transmit the signal higher than 10eV, Al 0.1 μ m, was used. The signal is line integrated. White line in each graph shows the corresponding plasma current evolution.
Shot 35967: Failed LHI shot.

5.2.3. The MHD transition

In section 4.1.2, A novel approach to distinguish kink mode in 3D helical flux ropes is suggested and verified experimentally with the calculation based on phenomenological theory and monoenergetic assumption. This approach also can be applied to the LHI experiment to check not only the external kink state before reaching the Taylor relaxation state, but also any MHD characteristics changes during LHI.

The aforementioned process of LHI in section 5.1.1, Shot 33547, can be clearly observed in and described by the spectrograms of both the magnetic pickup coils and Rogowski coil. Figure 5.19 shows the magnetic measurements of both discharges in Figs. 5.1(a) and 5.1(b). For shot# 33547, the broadband magnetic signal occurs on both the inboard and outboard pickup coils as shown in Figs. 5.19(a) and 5.19(b), but not on the Rogowski coil as shown in Fig. 5.19(c) for $t = [301 \text{ ms}, 302 \text{ ms}]$. As the flux rope current reached 1.5 kA in less than 0.5 ms, the external kink mode is observed from the very early time of discharge. Note that a magnetic flux rope that undergoes an external kink mode with highly dynamical motion does not leave a signal on the Rogowski coil, as described in Section 4.1.2.

At $t = [302 \text{ ms}, 306 \text{ ms}]$, $MF > G$, the broadband magnetic signals are measured by both the inboard pickup coil and the Rogowski coil, as shown in Figs. 5.15(a) and 5.15(c). Interestingly, the signal measured by the outboard pickup coil, Fig. 5.15(b), is significantly reduced during this time range. The appearance of broadband signals on the Rogowski coil means two important points in this experiment: (1) Both coherent internal kink and external kink modes in flux rope are disappeared in this phase. (2) The plasma undergoes changes in internal properties that lead to changes in toroidal plasma current. These changes are not entirely unexpected, as the LHI method is accompanied by a redistribution of current density, anomalous transport, and flux rope merging via magnetic reconnection[13, 14]. Note that the coherent internal kink mode described in Section 4.1.2.

is also included in the example of changing internal properties.

As the approach is absent from internal and direct measurement, it is not yet clear by what internal properties are changed and accompanied by broadband internal mode during LHI in VEST. One possible explanation for this LHI result is the reduced $n = 1$ MHD mode during LHI, extensively studied and reported by PEGASUS[10, 11]. The most noticeable feature of the reduced $n = 1$ mode is the disappearance(reduced) of the large $n=1$ mode in outboard magnetic fluctuation (figure 5.19 (b)) while the inboard magnetic fluctuation (figure 5.19 (a)) has persisted over the discharge time. In addition, increased edge density which is a generally favorable factor for inducing the reduced $n = 1$ mode is confirmed by magnetic reconstruction (figures 5.1 (c) and 5.1 (d)). Also, the edge fueling from the strong wall interaction might be realized, as the strong wall interaction is confirmed by reconstruction (figure 5.1 (c)) and mid-limiter signal (figure 5.3 (b)). However, there are differences from what is reported to get the reduced $n = 1$ MHD mode. First, the reduced $n = 1$ mode is always accompanied by the high $n = 1$ mode before it appear[11], which is not observed during the LHI operation in VEST so far. Second, the ratio of plasma current and toroidal field coil current, I_p/I_{TF} , is ~ 0.4 in this result, which is too low to expect the reduced $n = 1$ mode. In addition, the only difference in discharge conditions is the small change of $B_{vertical}$ (figure 5.3 (a)) for the two discharges in figures 5.1(a) and 5.1(b), which is not a clear whether it is a factor for achieving reduced $n = 1$ mode so far. This is the subject of the ongoing investigation for LHI in VEST.

As MF decreased, for $t = [306 \text{ ms}, 309 \text{ ms}]$, the broadband magnetic signal by the external kink in the flux rope is measured again by the outboard pickup coil but not by the Rogowski coil, as shown in Figs. 5.19(b) and 5.19(c). As described in the section 5.1.1 and shown in Fig. 5.1 (d) and 5.2(c), the coupling between the toroidally-averaged tokamak-like plasma and flux ropes is not maintained; the tokamak-like plasma decay away, and only the flux ropes undergo external kink instability remains in the LFS.

Conversely, it is confirmed by the approach that only the external kink mode is maintained over the discharge time for shot# 33545, as shown in Figs. 5.19(d)-(f). The broadband magnetic signals are measured on both the inboard and the outboard pickup coil. The Rogowski coil has measured a relatively quiet and low signal as only external kink mode persists over the discharge time. The experimental results of the current drive via LHI in VEST can be divided into three distinguishable phases. The phases are confirmed by magnetic reconstructions (figure 5.1) and the magnetic spectrogram approach (figure 5.19) proposed in this paper, which shows consistency. This tendency is also observed for the sustained current drive results; Shot 35963-35964, which is shown in figure 5.20. Shot 35967, the highly kink stable mode, is show the quiet signal on Rogowski coil as expected.

The disappearance of outer mirnov pickup coil signal from flux rope can be considered the ideal wall condition given by main plasma. As they coupled (high proximity), locally the external kink unstable flux rope can be stable by the ideal wall condition (high conductivity of main plasma). Thus, the highly chaotic mirnov signal from external kink unstable flux rope can be quiet.

This is a very interesting result as the high performance of reduced-MHD mode can be achieved without transition from the high-MHD mode. This is a subject of the future investigation for LHI in VEST.

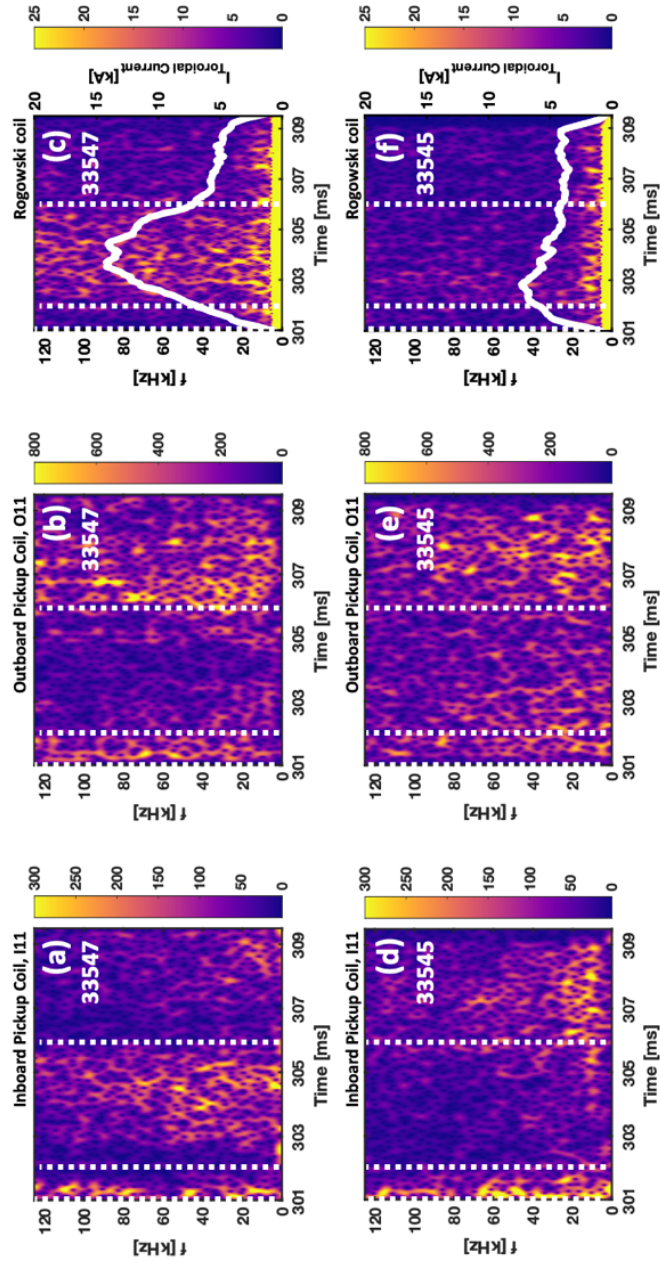


Figure 5.19 Spectrograms of (a) Inboard magnetic pickup coil, I11, (b) Outer magnetic pickup coil, O11, (c) Rogowski coil for shot# 33547. Spectrograms of (d) Inboard magnetic pickup coil, I11, (e) Outer magnetic pickup coil, O11, (f) Rogowski coil for shot# 33545. The white line in Figs. 15(c) and 15(f) represents the toroidal plasma current measured by the Rogowski current.

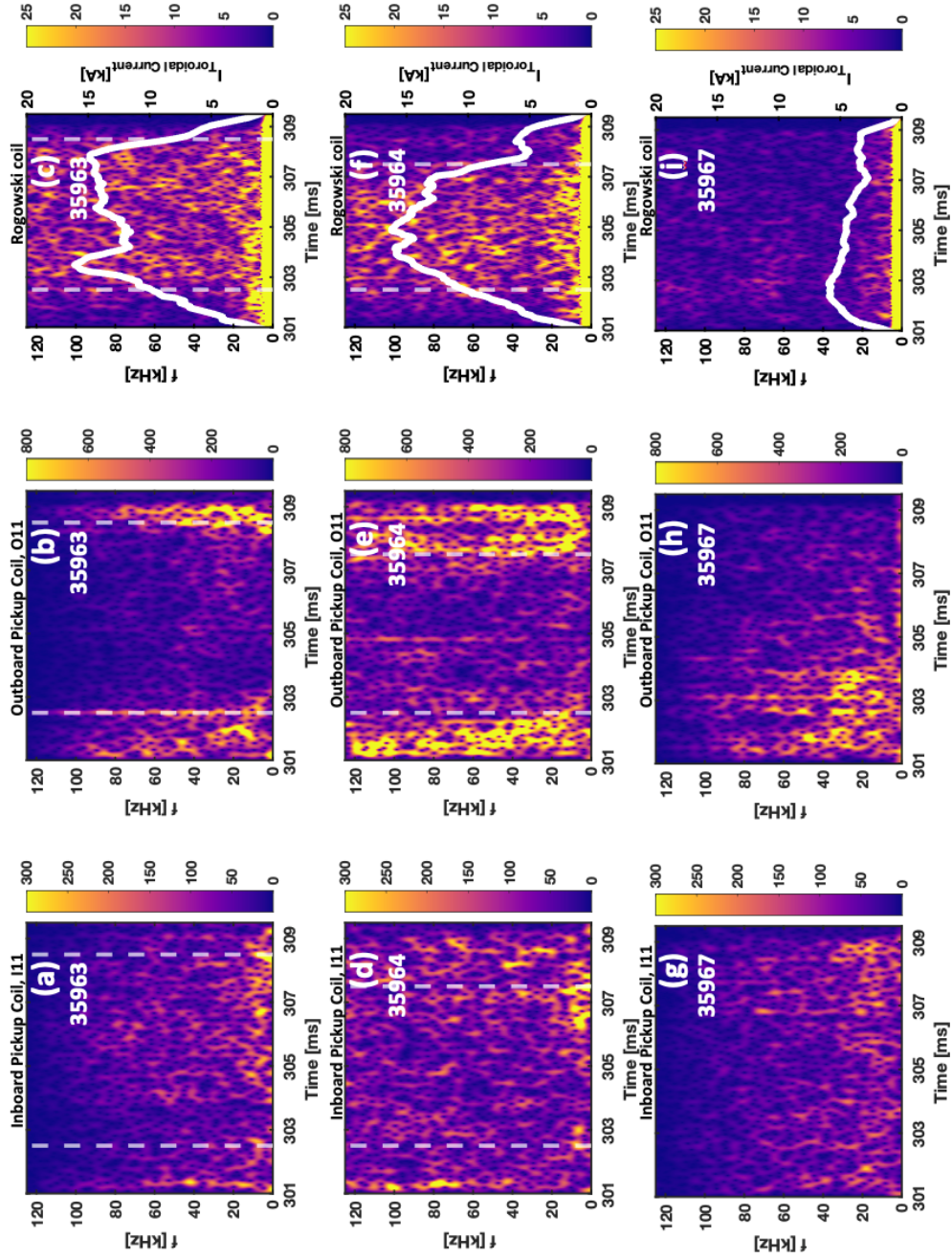


Figure 5.20 Spectrograms approach of sustained current drive with LHI; Shot 35963((a), (b), (c)), Shot 35964((d), (e), (f)), Shot35967((g), (h), (i))

Chapter 6. Conclusions and Future Work

6.1. Conclusions

The objectives of this thesis were satisfied as:

1. For the formation of seed plasma during LHI operation as a startup, the external kink mode in the 3D magnetic flux ropes, and rope-rope merging activity between the 3D magnetic flux ropes are necessary.
2. The radial force balance for, at least, the winding of the magnetic flux rope ring surrounding the central core is required to reach Taylor relaxation state, thereby giving high proximity.
3. The toroidal(guide) field is the first order of limiting factors for LHI operation at a given injection power, as it controls the kink mode in flux ropes and the merging activity
4. The tokamak-like plasmas driven by the LHI system in VEST were found to exhibit tokamak-like macroscopic properties such as increased confinement, the formation of closed flux surface at least in toroidally-averaged sense
5. The strong edge-localized ion heating is persisted during current drive via LHI, which implies the Taylor relaxation process accompanies the change of magnetic topology via strong magnetic reconnection activity.

6.2. Future work

Future work is categorized according to specific main goals; 1) Improvement of LHI system in VEST, 2) More higher performance experiment, 3) LHI-initiated plasma physics.

1. Improvement of LHI system in VEST
 - The increased power capability and its control

- Modify injector design and its shield that can sustain high power with minimum impurities
 - Operational dependence on the wall condition → The measurement of time variant local impurity influx using spectroscopy
2. More higher performance experiment
- Combining with Ohmic operation
 - Applying real-time controllable PF power system
3. LHI-initiated plasma physics
- What VEST LHI mode is; reduced $n=1$ or new mode?
 - Local relaxation and current drive mechanism[40]
 - Explore the LHI confinement and stability properties in VEST
 - Developing the predictive modeling and empirical scaling for VEST

Bibliography

- [1] Wesson, J. and D.J. Campbell, *Tokamaks*. Vol. 149. 2011: Oxford university press.
- [2] Raman, R. and V. Shevchenko, *Solenoid-free plasma start-up in spherical tokamaks*. Plasma Physics and Controlled Fusion, 2014. **56**(10): p. 103001.
- [3] Tanabe, H., et al., *Investigation of merging/reconnection heating during solenoid-free startup of plasmas in the MAST Spherical Tokamak*. Nuclear Fusion, 2017. **57**(5): p. 056037.
- [4] Yamada, T., et al., *Double null merging start-up experiments in the University of Tokyo spherical tokamak*. EXS, 2010. **2**: p. 19.
- [5] Ishiguro, M., et al. *Investigation of non-inductive plasma current start-up by RF on QUEST*. in *Journal of Physics: Conference Series*. 2014. IOP Publishing.
- [6] Uchida, M., et al., *Rapid current ramp-up by cyclotron-driving electrons beyond runaway velocity*. Physical review letters, 2010. **104**(6): p. 065001.
- [7] Raman, R., et al., *Non-inductive current generation in NSTX using coaxial helicity injection*. Nuclear fusion, 2001. **41**(8): p. 1081.
- [8] Raman, R., et al., *Demonstration of tokamak ohmic flux saving by transient coaxial helicity injection in the National Spherical Torus Experiment*. Physical review letters, 2010. **104**(9): p. 095003.
- [9] Hwang, Y.-S., *Studies of non-inductive current drive in the CDX-U tokamak*. 1993: Princeton University.
- [10] Bongard, M.W., et al., *Advancing local helicity injection for non-solenoidal tokamak startup*. Nuclear Fusion, 2019. **59**(7): p. 076003.
- [11] Perry, J.M., et al., *Initiation and sustainment of tokamak plasmas with local helicity injection as the majority current drive*. Nuclear Fusion, 2018. **58**(9): p. 096002.
- [12] Ono, M. and R. Kaita, *Recent progress on spherical torus research*. Physics of Plasmas, 2015. **22**(4): p. 040501.
- [13] O'Bryan, J.B., *Numerical Simulation of Non-Inductive Startup of the Pegasus Toroidal Experiment*. 2014, The University of Wisconsin-Madison.
- [14] O'Bryan, J., C. Sovinec, and T. Bird, *Simulation of current-filament dynamics and relaxation in the Pegasus Spherical Tokamak*. Physics of Plasmas, 2012. **19**(8): p. 080701.
- [15] Burke, M.G., et al., *Continuous, edge localized ion heating during non-solenoidal plasma startup and sustainment in a low aspect ratio tokamak*. Nuclear Fusion, 2017. **57**(7): p. 076010.
- [16] Eidietis, N., et al., *Non-inductive production of ST plasmas with washer gun sources on the Pegasus Toroidal Experiment*. Journal of fusion energy, 2007. **26**(1): p. 43-46.
- [17] Fiksel, G., et al., *High current plasma electron emitter*. Plasma sources science and technology, 1996. **5**(1): p. 78.
- [18] Hinson, E.T., et al., *Impedance of an intense plasma-cathode electron source for tokamak startup*. Physics of Plasmas, 2016. **23**(5): p. 052515.
- [19] Hinson, E.T., *Physics of the current injection process during localized helicity*

- injection. 2015, The University of Wisconsin-Madison.
- [20] Ishikawa, J. and T. Takagi, *Beam-plasma discharge in a Kyoto beam-plasma-ion source*. Journal of Applied Physics, 1983. **54**(6): p. 2911-2922.
 - [21] Furno, I., et al., *Current-driven rotating-kink mode in a plasma column with a non-line-tied free end*. Physical review letters, 2006. **97**(1): p. 015002.
 - [22] Ryutov, D., et al., *Phenomenological theory of the kink instability in a slender plasma column*. Physics of plasmas, 2006. **13**(3): p. 032105.
 - [23] Sun, X., et al., *Transition of MHD kink-stability properties between line-tied and non-line-tied boundary conditions*. Physical review letters, 2008. **100**(20): p. 205004.
 - [24] Shi, P., et al., *Alfvénic modes excited by the kink instability in PHASMA*. Physics of Plasmas, 2021. **28**(3): p. 032101.
 - [25] Paz-Soldan, C., et al., *Two-dimensional axisymmetric and three-dimensional helical equilibrium in the line-tied screw pinch*. Physics of Plasmas, 2011. **18**(5): p. 052114.
 - [26] Bergerson, W.F., *Experimental observation of internal and external kinks in the resistive wall machine*. 2008, University of Wisconsin--Madison.
 - [27] DeHaas, T.A., *Transformation of Canonical Helicity under the Collision and Merging of Two Magnetic Flux Ropes*. 2017: University of California, Los Angeles.
 - [28] Yamada, M., R. Kulsrud, and H. Ji, *Magnetic reconnection*. Reviews of modern physics, 2010. **82**(1): p. 603.
 - [29] 김유성, *Ion Heating and Rotation Acceleration during Bursting MHD Events on Versatile Experiment Spherical Torus, in VEST 장치에서 Bursting MHD 현상에 의한 이온 가열 및 회전 가속*. 2019, 서울 : 서울대학교 대학원: 서울.
 - [30] Yamada, M., et al., *Conversion of magnetic energy in the magnetic reconnection layer of a laboratory plasma*. Nature communications, 2014. **5**(1): p. 1-8.
 - [31] Parker, E.N., *Sweet's mechanism for merging magnetic fields in conducting fluids*. Journal of Geophysical Research, 1957. **62**(4): p. 509-520.
 - [32] Yamada, M., et al., *Experimental study of two-fluid effects on magnetic reconnection in a laboratory plasma with variable collisionality*. Physics of Plasmas, 2006. **13**(5): p. 052119.
 - [33] Zweibel, E.G. and M. Yamada, *Magnetic reconnection in astrophysical and laboratory plasmas*. Annual review of astronomy and astrophysics, 2009. **47**: p. 291-332.
 - [34] Yoo, J., et al., *Observation of ion acceleration and heating during collisionless magnetic reconnection in a laboratory plasma*. Physical review letters, 2013. **110**(21): p. 215007.
 - [35] Intrator, T., et al., *Experimental onset threshold and magnetic pressure pile-up for 3D reconnection*. Nature Physics, 2009. **5**(7): p. 521-526.
 - [36] Sun, X., et al., *Flux rope dynamics: experimental study of bouncing and merging*. Physical review letters, 2010. **105**(25): p. 255001.

- [37] Jensen, T.H. and M.S. Chu, *Current drive and helicity injection*. The Physics of fluids, 1984. **27**(12): p. 2881-2885.
- [38] Taylor, J., *Relaxation and magnetic reconnection in plasmas*. Reviews of Modern Physics, 1986. **58**(3): p. 741.
- [39] Ono, M., et al., *Steady-state tokamak discharge via dc helicity injection*. Physical review letters, 1987. **59**(19): p. 2165.
- [40] Richner, N., et al., *Magnetic Turbulence and Current Drive During Local Helicity Injection*. Physical Review Letters, 2022. **128**(10): p. 105001.
- [41] Chung, K., et al., *Design features and commissioning of the versatile experiment spherical torus (VEST) at Seoul National University*. Plasma Science and Technology, 2013. **15**(3): p. 244.
- [42] 안영화, *Efficient plasma start-up experiments using trapping particle configuration in versatile experiment spherical torus*, in *VEST 장치의 플라즈마 시동 실험 연구*. 2014, 서울 : 서울대학교 대학원: 서울.
- [43] Lee, J., et al., *Design and commissioning of magnetic diagnostics in VEST*. Fusion Engineering and Design, 2013. **88**(6-8): p. 1327-1331.
- [44] 정의찬, *MHD-Coherent External Filaments and Internal Reconnection Event in VEST*, in *VEST 장치에서의 자기수력불안정성-외부 필라멘트 커플링과 내부자기재결합 현상 연구*. 2022, 서울 : 서울대학교 대학원: 서울.
- [45] Park, J., et al., *Design and development of the helicity injection system in Versatile Experiment Spherical Torus*. Fusion Engineering and Design, 2015. **96**: p. 269-273.
- [46] Darrow, D.S., *DC helicity injection studies on the current drive experiment*. 1988, Princeton University. p. xi, 82 leaves.
- [47] An, Y., et al., *Control and data acquisition system for versatile experiment spherical torus at SNU*. Fusion Engineering and Design, 2013. **88**(6-8): p. 1204-1208.
- [48] Rim, G.-H., et al., *Pulse forming lines for square pulse generators*. IEEE transactions on plasma science, 2003. **31**(2): p. 196-200.
- [49] Yee, J. and P. Bellan, *Taylor relaxation and λ decay of unbounded, freely expanding spheromaks*. Physics of Plasmas, 2000. **7**(9): p. 3625-3640.
- [50] Park, J.Y., et al., *Identification of kink instability in 3D helical flux ropes at VEST*. Physics of Plasmas, 2022. **29**(5): p. 052112.
- [51] Hsu, S.C. and P.M. Bellan, *Experimental identification of the kink instability as a poloidal flux amplification mechanism for coaxial gun spheromak formation*. Physical review letters, 2003. **90**(21): p. 215002.
- [52] Bergerson, W., et al., *Onset and saturation of the kink instability in a current-carrying line-tied plasma*. Physical review letters, 2006. **96**(1): p. 015004.
- [53] DeHaas, T., W. Gekelman, and B. Van Compernelle, *Experimental study of a linear/non-linear flux rope*. Physics of Plasmas, 2015. **22**(8): p. 082118.
- [54] Intrator, T., et al., *Long-lifetime current-driven rotating kink modes in a non-line-tied plasma column with a free end*. Journal of Geophysical Research: Space Physics, 2007. **112**(A5).

- [55] Tanabe, H., et al., *Electron and ion heating characteristics during magnetic reconnection in the MAST spherical tokamak*. Physical review letters, 2015. **115**(21): p. 215004.
- [56] Linton, M., *Reconnection of nonidentical flux tubes*. Journal of Geophysical Research: Space Physics, 2006. **111**(A12).
- [57] Linton, M., R. Dahlburg, and S. Antiochos, *Reconnection of twisted flux tubes as a function of contact angle*. The Astrophysical Journal, 2001. **553**(2): p. 905.
- [58] Lee, J., et al., *Development of equilibrium fitting code using finite element method in versatile experiment spherical torus*. Fusion Engineering and Design, 2018. **131**: p. 141-149.

국 문 초 록

VEST 장치에서의 3D 자기 플럭스 로프를 활용한 비유도적 전류 구동 연구

박 중 윤

에너지시스템공학부

(핵융합 및 플라즈마 공학 전공)

서울대학교 대학원

Tokamak 구조에서 magnetic helicity의 물리량은 Poloidal과 Toroidal flux의 꼬임(linkage) 정도로 정의된다. 고정 Toroidal flux 조건 및 Tokamak 구조에서 Magnetic Helicity의 증가는 Toroidal 플라즈마 전류 및 성능 증가를 의미한다. Magnetic Helicity를 주입하기 위해, 3D 구조의 Magnetic flux 로프들을 활용한 국부 정전 헬리시티 주입 방법(Local helicity injection, LHI)이 개발되었다. 이 LHI는 본질적으로 한정된 유도적 (inductive) 전류 구동(current-drive) 성능을 가진 구형 토러스 (Spherical Torus, ST)의 시동(Startup) 및 전류 구동을 위해 사용된다.

ST의 시동을 위해 LHI를 사용하기 위해서는, 닫힌 플럭스 면(Closed-flux-surface, CFS)의 초기 플라즈마 생성이 필요하다. 이 초기 플라즈마에 Magnetic helicity를 주입함으로써 더욱 큰 전류가 구동될 수 있으며, 이 과정은 테일러 완화 과정(Taylor relaxation process)으로 설명될 수 있다. 테일러 완화 과정은 국부(local)적으로 주입된 Helicity가 전체(Global) helicity 및 전류 양으로 변화하는 과정을 뜻한다. 마침내 Tokamak과 유사한 닫힌 플럭스 면을 가지는 플라즈마가 방전된다. 여기서 중요한 점은 닫힌 플럭스 면의 초기 플라즈마 형성 없이는 구형 토러스의 시동 방법으로 국부 정전 헬리시티 주입법은 불가능하다는 것이다.

단힌 플럭스 면의 초기 플라즈마를 형성할 수 있는 자기유체역학 불안정성(MHD instability) 중 하나는 3D Helical 구조에서 꼬임 불안정성(Kink instability)을 겪는 Flux 로프들의 결합(Merging)이다. 하지만 ST에서 3D 자기 Flux 로프를 활용하여 단힌 플럭스 면의 초기 플라즈마 형성을 위한 운전 조건이 제시되거나 알려지지 않은 채로 남겨져 있고, 이는 ST 운전 실패의 가능성을 남겨두고 있다. 따라서 국부 자기 헬리시티 주입을 통한 구형 토러스 시동 성공을 위해, 3D 구조의 자기 Flux 로프들로 Tokamak과 같은 구조의 플라즈마를 형성하는 자기 위상(Magnetic Topology) 변화를 설명하기 위한 물리학적 배경을 이해 및 운전 조건을 제시하는 것이 중요하게 되었다. 이러한 배경으로 이 학위 논문의 목적은, 성공적인 LHI 운전 및 ST의 시동을 위해, 3D Flux rope들로부터 단힌 플럭스 면의 초기 플라즈마 형성을 위해 어떤 물리학적 배경이 있으며, 이들이 어떤 방식으로 연결될 수 있는지 해답을 찾고, 주어진 ST 운전 범위 안에서 물리학적 배경의 실험 운전 조건을 제시하는 것이다.

VEST 장치에서 3D 구조의 플럭스 로프를 형성하기 위해, 아크 플라즈마 총과 두 개의 펄스 파워로 이루어진 LHI 시스템이 개발되었고, 성공적으로 운전되고 있다. 방전 조건에 따라 아크 플라즈마 총들은 1.5MW의 전력 범위 안에서 최대 3 kA의 플럭스 로프를 10ms 동안 방전할 수 있다. 정규화 된 유효 토로이달 일주 전압은 최소 1.4 에서 최대 2.4 V-m의 범위를 가진다. 이온 도플러 분광기(IDS)을 활용하여 이온 온도를 측정할 수 있으며, 이 논문에서는 자기 재결합 현상의 정도를 대변하기 위해 사용되었다. 주요 분광 선은 CIII(464.7 nm)로, VEST에서 가장 강한 불순물 성분이다.

본격적인 플럭스 로프들 사이 결합(merging) 현상 연구전에, 아크 플라즈마 총으로부터 방전된 3D 플럭스 로프들의 두 가지 꼬임 불안정성 모드에 대해 관찰하고 분석하였다. 이 모든 상태는 어떠한 물리적 침범 없이, IDS와 자기 진단계를 활용하여 진단되었다. 축 방향 자기장 세기를 주요 변수로 하여, 이를 통해 플럭스 로프들

의 안정 상태를 제어할 수 있었다. 이 자기장 세기가 플럭스 로프로부터 생성된 Poloidal Field보다 강할 때는, 플럭스 로프는 %안정상태(MHD stable)에 있으며, 이 플라스마의 온도와 밀도는 배경 중성 가스 입자에 의해 결정 된다. 축 방향 자기장 세기가 낮아짐에 따라, 내부 결맞음 꼬임 불안정성(Internal coherent kink instability)이 나타나며, 꼬임 불안정성의 회전 주파수 및 변형(deformation) 정도가 계산되었으며, 실험과 계산 결과가 매우 잘 맞는 결과를 보여주었다. 현상학적(Phenomenological) 꼬임 불안정성 이론과 단일 에너지(Monoenergetic) 가정을 기본으로 한 결맞음(Coherent) 회전 모델이 개발되었고, 이 결과와 실험 결과 역시 매우 잘 일치하는 결과를 보여주었다. 축 방향 자기장 성분을 더 감소시키면, 더욱 불안정한 외부 꼬임 불안정성(Highly unstable external kink instability)이 관찰되며, 자기 진단기에 혼돈 행태 신호(Chaotic signal)를 남긴다. 이 외부 꼬임 불안정성 모드가 발현됐을 때, 자기 재결합(Magnetic reconnection)을 통한 Flux rope들의 결합이 일어날 수 있다. 이 영역에서 자기 재결합에 의한 이온 온도 증가와 방전 전력은 선형 관계를 보여준다. 축 방향 자기장 성분은 플럭스 로프의 꼬임 불안정성을 억제할 뿐 아니라, 결합 활동을 억제하는 반발력(repulsing force)을 제공한다. 자기 플럭스 로프들 사이의 간격이 감소했을 때, 이온 온도의 증가가 관찰됐으며, 이는 3D 자기 재결합 구조를 감안한 재결합 각도(reconnection angle) 계산 결과와 동일한 경향을 보여준다. 이 연구를 통해 얻어진 중요한 조건 중 하나는 한정된 방전 전원으로 3D구조의 플럭스 로프 결합을 위해서는 자기장 세기의 상한 값이 있다는 것이 확인되었다. 이 범위 안에서 로프들의 결합이 일어날 수 있다.

결합(Merging) 과정을 위한 조건이 만족됐을 때, 또 다른 중요한 조건이 만족해야만 비로소 Toroidal 플라스마 전류가 비유도적(Non-inductively)으로 구동될 수 있다. 이는 근접성(Proximity or coupling)으로, 3D 플럭스 로프들과 초기 플라스마 사이의 간격을 의미한다. 오직 높은 근접성(high proximity)이 유지될 때, 증배 계수(Multiplication factor)가 ~10에 도달 가능했으며, 1.5 kA의 방전 전류로 15 kA의 플

라즈마 전류가 구동 되었다. 전류 증가 시점에 증가된 CIII/CII 비율이 관찰되었으며, 이는 증가한 가둠 효율을 의미한다. FEM 법을 활용한 자기 재구성(Magnetic reconstruction) 결과는 토로이달 방향의 평균화된(Toroidally-averaged) 닫힌 플럭스 면을 보여준다. 높은 근접성이 유지될 때, 토로이달 전류의 증가와 함께, 봉우리 형태의 이온 온도 경향(Peaked profile of ion temperature)이 관찰되었으며, 이는 활발한 자기 재결합 현상이 일어나고 있음을 뜻한다. 흥미롭게도, 이때 플럭스 로프 속 꼬임 불안정성에 의한 자기 신호들이 사라지며, “Reduced n=1 MHD mode”와 유사한 특성을 보여준다. 방전이 마무리되는 시점에서는 지름 방향 힘의 균형(Radial force balance) 맞지 않아 근접성이 감소하고, 토로이달 전류의 감소가 나타나며 테일러 완화 과정이 중단된다. 플럭스 로프 속 외부 꼬임 불안정성에 의한 신호가 다시 나타나며, 평평한 형태의 이온 온도 경향(Flatted profile of ion temperature)이 나타난다.

3D 구조의 자기 플럭스 로프는 결합부터 국부 헬리시티 주입 과정까지 필수적인 역할을 한다. 진공 자기장 세기와 방전 전원 제어를 통한 3D 플럭스 로프의 안정성 모드 및 Merging 연구를 통해, 두가지 필수 운전 조건이 제안되었다. 방전 전력과 진공 자기장 제어성의 향상을 통해, 국부 헬리시티 주입을 통한 더욱 증가된 토로이달 전류가 기대된다.

주요어: 구형 토러스, 플라즈마 총, 펄스 파워, 자기 재결합, 머징, 헬리시티 주입

학 번: 2013-23180